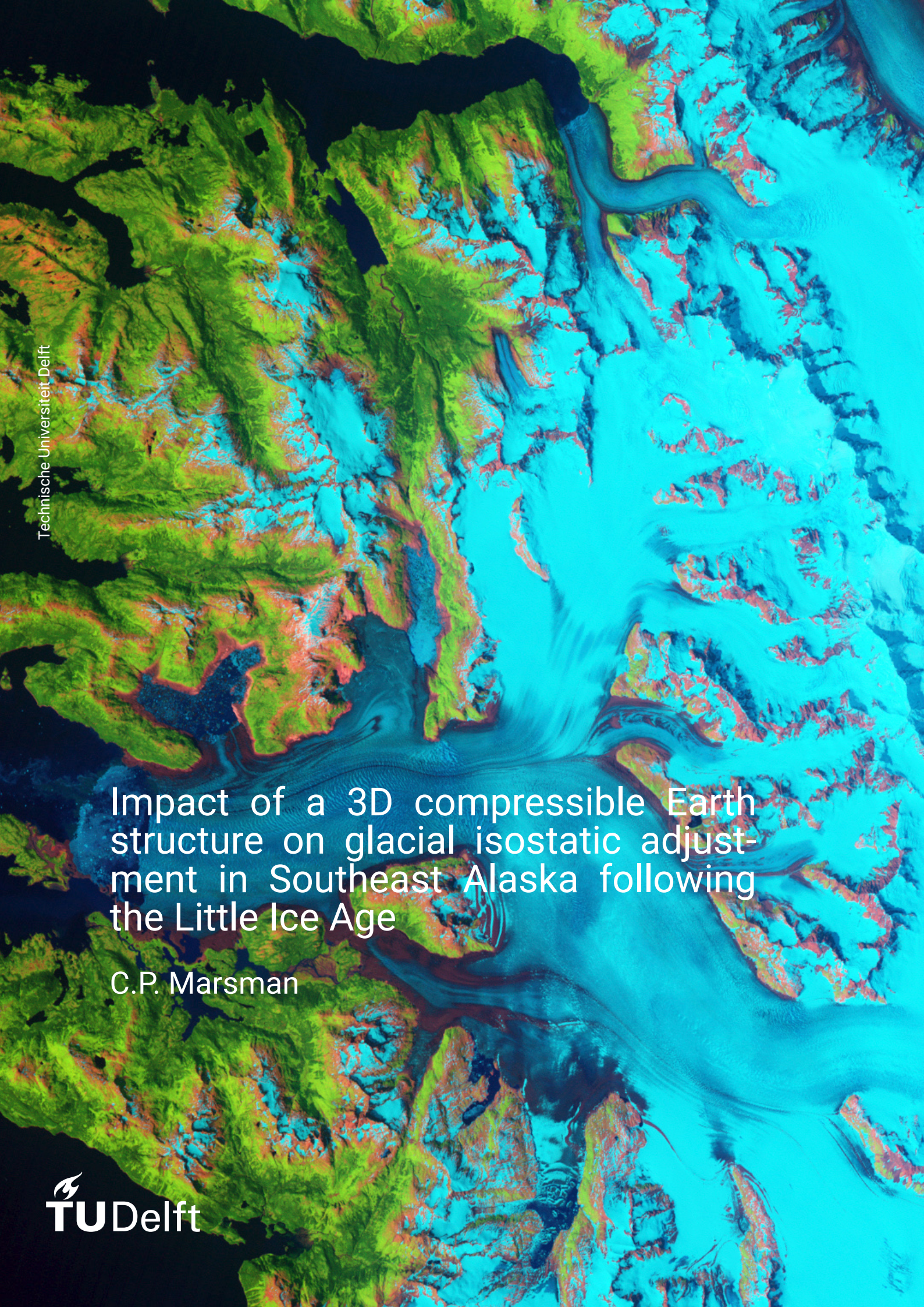

Technische Universiteit Delft

Impact of a 3D compressible Earth structure on glacial isostatic adjustment in Southeast Alaska following the Little Ice Age

C.P. Marsman

TU Delft

Impact of a 3D compressible Earth structure on glacial isostatic adjustment in Southeast Alaska following the Little Ice Age

by

C.P. Marsman

to obtain the degree of Master of Science

at the Delft University of Technology,

to be defended publicly on Friday October 9, 2020 at 14:30 PM.

Student number: 4269918

Thesis committee:

Prof. Dr. L.L.A. Vermeersen,	TU Delft, chair
Assoc. Prof. Dr. W. van der Wal,	TU Delft, supervisor
Assoc. Prof. Dr. R.E.M. Riva,	TU Delft, supervisor
Assoc. Prof. Dr. A. Barnhoorn,	TU Delft

Cover: false-color image of the Alaskan Columbia glacier, captured by Landsat satellites, obtained from `https://www.nasa.gov/image-feature/world-of-change-columbia-glacier-alaska` An

electronic version of this thesis is available at `http://repository.tudelft.nl/`.

TU Delft

Preface

In front of you lies the graduation thesis "Impact of a 3-D compressible Earth structure on glacial isostatic adjustment in Southeast Alaska following the Little Ice Age". The thesis concludes my studies, which I extended by following two master tracks, Geoscience & Remote Sensing and Space Flight Exploration at Delft University of Technology.

I had just started my thesis project when the Covid-19 crisis broke out and almost everyone around me had to work from home. In these difficult and unpredictable times, it was amazing to see how everyone was able to adapt, persevere and support each other, even when they are on the other side of the world.

The thesis was difficult and rewarding at the same time, conducting extensive research led me to answer a number of key questions. I would like to thank my daily supervisors, Wouter and Riccardo. Thank you for your guidance and support, for being critical and for taking the time to answer my questions. Additionally, I would like to thank Jeff Freymueller for the valuable input in this master thesis and for answering my many questions. Last but not least, I'd like to thank my family and friends for their support during my study period. Thank you for lifting my spirits during difficult times. Joost, thank you for our in depth discussions and for your endless support.

C.P. Marsman
Delft, September 2020

Abstract

In Southeast Alaska extreme uplift observations (> 30 mm/yr) are primarily caused by Glacial Isostatic Adjustment (GIA). The extreme uplift rates observed, are due to ice load changes since the Little Ice Age to the present in combination with a low viscosity asthenosphere ($10^{18} - 10^{19}$ Pa s). Current models have adopted a 1D stratified Earth structure, however, a simplified 1D Earth model may not be an accurate representation in this region and therefore affect the GIA predictions.

In this study a numerical model for three-dimensional (3D) GIA has been constructed for Southeast Alaska using the finite element (FE) method to study lateral variations in the upper mantle viscosity. In addition, the FE method allows for adding material compressibility using the scheme by Wu (2004), which was not possible with the previous 1D GIA models for Southeast Alaska using the TABOO software (Spada, 2003; Spada et al., 2003). The goal of this study is to present an assessment on the impact of lateral variations in the upper mantle rheology on the vertical GIA component. Two different approaches to obtain a 3D viscosity structure in the upper mantle are tested. The first approach, as described in van der Wal et al. (2013), derives the viscosity distribution through olivine flow laws. This requires experimental flow law parameters, grain size, water content and a heterogeneous temperature model. The grain size and water content are varied to find the viscosity structure that best fits the GPS data. The second approach utilizes scaling factors on shear wave velocity anomalies to derive the viscosity anomalies in a 3D structure. This approach relies on the assumption that temperature variations cause shear wave and viscosity anomalies.

Regarding the first approach, a best-fit viscosity structure with wet rheology (400 wt ppm H_2O) and grain size 8 mm is found, which are consistent with xenolith data. However, this 3D model did not yield a better fit to the GPS data than a 1D model. This is partly attributed to the temperature structure (Fullea et al. (2019) which is not consistent with findings by a regional study by Hyndman et al. (2009), in which a thinner thermal lithosphere and lower temperatures in the shallow upper mantle were found. As a result, the elastic lithosphere is much thicker than the 1D model and ultimately the 3D model severely underestimates the GIA uplift rate in this region. The second approach, where lateral viscosities were inferred directly from shear wave anomalies, yielded a better fit than the 1D model. Relatively small lateral variations improve the fit and a higher background viscosity is required to counteract the weakening effect of shear wave anomalies and compressibility. Overall, the inclusion of lateral variations decreases the residuals between 1.0-2.7 mm/yr, which is slightly above the GPS uncertainty. This demonstrates that lateral variations have a small, but measurable effect on the local GIA.

Contents

Abbreviations

GB	Glacier Bay
GIA	Glacial Isostatic Adjustment
GPS	Global Positioning System
LIA	Little Ice Age
LGM	Last Glacial Maximum
NAp	North American plate
PDIM	Present Day Ice Melt
PREM	Preliminary Reference Earth Model
SLR	Sea Level Rise
YK	Yakutat Icefields

1

Introduction

Alaska is characterized by numerous geologic phenomena. The margin of the Pacific plate in southern Alaska is one of the most active seismic regions in the world. The Pacific plate is, for a large region (i.e. the Aleutian-Alaska subduction zone, see Figure 1.1), subducting under the continental North American plate (NAp), resulting in volcanoes and intermediate to mega-thrust earthquakes. In fact, the second largest earthquake recorded, the 1964 great Alaskan earthquake with magnitude $M_w = 9.2$ took place here.

The Yakutat block (Figure 1.1) is a remnant of a tectonic plate and is much thicker than the Pacific plate. As a result, is does not subduct as much as the Aleutian slab. This micro plate is also colliding with the NAp, resulting in the Wrangell and Chugach-St Elias mountain ranges. Along the South-Eastern margin, the Pacific plate and NAp are sliding past each other, forming a strike-slip geometry.

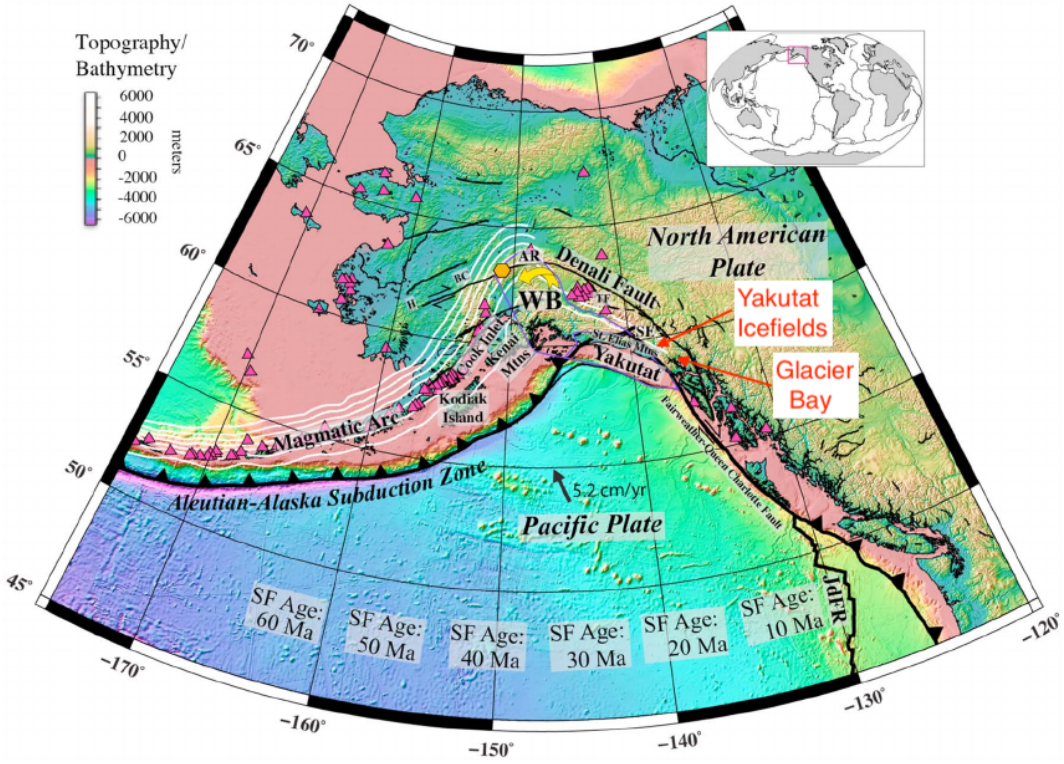

Figure 1.1: Tectonic setting of Alaska modified from Haynie and Jadamec (2017). White lines = slab contours with 40km interval, black lines = faults, orange hexagon = Denali, pink traingles = volcanoes, purple polygon outline = Yakutat oceanic plateau, WB = Wrangell block

All over Alaska significant vertical uplift occurs, both due to the subducting plate geometry and postseismic deformations from large earthquakes. However, the most rapid uplift takes place in South-East Alaska at the Yakutat Icefields and Glacier Bay (up to 32 mm/yr, e.g. Sato et al. (2011); Hu and Freymueller (2019)). The tectonic component to the vertical deformation is significantly smaller here, less than 5 mm/yr (Larsen et al., 2005). Here, rapid uplift is mostly due to unloading of mass resulting from melt of glaciers and ice caps. The process behind this is called Glacial Isostatic Adjustment (GIA). The topic of this thesis will focus on modeling GIA in Southeast Alaska.

In this chapter a number of concepts are discussed. Section 1.1 shortly introduces what GIA is, what GIA observations in Alaska are measured and how GIA is currently modelled. The current models are limited to a 1-D Earth structure, i.e. properties only vary radially. Evidence for lateral heterogeneity beneath Alaska is shown in Section 1.2 together with an explanation of how lateral variations can be incorporated in a 3D GIA model. The research questions are presented in Section 1.3. Finally, the chapter concludes with the report outline in Section 1.4.

1.1. Glacial isostatic adjustment in Alaska

Glacial Isostatic Adjustment (GIA) describes the Earth's response to changes following the mass (re-)distributions during a glacial cycle. An ice sheet for example, induces a load on a viscoelastic Earth. As depicted in Figure 1.2 the mantle material flows outward during glacier advances, resulting in subsidence near the deloading centre and uplift in the far-field. In case of glacier retreat, uplift is seen around the loading centre, while subsidence is seen in the far-field.

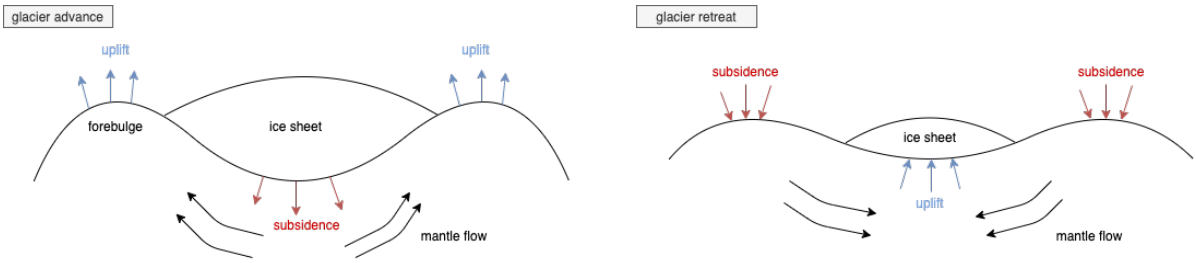

Figure 1.2: Glacial isostatic adjustment concept. During glacier advancement, a load is induced on the Earth's surface, causing subsidence around the loading centre. The underlying mantle material flows outwards and forms forbulges at the far-field. During glacier retreat, unloading causes the mantle material to flow inwards and uplift can be seen around the loading centre, whereas subsidence is seen in the far-field.

Upon deloading(i.e. ice mass loss) the Earth responds with an elastic and viscous component. The upper layer of the Earth, the lithosphere, behaves effectively as an elastic layer. The deeper part, the mantle, is also affected by the loading and is often considered to have a Maxwell viscoelastic rheology. The viscous component is a long-term response (a few years to ten thousands of years) to the unloading, depending on the ice load history and the underlying mantle properties. This means that the response of the mantle following glacial unloading includes a short-term elastic response followed by a long-term viscous response.

Studies have shown glacial rebound in North America and Scandinavia (e.g. Roy and Peltier, 2015; Barnhoorn et al., 2011) in response the ice load removal from the Last Glacial Maximum (LGM), which ended approximately 21,000 years ago. In Southeast Alaska the effects of the LGM are relatively small, 1-2 mm/yr (DeGrandpre and Freymueller, 2019). Southeast Alaska has the largest GIA rates in the North American continent, up to 32 mm/yr (Sato et al., 2011). These extreme uplift rates are, for a large portion, the result of a low viscosity zone's response to a recent colder period, the Little Ice Age (LIA), and present-day ice melt (PDIM). During the LIA glaciers expanded significantly between approximately A.D. 1200 and A.D. 1900 in Alaska (Calkin and Wiles, 1991). Since the 19th century the Alaskan glaciers have in general experienced retreat.

GIA observables in South-East Alaska

In South-East Alaska one of the fastest uplift rates have been measured related to GIA. The uplift has been monitored using GPS (both campaign style and continuous) measurements. Figure 1.3 shows the GPS observations for the periods 1992-2003 and 2003-2012. The uplift measurements show two (averaged) extreme uplift peaks of 32 mm/yr for both the Yakutat Icefield and Glacier Bay Icefield.

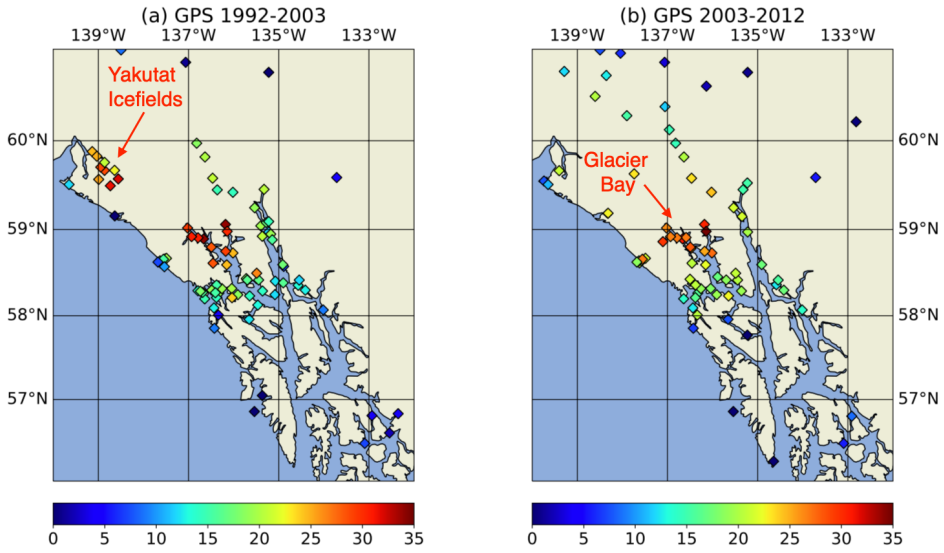

Figure 1.3: Average GPS uplift rates (mm/yr) over the periods (a) 1992-2003 and (b) 2003-2012. This is the same dataset used in Hu and Freymueller (2019)

Past studies have shown an acceleration in the GPS observables. An older GPS data analysis by Larsen et al. (2005) showed uplift peaks of 32 mm/yr and 30 mm/yr for the Yakutat Icefield and Glacier Bay, respectively. Sato et al. (2011) updated the dataset and showed that the peak at Glacier Bay increased to 32 mm/yr. Unfortunately no additional GPS measurements were available for the Yakutat area, hence, the hypothesis for an accelerated uplift for the Yakutat area could not be tested. As no significant changes occurred in the Earth structure during this time period, it is expected that the increase in uplift is due to an accelerated ice mass loss.

What processes are behind the uplift?
A number of processes contribute to the total uplift observed. These include: (i) the viscoelastic response since the Little Ice Age (LIA), (ii) the viscoelastic response since the Last Glacial Maximum (LGM), (iii) present-day ice melt (PDIM) and (iv) tectonics. The contributions of tectonics and GIA following the Pleistocene deglaciations (LGM) are estimated to be relatively small, of the order <5 mm/yr (Larsen et al., 2005) and 1-2 mm/yr (DeGrandpre and Freymueller, 2019), respectively. The majority of the uplift is due to post-LIA effects (i.e. viscoelastic response since the LIA and PDIM). Due to the heterogeneous ice history (e.g. Larsen et al., 2005; Hu and Freymueller, 2019) the elastic and viscous responses differ between the Yakutat and Glacier Bay Icefields. Larsen et al. (2005) estimated that 40% of the observed uplift near the Yakutat Icefields is related to the current ice thinning causing elastic uplift, whereas for Glacier Bay this is 15%. The elastic responses are, however, based on ice loss mass rates with a mean epoch in the 1970s (Arendt et al., 2002). Ideally, ice thinning rates should be around the same time as the period where GPS observations are measured. Sato et al. (2011) updated the ice model by including a PDIM model with mean epoch date in the 1980s and GPS measurements were between 1996 and 2006. The increased ice mass loss rates resulted in an elastic response contribution of approximately 20% in Glacier Bay.

Current GIA models for South-East Alaska

A number of studies have modelled the GIA effects due to the Little Ice Age. The majority of these studies have focused solely on South-East Alaska, where the uplift is primarily caused by GIA. Table 1.1 gives an overview of the search grid and best fit of the earth model parameters. The models described calculate the Earth's response to a glacial load using the software TABOO (Spada, 2003; Spada et al., 2003). These models are spherical, non-rotating, incompressible and self-gravitating, whereas the load is presented in glacial surface disk loads. The Earth structure is modelled using an elastic lithosphere underlain with a viscous mantle. These models have, to date, only considered an Earth with radially varying parameters. The thickness of the lithosphere, the thickness of the asthenosphere and the upper mantle viscosity are parameters under investigation. The models show that a thin lithosphere underlain with a low viscosity is required to explain the observed rapid uplift.

Table 1.1: Earth model parameters from various studies concerning southern Alaska.

Study	Lithosph.el. thickness (km)	Asthenosp. thickn. (km)	Asthenosp. visc. (Pa-s)	Upper mantle visc. (Pa-s)	Largest update -
Larsen et al. (2005)	60-70	110	$2.5 - 4.0 \times 10^{18}$	4×10^{20}	
Elliott et al. (2010)	50	110	3.7×10^{18}	4×10^{20}	GPS
Sato et al. (2011) 2-layer mantle	54	110	5.6×10^{18}	4×10^{20}	GPS + Ice model
Sato et al. (2011) 4-layer mantle	60	160	1×10^{19}	*	GPS + Ice model
Hu and Freymueller (2019)	55	230	3×10^{19}	**	GPS + Ice model

* 4 layer model: viscosities 3, 3, and 4 in units of 10^{20} Pa-s for the upper and lower parts of the upper mantle, and the lower mantle, respectively. ** set to values of the VM5a model: upper part and lower part 2.4×10^{21} ad 5×10^{21} Pa-s, respectively.

One of the larger uncertainties in these existing models is related to the PDIM. As mentioned earlier, PDIM is estimated to contribute to approximately 40% and 15% to the observed uplift rate in the Yakutat Icefields and Glacier Bay, respectively. Sato et al. (2011) used the same ice history as in Larsen et al. (2005), but terminated all LIA ice loads to zero in 2000. The elastic response was accounted for with separate PDIM models, with mean epoch older than the observation data. Hu and Freymueller (2019) implemented an accelerated ice mass loss rate for the early 21st century which could also explain the accelerated uplift observations. The increased mass loss rate results in a thicker asthenosphere and higher viscosity with respect to Sato et al. (2011). All in all, it is important to have accurate PDIM ice mass loss rates incorporated into the ice model, as these also influence the resultant rheological structure found in these GIA models. Historic glaciations are not well documented, which could also affect the obtained rheological parameters.

Another uncertainty is in the Earth's structure. The current models have only considered an Earth with radially varying parameters. In reality, Alaska has a complex tectonic setting, resulting in a laterally heterogeneous viscosity and crust structure. The next section discusses the laterally heterogeneous structure in (South-East) Alaska and how this can be incorporated into a 3D GIA model.

1.2. Lateral heterogeneity beneath South-East Alaska

The existing Little Ice Age GIA models in South-East Alaska only considered a 1-D rheology (e.g Larsen et al., 2005; Sato et al., 2011; Hu and Freymueller, 2019). The actual rheology of Alaska is far more complex and it is suggested that lateral variations in the lithosphere and mantle may effect the uplift in South-East Alaska (i.e. Larsen et al., 2005; Sato et al., 2011).

The observations of seismometers are used to infer the composition of the Earth's interior. It is commonly interpreted that fast travelling waves indicate a high temperature region and slow travelling waves indicate a much colder region. Figure 1.4 shows velocity maps at depths 80, 110, 150 and 200 km, from the global 3D shear wave velocity model by Schaeffer and Lebedev (2013). At depths 80, 110 and 150 km a reasonable contrast (>5%) can be seen between the Yakutat Icefields and the region south of Glacier Bay, whereas this contrast disappears at 200 km depth. The negative seismic anomalies indicate a relatively hot region beneath Southeast Alaska.

The temperature distribution in the upper mantle can be derived from seismic waves using scaling laws (Ivins and Sammis, 1995). Density anomalies are computed from seismic anomalies. To obtain temperature, it is assumed that density anomalies and seismic anomalies are related through a thermal expansion coefficient. The viscosity can be computed through flow laws (e.g. Hirth and Kohlstedt, 2003) where the dominant constituent of the mantle is assumed to be olivine and temperature is one of the inputs. A hot region would indicate a low viscosity structure beneath Glacier Bay. There is a change in the shear wave velocity when moving up to the Yakutat Icefields, indicating that the viscosity structure here is slightly higher. The question remains if this transition results in a large enough viscosity transition leading to a significant different response to glacial (un-)loading.

Shear wave anomalies, however, are not entirely attributed to thermal effects. Effects resulting from composition, presence of partial melt or water, and anisotropy are usually considered as second order effects, but may play an important role in local areas (e.g. Hyndman et al., 2009). To study the thermal effects on seismic wave anomalies, Wu et al. (2013) modified the scaling relationship by Ivins and Sammis (1995) to obtain viscosity anomalies from seismic wave anomalies by introducing a scaling factor. It was found that the scaling parameters increase with depth as the thermal contribution to seismic wave anomalies increases with depth

(Wu et al., 2013). However, one should be cautious when local effects (e.g. water content or partial melt) play a larger role when applying a region-wide scaling factor.

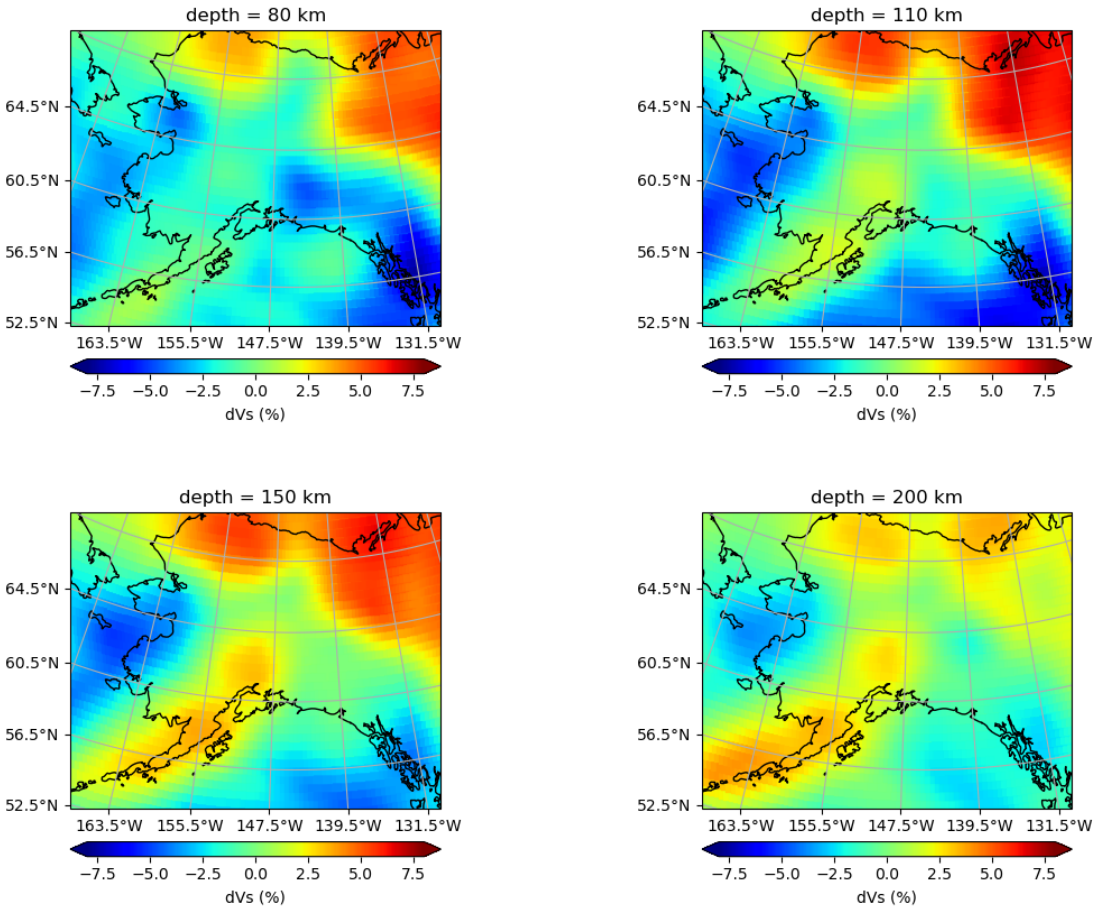

Figure 1.4: Shear wave velocity anomalies (in percentage) beneath Alaska for (a) depth = 80 km, (b) depth = 110 km, (c) depth = 200 km and (d) depth = 260 km. Dataset from Schaeffer and Lebedev (2013).

1.3. Research objective and questions

Current models use a uniformly stratified Earth model in terms of lithospheric thickness and asthenospheric viscosity and thickness. These three key parameters have been optimized to find a best fit with respect to the GIA observables. However, seismic evidence has shown that the lithospheric thickness and mantle rheology can vary laterally. Incorporating seismic observables and field geology findings has yet to be incorporated in a GIA model for Southeast Alaska.

The goal of this study is to present a model which uses seismic tomography (directly and indirectly) to derive a laterally heterogeneous (3D) viscosity structure, which could explain a number of differences in the uplift rate with respect to a radially symmetric Earth. In addition, material compressibility is taken into account in this study, which was not previously possible with GIA studies focused on Southeast Alaska using the TABOO program. Viscosities are inferred from laterally variations in temperatures through flow laws for olivine. However, there are still uncertainties associated with the temperatures and the experimental flow law parameters. In this research we investigate the effects of lateral variations in the Earth rheology through olivine flow laws. A second approach is used to compute the viscosity anomalies. The latter approach assumes that a portion of the temperature is responsible for seismic wave anomalies, which in turn are used to compute viscosity anomalies. The effect of the thermal contribution to seismic wave anomalies can be tuned to retrieve a viscosity distribution that can best explain the GIA observables. The aim of this research can be formulated in the following research question:

What is the impact of the inclusion of lateral variations in the Earth rheology in glacial isostatic adjustment models on uplift predictions in Southeast Alaska?

To help answer the research question and guide this research the following sub -research questions are posed:

1) To what extent do lateral variations affect GIA model predictions in comparison with a radially symmetric GIA model?

2) To what extent are the parameters to determine the viscosity distribution directly from mantle shear wave velocities constrained by GIA observations?

3) To what extent are experimental flow law parameters for diffusion constrained by the GIA observations?

1.4. Report outline

The first part of this dissertation introduced the topic and identified the key research objectives. The second part, Chapter 2, shapes the main section of this thesis, which is written in the form of a first version of a draft article. The article is divided into a number of subsections. Firstly, it includes a short introduction on the topic and defines the research aim, which is similar to what was explained previously. Secondly, the model setup is explained and different approaches are introduced to retrieve a 3D viscosity distribution. The article shows the findings of the results and concludes with a discussion. In addition, supplementary information (Chapter 3) is added to the article concerning a select number of topics to support the main article. Finally, the thesis report is wrapped up with conclusions answering the research questions and recommendations for future work in Chapter 4. Lastly, the report includes an Appendix explaining coordinate transformations, which was not included in the article.

2

Article

Impact of a 3D compressible Earth structure on glacial isostatic adjustment in Southeast Alaska following the Little Ice Age

C.P. Marsman, et. al.[1,2]

[1]Faculty of Civil Engineering and Geosciences, Delft University of Technology, Delft, The Netherlands
[2]Faculty of Aerospace Engineering, Delft University of Technology, Delft, The Netherlands

Corresponding author: C.P. Marsman, cpmarsman@outlook.com

Abstract

In Southeast Alaska extreme uplift rates are primarily caused by Glacial Isostatic Adjustment (GIA), as a result of ice load changes from the Little Ice Age to the present combined with a low viscosity asthenosphere. Current GIA models adopt a one-dimensional (1D) stratified Earth structure. The three-dimensional (3D) structure of the Earth is complex in this region due to the proximity of a subduction zone and the transition from a continental to oceanic plate. A simplified 1D Earth model may not be an accurate representation in this region and therefore affect the GIA predictions. In this study a numerical model for 3D GIA is constructed for Southeast Alaska. We present an assessment on the impact of lateral variations in the upper mantle rheology on the vertical GIA component. We test two different approaches to obtain a 3D viscosity structure in the upper mantle. For the first approach, viscosities are inferred from lateral variations in temperature through flow laws for olivine. The water and grain size are varied to find a viscosity structure that best fits the GPS data. We find a best-fit viscosity structure with wet rheology (400 wt ppm H_2O) and grain size 8 mm. However, this model does not perform better (in terms of χ^2) than a radially symmetric model, because predicted uplift rates are much lower than the observed values. For the second approach, we infer a viscosity distribution obtained directly from shear wave anomalies through scaling relationships. Our 3D model reduces the residuals between 1.0-2.7 mm/yr. We find that the effects of lateral variations in viscosity (up to 0.4 log units or, equivalently, a factor of 2.5) are in principle detectable by the GPS network and provide a better overall fit than a radially symmetric 1D viscosity model.

1 Introduction

Extreme uplift rates are observed in Southeast Alaska. In the early 2000s, two major peaks centered at the Yakutat Icefields (YK) and Glacier Bay (GB) exceeding 30 mm/yr have been recorded (Sato et al., 2011; Hu & Freymueller, 2019). A large portion of these uplift rates are the result of a low viscosity region's response to the decline of a recent colder period, the Little Ice Age (LIA), and elastic rebound to present-day ice melt (PDIM). The largest deglaciation event occurred in GB between 1800 and 1900 AD, which was equivalent to 8mm global sea level rise (Larsen et al., 2005). PDIM in Alaska is a significant contributor to global mean sea level rise, i.e. 53.4 ± 13.8 Gt/yr (equivalent to 0.15 mm/yr) between 2002 and 2016 (Wouters et al., 2019), adding up to roughly 10% of the global ocean mass change. Due to an accelerating ice mass loss, the contribution to global ocean mass change is expected to increase. The effects of glacier melt do not remain limited to sea level rise. The glacial unloading can affect fault stability, increasing the stress leading to increased seismicity rates (Sauber & Molnia, 2004).

To model the Earth's viscoelastic response to changes in ice loading, previous GIA studies (e.g., Larsen et al., 2005; Sato et al., 2011; Hu & Freymueller, 2019) have optimized three key parameters, i.e. the effective elastic lithospheric thickness, the asthenospheric viscosity and thickness, to improve the fit with respect to the GIA observables. Larsen et al. (2005) set up a uniformly stratified, non-rotating, self-gravitating, incompressible spherical Maxwell viscoelastic Earth model using the TABOO progam (Spada, 2003; Spada et al., 2003). Subsequent studies (e.g., Elliott et al., 2010; Sato et al., 2011; Hu & Freymueller, 2019) added new GPS data, increased the spatial resolution and updated the ice load model to account for the increasing PDIM, explaining differences in the obtained parameters. Increasing PDIM rates result in a thinner lithosphere underlain with a higher upper mantle viscosity than previous models (Hu & Freymueller, 2019). Overall, a thin lithosphere (50-70 km) underlain with a low viscosity asthenosphere ($2.5 \times 10^{18} - 3 \times 10^{19}$ Pa-s) is preferred. However, a select number of areas show either underprediction (e.g. the Yakutat Icefields) or overprediction (e.g. Haines to Juneau) (Hu & Freymueller, 2019). Error sources are likely from systematic errors in the ice load model or from an inaccurate earth model.

Southeast Alaska is near a subduction zone and it is considered "tectonically stable", i.e. the vertical uplift due to tectonics is relatively small (Larsen et al., 2005), making this region a good calibration area for GIA in Alaska. Previous GIA studies focused on Southeast Alaska have only considered a radially symmetric Earth. In reality, the Earth is far more complex and lateral variations in the Earth structure can have significant effects on GIA (e.g. van der Wal et al., 2013; Nield et al., 2018). Lateral variations have yet to be included in a GIA model for Southeast Alaska and it is currently unknown what the sensitivity of uplift predictions is to a heterogeneous Earth. Moreover, 3D studies can provide more insights on the interior structure and processes within the Earth for this region.

In this work a 3D GIA model is constructed using the finite element method (FEM). The FEM method enables addition of material compressibility by using the scheme by Wu (2004), which was not possible with the previous 1D GIA models. A heterogeneous Earth is deployed using a 3D viscosity structure in the upper mantle. In this research we test two approaches to derive a 3D viscosity distribution, as uncertainties related to both approaches are not well known. The first approach, as described in van der Wal et al. (2013), derives the viscosity distribution through olivine flow laws, which requires experimental flow law parameters, grain size, water content and a (heterogeneous) temperature model. In the second approach, lateral viscosities are derived by a method that uses scaling factors on shear wave velocity anomalies in a seismic tomography model (Ivins & Sammis, 1995). Here, we tune the contribution of shear wave anomalies to viscosity anomalies using the method

by Wu et al. (2013). In addition, flow law parameters, and background temperature and viscosity profiles are required. We aim to answer the following research questions:

a) To what extent do lateral variations affect GIA model predictions in comparison with a radially symmetric GIA model?
b) To what extent are experimental flow law parameters for diffusion constrained by the GIA observations?
c) To what extent are the parameters to determine the viscosity distribution directly from mantle shear wave velocities constrained by GIA observations?

Section 2.1 of this paper explains the FEM model setup and the Earth model parameters. Section 2.2 and Section 2.3 describe the methods to retrieve a 3D viscosity distribution using seismic tomography and flow laws. Section 2.4 presents the ice load model and how it is applied to the FE grid. The effective viscosities are shown in Section 4.1 and the effect of select viscosity profiles on uplift rate are discussed in Section 4.2. Model evaluation and comparisons are made in Sections 4.3 and 4.3, respectively. A number of model imitations are mentioned in Section 4.5. The paper is wrapped up with a conclusion.

2 Methodology

2.1 Finite element method and model

In this research the finite element (FE) method is used to model deformation and stress in the Earth with the commercial FE package Abaqus FEA (Hibbitt et al., 2016), following the approach by Wu (2004). The GIA model in this research adopts a flat-Earth approximation. The validity of the flat-Earth approximation was shown in Wu and Johnston (1998) for loads up to the size of the Fennoscandian ice sheet. Hence, the flat-Earth assumption is reasonable considering the smaller extent of the ice load in Alaska since the LIA. In addition, material compressibility is assumed and effects by density perturbations are neglected. From now on we refer to a compressible model where only material compressibility is implemented. The effects of a compressible model versus an incompressible model is analyzed in the Supplementary Information. Moreover, self-gravitation is neglected. Amelung and Wolf (1994) showed the effect of neglecting self-gravitation is partly counteracted by the flat-Earth approximation, which was also confirmed in Spada et al. (2011) and Schotman et al. (2008).

The incompressible flat-Earth FE model has been benchmarked with the normal-mode (NM) model by Hu and Freymueller (2019) (see Supplementary Information). The FE and NM models show good agreement, where most of the difference are smaller than 1 mm/yr.

The largest differences (up to 2.5 mm/yr) are near the Yakutat Icefields, which are likely due to smoothing of the ice load model in the FE grid and differences in relaxation times between the FE and NM models. In addition, tests were performed on the FE model resolution with 10 and 15 km. The NM model uses spherical harmonics with maximum order and degree of 2048 (∼10 km). the 10 km FE resolution model did not yield significantly better results than the 15 km resolution test (differences less than 0.5 mm/yr) and resulted in much longer computational times. For that reason, the 15 km resolution was used in further simulations. For further details the reader is referred to the Supplementary Information.

The model geometry is based on work by Schotman et al. (2009) and Barnhoorn et al. (2011). The loading area consists of 155 x 95 elements with a resolution of 15 x 15 km. This high spatial resolution is required by the ice load model (see Section 2.4). Deeper layers (starting from 90 km) have a coarser resolution: 31 x 19 elements of 75 x 75 km. Figure 1 shows the model surface geometry. The total surface area of the model is 20,000 x 20,000 km and the model extends to a depth of 10,000 km in order to minimize boundary effects. In total, 26 finite element layers are created, which gives a total of 198,530 elements. The bottom and vertical edges are prescribed with boundary conditions such that the bottom edge is fixed and the sides are limited to vertical translation. Winkler foundations (Wu, 2004) are applied at the Earth's surface and internal boundaries where density jumps occur.

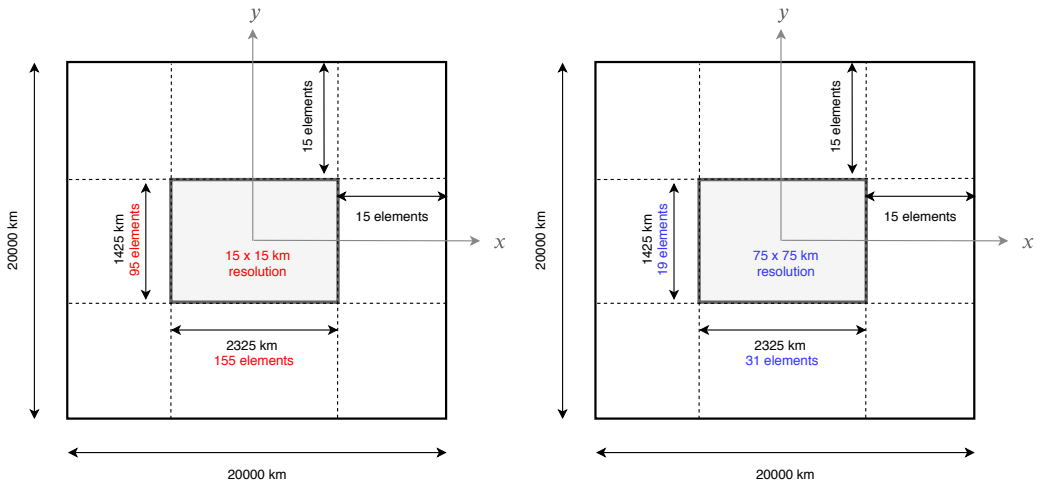

(a) From 0 to 90 km depth

(b) From 90 km to bottom

Figure 1: XY model geometry

The outer vertical layers of the model have a higher resolution, whereas the inner layers have lower resolution. The resolution of these two parts are chosen such that an even amount of bricks of the higher resolution part fit exactly on the top surface of the lower resolution part. Considering the mismatch in nodes and the fact that Abaqus does not

provide a standard element to model this, tie constraints are applied at the two surfaces where resolution jumps occur, using the Abaqus keyword *TIE. The tie constraints allows for all active degrees of freedom to be equal for both surfaces. The two surfaces are defined by the upper and lower element surfaces of the two layers, respectively. The outer vertical edge elements are not taken into account as these element nodes already have a fixed constraint.

The Earth model parameters are described in Table 1. The density and shear modulus are derived through volume-averaging the PREM model (Dziewonski & Anderson, 1981). The Young's modulus E is required as input by Abaqus and is computed using $E = 2G(1 + \upsilon)$, where υ is the Poisson's ratio. Durkin et al. (2019) used the LITHO1.0 model (Pasyanos et al., 2014) to infer variations in the density and elastic structure and showed that lateral variations have a small effect on the elastic uplift. We therefore do not include a heterogeneous density and elastic structure. Material compressibility is incorporated and the Poisson's ratio varies with depth between 0.26 and 0.30.

The upper three layers (depth <40 km) are considered fully elastic. Below 400 km depth, the rheology is only varying with depth and values from the VM5a rheology model (Peltier et al., 2015) are adopted. (Sato et al., 2011) showed that GIA is less sensitive to deeper viscosities due to the short wavelength of ice the load involved. Therefore, we consider it reasonable to infer viscosities of a global reference model below 400 km depth. Below 40 km and above 400 km depth, each individual element is assigned to an individual viscosity value. The next sections explain two approaches to assign 3D viscosity. The first approach uses creep flow laws to assign creep parameters to each individual element. The second approach converts shear wave anomalies into viscosity.

2.2 Upper mantle rheology derived from flow law parameters

For the first approach, creep parameters are retrieved using the methodology in van der Wal et al. (2013). We assume that the main constituent of the mantle material up to 400 km depth is olivine (Turcotte & Schubert, 2002) and assume this controls the deformation in the mantle. Diffusion creep and dislocation creep are described using a general flow law for olivine, where the strain rate depends on stress to a certain power (Hirth & Kohlstedt, 2003):

$$\dot{\epsilon} = A\sigma^n d^{-p} f H_2O^r \exp\left(-\frac{E + PV}{RT}\right) \tag{1}$$

where $\dot{\epsilon}$ is the strain rate, A is a constant, σ the induced stress to a power n, d the grain size to a power $-p$, fH_2O the water content to a power r, E the activation energy, P the pressure, R, the gas constant, and T the absolute temperature. Note that partial melt

Table 1: Model layers and Earth parameters. Density and Young's modulus are derived from volume-averaged PREM values. Viscosity from 400km depth follows the VM5a rheology model. The rheology between 40 and 400 km depth are determined through flow laws for olivine. T.B.D. = to be determined.

Top of layer radius (km)	Layer thickness (km)	Density (kg/m^3)	Rigidity (GPa)	Young's modulus (GPa)	Poisson's ratio (-)	Viscosity (Pa s)
6371	12	2171.5	26.6	68.1	0.28	-
6359	14	2885.1	42.8	109.6	0.28	-
6345	14	3380.3	68.1	174.4	0.28	-
6331	15	3378.0	67.8	174.2	0.28	T.B.D.
6316	15	3376.6	67.7	173.5	0.28	T.B.D.
6301	20	3375.2	67.5	172.9	0.28	T.B.D.
6281	20	3372.5	67.1	171.8	0.28	T.B.D.
6261	20	3370.9	66.9	171.0	0.28	T.B.D.
6241	20	3369.2	66.7	170.1	0.27	T.B.D.
6221	20	3365.8	66.3	168.8	0.27	T.B.D.
6201	20	3372.9	67.1	170.4	0.27	T.B.D.
6181	20	3380.0	67.9	172.0	0.27	T.B.D.
6161	20	3416.2	71.5	180.8	0.26	T.B.D.
6141	20	3452.4	75.1	189.5	0.26	T.B.D.
6121	40	3463.7	75.8	190.7	0.26	T.B.D.
6081	50	3486.1	77.1	199.3	0.29	T.B.D.
6031	60	3706.4	92.4	239.5	0.30	T.B.D.
5971	135	3781.5	116.4	302.3	0.30	$5.0 \cdot 10^{20}$
5836	135	3950.7	117.9	304.6	0.29	$5.0 \cdot 10^{20}$
5701	250	4443.9	170.1	439.2	0.29	$1.6 \cdot 10^{21}$
5451	250	4590.3	188.5	479.4	0.27	$1.6 \cdot 10^{21}$
5201	430	4780.0	208.8	533.8	0.28	$3.2 \cdot 10^{21}$
4771	430	5008.7	233.7	601.6	0.29	$3.2 \cdot 10^{21}$
4341	430	5227.8	258.4	668.5	0.29	$3.2 \cdot 10^{21}$
3911	431	5444.1	283.4	736.6	0.30	$3.2 \cdot 10^{21}$
3480	3480	10925.0	-	-	-	-

is ignored in this study and omitted from Equation 1. In case of diffusion creep, a linear relation exists between the stress and strain rate, and thus the power is 1. When speaking of dislocation creep, the problem becomes non-linear, where the power is approximately 3.5 (e.g., Whitehouse, 2018). Moreover, we have looked into crustal rheology which may influence the uplift rates. We have tested a flow law for the crust (<55 km) (described in the Supplementary Information Section 4), however, inferred viscosities are too high such that the crust behaves elastically.

Diffusion and dislocation creep parameters are assigned to each FE element (B_{diff} and B_{disl}) and the effective viscosity can be computed with (van der Wal et al., 2013):

$$\eta_{eff} = \frac{1}{3B_{diff} + 3B_{disl}q^{n-1}}, \tag{2}$$

where B_{diff} and B_{disl} are the diffusion and dislocation creep parameters, respectively, and $q = \sqrt{\frac{3}{2}\sigma'_{ij}\sigma'_{ij}}$ is the Von Mises stress. The B parameters contain the parameters in Equation 1 such that $B = Ad^{-p}fH_2O^r \exp\left(-\frac{E+PV}{RT}\right)$. In this study only diffusion creep is considered as it is unknown if the stress-state in this region affects the effective viscosity. This was chosen due to the tectonic origin of the region where background stresses may affect a stress-dependent viscosity. On the other hand, in presence of large background stresses, stress changes due to GIA have less effect on the effective viscosity (van der Wal et al., 2013) and the GIA process is effectively linear (Schmidt, 2012). The input parameters for the creep parameters are taken from Hirth and Kohlstedt (2003), which are depicted in Table 2. Note that the pre-factor A for wet rheologies is reduced by a factor 3 as done in Behn et al. (2009) and Freed et al. (2012) due to calibration for water content in olivine (Bell et al., 2003).

Table 2: Rheological parameters for diffusion creep mechanisms for wet and dry rheology settings. Values from (Hirth & Kohlstedt, 2003). $^{(a)}$The pre-factor A for wet rheologies in reduced by a factor 3 following (Behn et al., 2009; Freed et al., 2012) due to calibration for water content in olivine

No.	A	E (kJ/mol)	V (10^{-6} m^3/mol)	r	n	p	wet/dry
1	1.5×10^9	375	5	-	1	3	dry
2	$^{(a)}3.33 \times 10^5$	335	4	1	1	3	wet

The viscosity profiles are tuned with the grain size and water content, which do not vary laterally or with depth. Partial melt is ignored in thus study, but may be important in select local areas beneath volcanic zones (Hyndman, 2017). Typical grain sizes found in peridotite-gabbros in Southeastern Alaska are 1-4 mm (Himmelberg et al., 1986; Himmelberg & Loney, 1986) but can lead up to 10 mm (Morales & Tommasi, 2011), hence the grain size in this study is varied between 1-10 mm. Both dry and wet rheology settings are considered. However, there is a preference for a wet rheology setting. Laboratory experiments show that the presence of water significantly weaken the olivine material (e.g., Hirth & Kohlstedt, 2003). In Dixon et al. (2004) evidence is shown for low viscosities beneath western Unites States, which are attributed to the subducting oceanic plate hydrating the upper mantle, and concluded that the presence of water is required to explain such low viscosities.

WINTERC-3D (Fullea et al., 2019) provides a preliminary global reference temperature model. This model uses joint inversion of different data sources to map the temperature globally at 56 km, 80km, 110 km, 150 km, 200 km, 260 km and 330 km. The global shear wave velocity model, SL2013sv (Schaeffer & Lebedev, 2013), and globally averaged xenolith/peridotite data of different ages are used to derive the temperature. Temperature maps at select depths can be seen in Figure 2. Lateral variations in temperature between YK and GB are minimal in comparison to lateral variations towards the upper-east, where the Aleutian slab in subducting underneath the North-American plate. Around 100 km depth the temperatures between YK and GB are quite similar. The temperature differences between the two is maximum around 200 km depth ($\sim 100°C$). The question remains if these temperature differences are large enough to cause significant viscosity differences. At 370 km depth lateral variation decreases. Overall, the Cordillera is a hot region (>1500°C beneath 200 km). Approximately from 100 km depth temperatures are increasing according the adiabatic temperature gradient.

The averaged temperature profile underneath Southeast Alaska from interpolated values of WINTERC-3D are shown in Figure 3, along with temperature profiles by Hyndman et al. (2009) (regional) and Stacey and Davis (2008) (global average). The temperature profile by Stacey and Davis (2008) is not representative of Southeast Alaska as its geotherm follows a much older and thus thicker thermal lithosphere. The shallow upper mantle temperatures are thus too low and as a result viscosities would be higher. The temperature profile obtained with WINTERC-3D shows high temperatures and a thermal lithospheric thickness of approximately 90 km. A regional study by Hyndman et al. (2009) computed the temperatures from the NA04 North American shear wave velocity model (van der Lee & Frederiksen, 2005) following the method by Goes and Govers (2000). Hyndman et al. (2009) incorporated a thermally-dependent anelastic correction, resulting in lower temperatures. The thermal lithosphere is approximately 60 km and below it follows the adiabatic gradient approximately. When comparing the regional study with the WINTERC-3D profile, it seems that temperatures by WINTERC-3D are overestimated. Differences can be explained due to the different shear wave velocity models, methods and compositions used. Neglecting the importance of anelastic effects in a high temperature region could lead to higher temperatures in WINTERC-3D. Moreover, both models do not include effects of water content or partial melt. Both parameters cause a reduction in seismic velocities and temperatures could be overestimated (Hyndman et al., 2009). Hyndman et al. (2009) estimates that temperatures could be 50°C too high for the Cordillera.

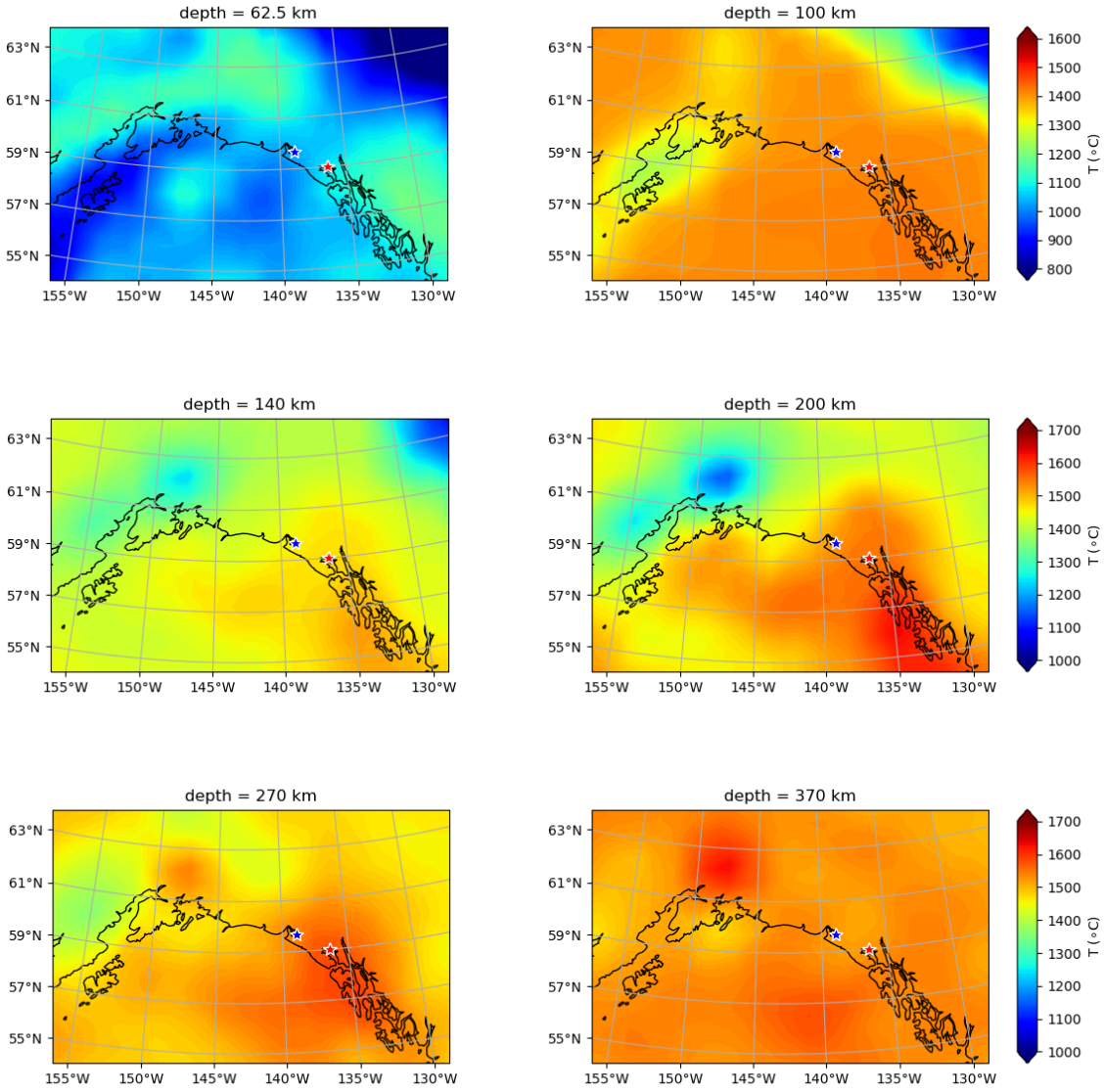

Figure 2: Temperature maps at selected depths from interpolated values in WINTERC-3D (Fullea et al., 2019). The blue and red stars correspond to the peak uplift in the Yakutat Icefields and Glacier Bay, respectively. Take note of the different scales used in the upper two plots.

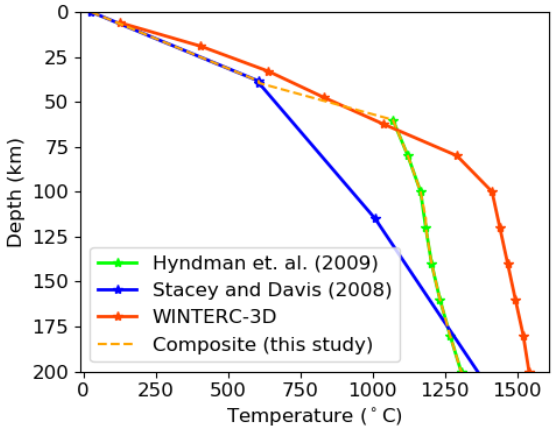

Figure 3: Averaged temperature profiles by (1) Hyndman et al. (2009) for Northern Cordillera and (2) WINTERC-3D (Fullea et al., 2019). The WINTERC-3D temperatures are averaged within the area bounded by latitudes 58°N - 60°N, and longitudes 135°W - 141°N. The temperature profile by (Hyndman et al., 2009) (Model C8) represents the upper mantle temperatures beneath the Cordillera.

2.3 Upper mantle rheology inferred from seismic velocity anomalies

Previously, lateral variations in viscosity were inferred from a 3D viscosity distribution through flow laws. Another approach to estimate the 3D viscosity structure is directly through seismic tomography as described in the approach by Wu et al. (2013). In the crust seismic anomalies are mainly controlled by composition, whereas in the upper mantle seismic wave anomalies are for a large portion controlled by temperature (Hyndman, 2017). Assuming that temperature anomalies are responsible for viscosity anomalies, Ivins and Sammis (1995) introduced a scaling relationship that computes viscosity anomalies based on the effect of temperature and mineral physics. Wu et al. (2013) slightly modified this relationship and included a parameter to scale the viscosity anomaly based on the thermal contribution. The scaling relationship is given by (Wu et al., 2013):

$$\log_{10}(\Delta\eta) = \frac{-\log(e)\beta}{[\partial \ln \nu_S / \partial T]_{tot}} \frac{E + PV}{RT_0^2} \frac{\delta\nu_S}{\nu_{S_0}}, \tag{3}$$

in which β is a scaling factor representing the thermal contribution on shear wave anomalies, T_0 the background temperature profile (1D), E is the activation energy, P is the pressure, V is the activation volume, R is the gas constant, $\frac{\delta\nu_S}{\nu_{S_0}}$ is the fractional shear wave anomaly computed with respect to the reference seismic anomaly profile ν_{S_0}, and $[\partial \ln \nu_S / \partial T]_{tot}$ is the velocity derivative with respect to temperature accounting for both

anharmonic and anelastic effects, which are explained later. The absolute viscosity is then related to the background viscosity and the viscosity anomalies with $\Delta\eta \equiv \eta/\eta_0$.

Anharmonicity refers to the process where elastic constants change due to temperature caused by deviations in lattice vibrations from a harmonic oscillator (e.g. Karato & Karki, 2001). As a result of higher temperatures, the equilibrium spacing between atomic bonds is increased, which is called thermal expansion. Anelasticity is a process that describes the dissipation of energy in a material under stress, resulting in decay of the amplitude of seismic waves. It is an important process to consider when computing temperature, as temperature derivatives are significantly increased due to the effect of anelasticity (Karato, 1993). The velocity derivatives are taken from Table 20.2 in Karato (2008), which represent global averages. It should be taken note that global averages may produce a bias for Southeast Alaska. Anelasticity is expected to play a larger role in this area due to the higher temperatures involved (Hyndman et al., 2009). Also, if indeed the mantle is substantially hydrated, the increased water content will enhance the anelasticity effects (Hyndman et al., 2009). If anelastic effects are not taken into account (or not enough), temperatures could be overestimated and in turn result in lower viscosities. Uncertainties related to the effect of the composition, water content and partial melt, are not considered in this study and may also affect the β parameter.

2.3.1 Shear wave velocity anomaly maps

The seismic anomalies are taken from the global shear wave velocity model SL2013sv (Schaeffer & Lebedev, 2013). The seismic anomalies over all Alaska are shown in Figure 4 at depths 80, 110, 150 and 200 km. At depths 80, 110 and 150 km a reasonable contrast (>5%) can be seen between YK and the region south of GB, whereas this contrast disappears at 200 km depth. The negative shear wave velocity anomalies in Southeast Alaska result in lower viscosities and thus have a weakening effect on the upper mantle strength.

2.3.2 Baseline parameter selection

The search space in this study is limited to the background viscosity profile and the β parameter in the upper mantle. We limit the search grid to the upper mantle as GIA does not constrain deeper viscosities due to the short wavelength of the regional deglaciation (Larsen et al., 2005; Sato et al., 2011; Hu & Freymueller, 2019).

The 1D background temperature profile is a composite of the globally averaged profile by Stacey and Davis (2008) and the regional study by Hyndman et al. (2009). Between 0 and 60 km depth, temperatures are taken from Stacey and Davis (2008), between 60 and 200 km the temperatures from Hyndman et al. (2009) (model C8 in their appendix) are taken

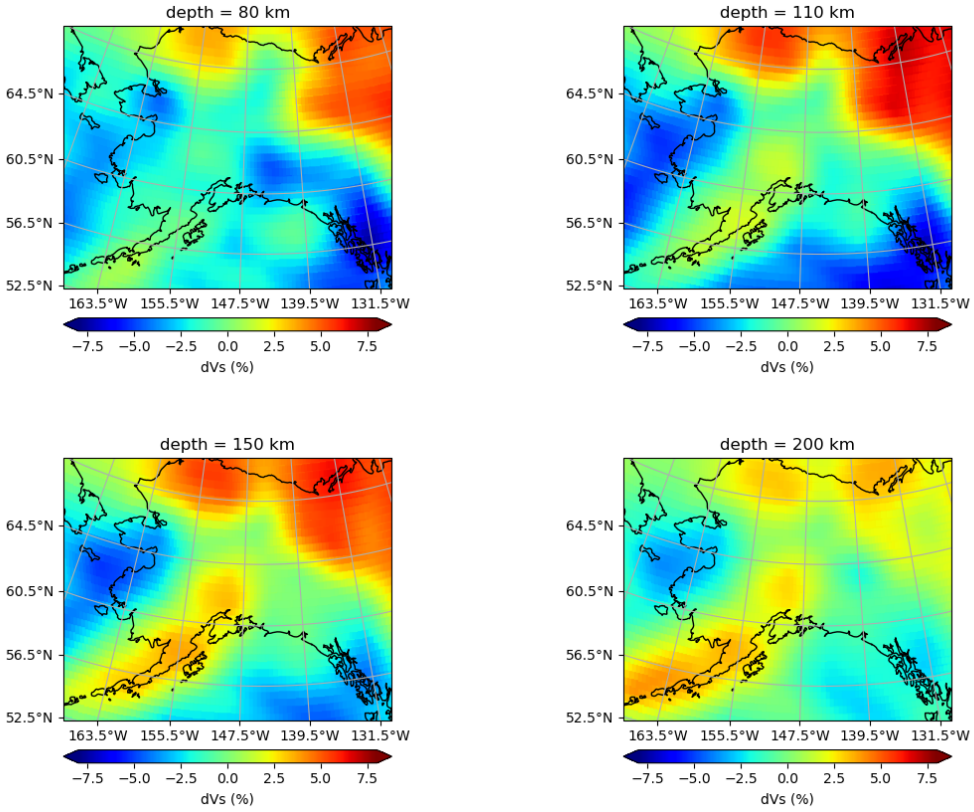

Figure 4: Shear wave velocity anomalies (in percentage) beneath Alaska for (a) depth = 80 km, (b) depth = 110 km, (c) depth = 200 km and (d) depth = 260 km. Dataset from Schaeffer and Lebedev (2013).

and bellow 200 km the temperature follows the adiabatic gradient of 0.4 K/km. Choosing the background viscosity should be done carefully. The VM5a viscosity structure is not suitable for this area due to the relatively high viscosity in the upper mantle: 1×10^{22} Pa s between 60 and 100 km opposed the to range ($2.5 \times 10^{18} - 3 \times 10^{19}$ Pa s) found in regional GIA studies (i.e. Larsen et al., 2005; Sato et al., 2011; Hu & Freymueller, 2019). We choose to select the viscosity found in the best-fit model by Hu and Freymueller (2019) as the baseline in our analysis. Here, the elastic lithosphere is 55 km thick and the asthenosphere is 230 km thick with a viscosity of 3×10^{19} Pa s. In this study, only the viscosity in the asthenosphere is varied. It is expected that the viscosity at this depth has the largest effect on uplift due to the short wavelength of the ice load. As the shear wave velocity anomalies have a weakening effect on the viscosity structure beneath Southeast Alaska, the background viscosity in increased subsequently until a best-fit model is found.

2.4 Ice load model

Upon deloading of ice, the Earth responds in with an instantaneous elastic response and a time-delayed viscous response. The timescales associated to the viscous flow is related to the (Maxwell) relaxation time of the mantle. Due to the presence of a low viscosity asthenosphere, the associated relaxation times are decadal to years, making it difficult to separate these two components. For that reason, both LIA and PDIM effects are modelled together in the ice model. PDIM has a large contribution to the current uplift rates observed, PDIM effects lead up to 45% and 25% for YK and GB, respectively (see Supplementary Information Section 3), which are larger than the values found in Larsen et al. (2005).

The ice history is adopted from Hu and Freymueller (2019), where the interpolated late 20th century ice load changes from Berthier et al. (2010) (see Figure 5) were used to assemble to ice load model. The late 20th century ice load changes represent the ice wastage between the 1962 and 2006. Subsequently, to compute the load history, the same methods in Larsen et al. (2005) are applied. The ice load history is assumed to be a function of space and time (Hu & Freymueller, 2019):

$$LOAD(x,t) = L_1(x) \cdot L_2(t), \tag{4}$$

in which L_1 and L_2 are functions of space (x) and time (t), respectively. The ice load history can be seen in Figure 6. The Earth model is subjected to two ice load models: (i) a regional model covering the majority of the Alaskan glaciers and (ii) a GB ice load model describing the non-synchronous behaviour of the GB icefield. An inferred ice loss of 3030 km^3 since the collapse of the GB icefield is the largest post-LIA unloading known (Larsen et al., 2005). Another exception in the ice load behaviour is made to the YK Icefields, which experienced a rapid ice wastage starting in the 20th century. Essentially, the ice model for YK follows the same pattern as the regional model, only with and enhanced ice wastage starting in the late 20th century. The enhancement, which is 3 times the rate of the regional model, was implemented on three load disks defined in the ice load model for the spherical GIA model.

In order to describe the present day ice loading, the Berthier model is extrapolated to the year 2012. It was chosen to stop the model here due to the vertical deformation component being contaminated by post-seismic deformation from two large earthquakes on 5 January 2013 (Mw 7.5) and 28 October 2012 (Mw 7.5) (Hu & Freymueller, 2019). To account for the accelerated mass loss from 1995 to 2012, the average late 20th century rates are multiplied by a scaling factor. Hu and Freymueller (2019) showed scaling factors of 1.8

and 2.2 for the periods 1995-2003 and 2003-2012, respectively, yielded an accurate representation of the enhanced ice loss, which was inline with the GPS observations.

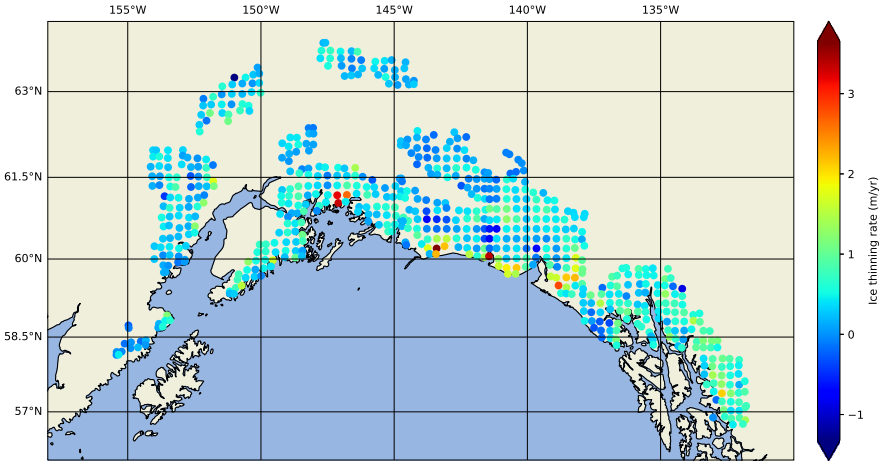

Figure 5: Interpolated ice thinning rates in the late 20th century from Berthier et al. (2010). Data obtained from Hu and Freymueller (2019). The ice thinning rates in (Berthier et al., 2010) represent the regional ice thinning rates in Alaska between 1962 and 2006. Note that the disk radius are not projected in this map, instead the markers have equal size.

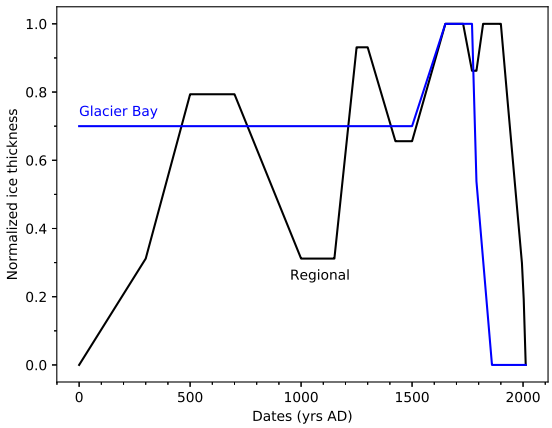

Figure 6: Glacier load history defined for a regional and GB model. The same methods as in Larsen et al. (2005) and Hu and Freymueller (2019) are applied.

The regional ice load model is given by 677 disks with radii between 10 and 11 km, whereas the GB ice load model is presented with an additional 5 disks with radii between 13 and 19.5 km. This loading is converted to the FE grid, while conserving mass. The

ice thickness is converted to mass according to $m_d = \rho_{ice}\pi r_d^2 h_d$, where m is the mass, ρ_{ice} the ice density, h the ice height and the subscript d referring to the disk. The ice density is 850 kg/m^3, the same value used in Hu and Freymueller (2019). Subsequently, the mass from each disk is divided onto the rectangular grid cells of the FE mesh. Essentially, the (fraction) of each disk is assigned to a rectangular grid cell. The mesh size should be small enough so that errors around the ice load edges are minimized. Our benchmark analysis (see Supplementary Information) showed a resolution of 10 km was not substantially superior to a 15 km resolution. We therefore selected a 15 km grid to also reduce the computational times of our models. The ice load is implemented in Abaqus using pressure loads, hence to mass is converted to pressure with $P = \frac{m_g g}{A}$, where P is the pressure load, m_g the total mass assigned to a grid cell, g the gravitational acceleration and A the surface area of a grid cell.

3 GPS data

To date, one of the fastest uplift rates related to GIA have been measured in Southeast Alaska. The uplift has been monitored using GPS (both campaign style and continuous) measurements. Figure 7 shows the GPS observations for the periods 1992-2003 and 2003-2012. The uplift measurements show two (averaged) extreme uplift peaks of 32 mm/yr for both YK and GB.

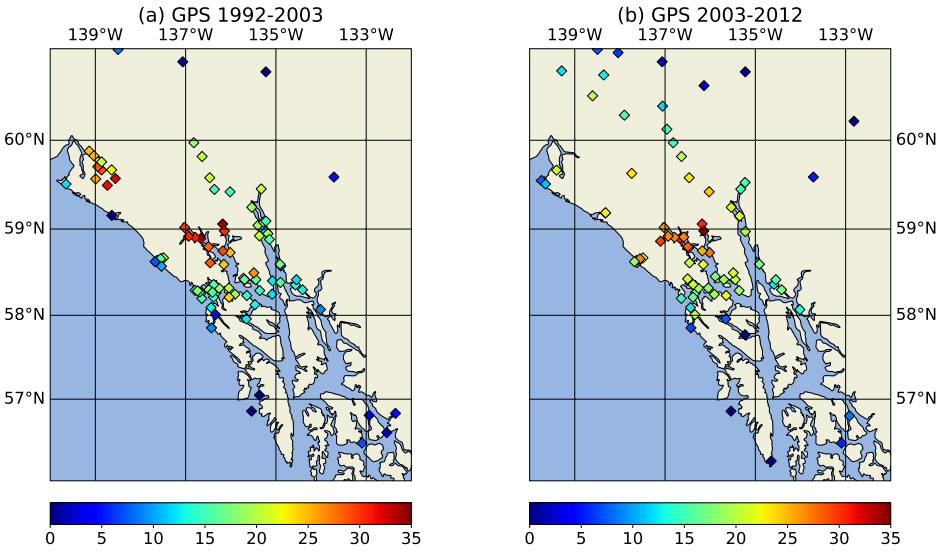

Figure 7: Average GPS uplift rates (mm/yr) over the periods (a) 1992-2003 and (b) 2003-2012. This is a slightly updated GPS dataset than used in (Hu & Freymueller, 2019) (Jeff Freymueller, personal communication)

Past studies have shown an acceleration is the GPS observables. A GPS data analysis by (Larsen et al., 2005) showed uplift peaks of 32 mm/yr and 30 mm/yr for YK and GB, respectively. (Sato et al., 2011) extended the dataset and showed that the peak at GB increased to 32 mm/yr. Unfortunately, no additional GPS measurements were available for YK, hence, the hypothesis for an accelerated uplift for YK could not be tested. It is expected that the increase in uplift is due to an accelerated ice mass loss.

Most of the GPS uncertainties are between 1-2 mm/yr but a select number of points have larger uncertainties between 5-8 mm/yr (see Supplementary Figure S1). The GPS dataset includes measurements of 115 GPS stations, of which 55 stations have measurements for both periods 1995-2003 and 2003-2012. For 29 stations, the difference in velocity is larger than the uncertainty with respect to the measurements. 20 stations show an increase in velocity, whereas 9 show a decrease. The difference in velocities (between Figure 7a and 7b) and their respective uncertainties are plotted in Figure 8 along with a histogram. There is also a spatial pattern to the increase or decrease in the observed uplift. Generally, GPS sites along the Western side of GB show a decrease, whereas more inland sites show an acceleration (Hu & Freymueller, 2019). For more information on the GPS dataset, the reader is referred to Hu and Freymueller (2019).

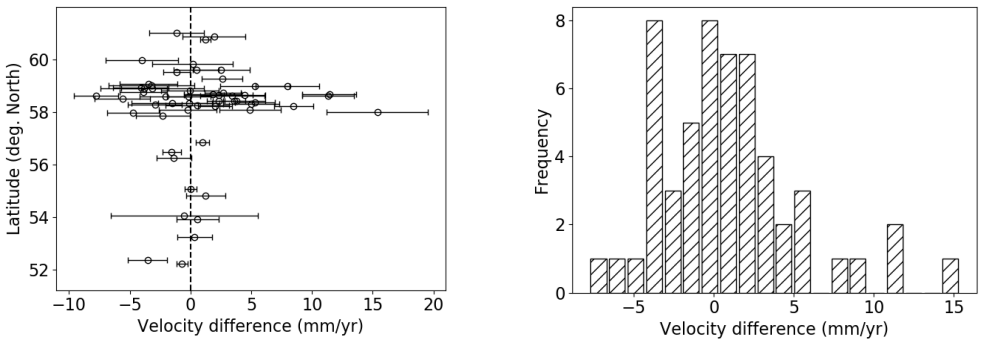

(a) (b)

Figure 8: (a) Difference in velocity measurements between 1995-2003 and 2003-2012 and (b) the corresponding histogram. The uncertainties in (a) were obtained by adding the velocity uncertainties in quadrature then taking the root square.

4 Results and Discussion

4.1 Effective viscosity

The viscosity profiles obtained with the first approach, using flow laws for olivine, are shown in Figure 9. Note that for each combination of parameters, two profiles are given which represent the extent of the viscosity distribution. The 3D temperature model is used to implement lateral variations in the viscosity structure. The grain size and water content are varied. A number of comments can be made on the vertical profiles. First of all, the largest viscosity jumps occur within 100 km depth. This can be explained with the thermal profile in Figure 3 where the thermal lithosphere is approximately 100 km. As a result the 3D models here have a much thicker elastic lid than the 1D model in (Hu & Freymueller, 2019). Below 100 km the temperature is increasingly slower, approximately according to the adiabatic gradient of 0.3-0.4 K/km, which is also reflected into the viscosity profile. The viscosity decreases until 200 km and increases again below this depth. The largest lateral variations are seen between 150 and 200 km depth (up to 0.6 log units), which is inline with the largest temperature variations shown in Figure 2. Below 200 km depth, lateral viscosities decrease as temperatures converge. The grain size and water content shift the profile either to the left or right. An increasing grain size increases the viscosity, whereas larger water content has a weakening effect on the upper mantle.

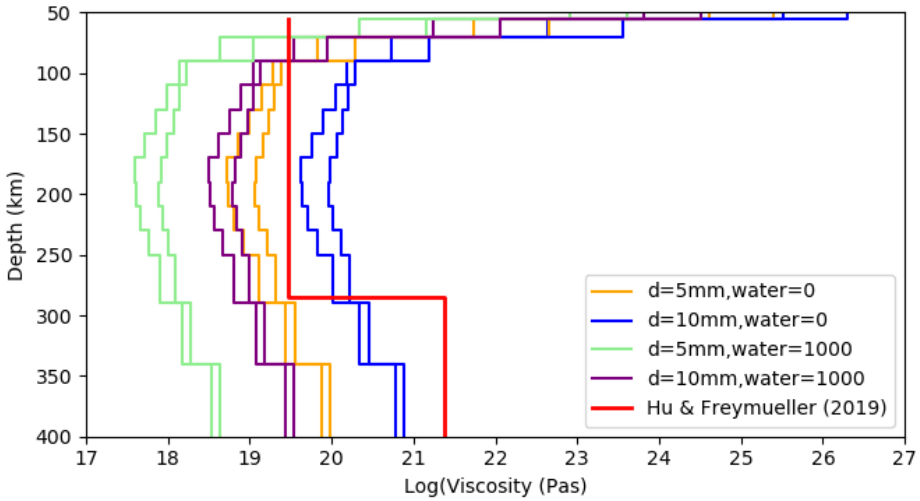

Figure 9: Viscosity profiles obtained with WINTERC-3D temperatures at select grain sizes and water content. The viscosity profiles are taken at two points, (1) 133.6°W, 57.3°N and (2) 138.8°W, 59.3°N.

Next, we analyze the viscosity profiles obtained with the second approach. Figure 10 shows the viscosity profiles derived directly from shear wave anomalies for a select number

of combinations between the background viscosity in the asthenosphere η_0 and the β parameters. The spread in viscosity is largest around 100 km, which is expected as the shear wave velocity anomalies are largest around this depth (Figure 4). Below 285 km, the lateral variation is relatively small as shear wave anomalies converge. In any case, lateral variation is expected to play a less important role at deeper depths as the GIA is insensitive to viscosities at deeper depths due to the short wavelength of the ice load. The shear wave anomalies in Southeast Alaska suggest a lower mantle viscosity. We find that, any profile where only β is increased, while the background viscosity is equal to that of Hu and Freymueller (2019), leads to lower viscosities and thus overestimate the uplift. To account for this effect, while also wanting to investigate the influence of lateral variations, the background viscosity in the asthenosphere is increased until a best-fit solution is found.

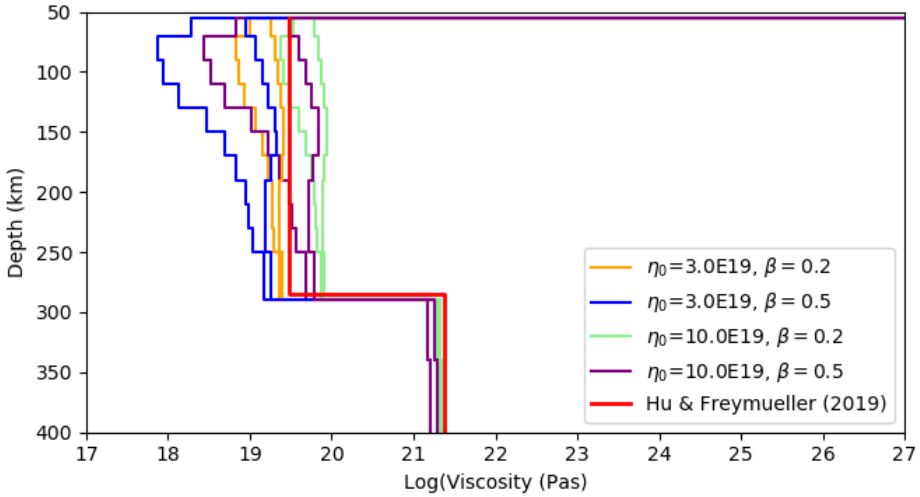

Figure 10: Viscosity profiles obtained directly from shear wave anomalies at select background viscosity and β. The viscosity profiles are taken at two points, (1) 133.6°W, 57.3°N and (2) 138.8°W, 59.3°N.

4.2 Effect of lateral variations on uplift

The resultant profiles in approach 2 are used to analyze the effect of lateral variations on uplift. Here we compare the uplift rate obtained for select profiles with $\eta_0 = 5.5 \times 10^{19}$ and varying β. Figure 11 shows the spatial distribution of change in uplift rate for (a) $\beta = 0.1$ and (b) $\beta = 0.2$ with respect to $\beta = 0$. As noted in section 4.1, an increasing β parameters has a weakening effect on the upper mantle, resulting in higher uplift rates. We can observe two peaks. The first peak is located to the eastern side of GB along the Chilkat and Chilkoot inlets. The second peak is located in the southeastern corner of our area of interest. Referring to Figure 4, we note that the lower seismic anomalies are seen in the

proximity of these two uplift peaks. For the first peak, relatively lower seismic anomalies are primarily seen in the upper 100 km. In a similar fashion, lower seismic velocities are extended and slowly decrease towards 200 km depth. There is a depth sensitivity of seismic wave anomalies which is also related to the induced ice load. For example, the first peak is in the proximity of the asynchronous ice load model for Glacier Bay, explained in Section 2.4. A decrease in viscosity for the first peak results in higher uplift than a the same decrease in viscosity for the second peak. Even though the first peak is attributed to somewhat larger viscosities than the second peak, we conclude that the sensitivity towards the ice load model with depth results in two uplift peaks with approximately the same magnitude. For GB uplift rates increase from $\sim$ 3.0 mm/yr for $\beta = 0.1$ to $\sim$ 6.0 mm/yr for $\beta = 0.2$. YK is affected with an increase of $\sim$ 1.2 mm/yr for $\beta = 0.1$ to $\sim$ 2.0 mm/yr for $\beta = 0.2$. For the larger ice loads, the increase from $\beta = 0.1$ to $\beta = 0.2$ is approximately twice as large. Once past the ice margin the differences quickly decrease towards zero (excluding the fore-bulges).

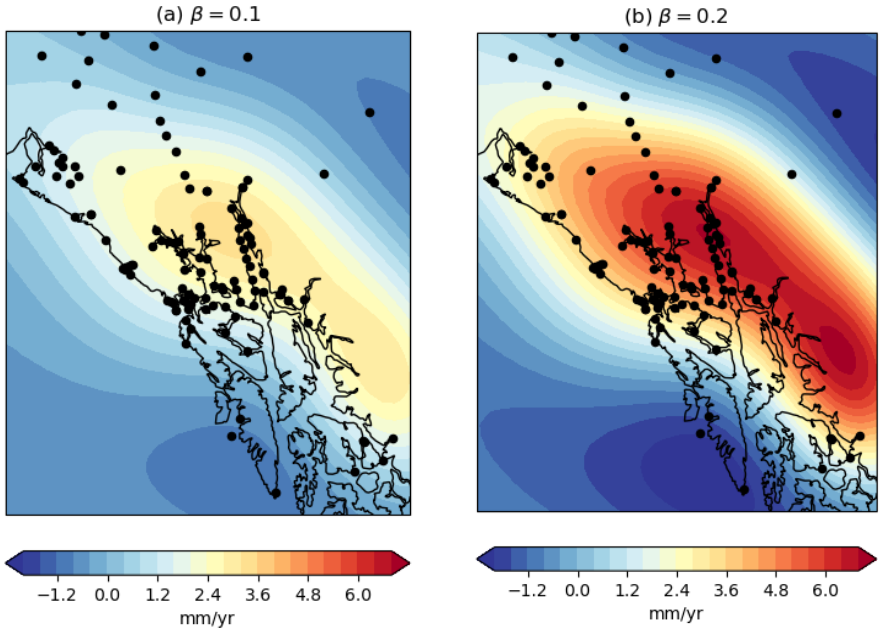

Figure 11: Difference maps with $\eta_0 = 5.5 \times 10^{19}$ Pa s. (a) difference between uplift rates produced with $\beta = 0$ and $\beta = 0.1$ and (b) difference between uplift rates produced with $\beta = 0$ and $\beta = 0.2$. Black dots indicate GPS locations.

4.3 Evaluation based on vertical GPS rates

The GIA model performance is tested against GPS rates from Hu and Freymueller (2019). The vertical uplift is a composite of post-LIA, PDIM, Pleistocene glaciations and tectonics effects. Tectonic effects are small and not taken into consideration and the effects of

the ice melt since the Last Glacial Maximum (LGM) taken from Hu and Freymueller (2019). The LGM effects include contributions of the Laurentide ice sheet (ICE-3G), glaciers in southern Alaska (Wheeler, 2013) and glaciations of southern British Columbia and Cascadia (James et al., 2009). The effects were estimated using the normal-mode GIA model by Hu and Freymueller (2019), which may not represent the effects with finite element with slightly different Earth parameters. The LGM effects are relatively small, hence the overall difference is assumed to be negligible. The misfits between the observed and predicted GIA rates are evaluated using the χ^2 test, which is computed using:

$$\chi^2 = \frac{1}{N} \sum_{i=1}^{N} \left(\frac{o_i - p_i}{\sigma_i} \right)^2, \tag{5}$$

where N is the number of observations, o_i is the observed GPS rate, p_i is the predicted uplift rate (incl. LGM, LIA and PDIM effects) and σ_i the GPS error. GPS observations are available for two periods: 1992-2003 and 2003-2012. Observations of both periods are combined to compute the best-fit value.

4.3.1 Misfit evaluation of approach 1 (flow laws)

We search for the optimal grain size and water content combination that best fits the GPS observations. The results of the search grid are seen in Figure 12a. Results including a grain size smaller than 5 mm are omitted as these lead to an upper mantle where viscosities are too low which fail to explain the GIA observables. There is a preference for lower grain sizes (1-4 mm) based on xenolith data, however, some samples of 10 mm have been found, as explained in Section 2.2. A dry setting with grain sizes 5-6 mm, lead to too much uplift as the grain size is too small. On the other hand, a dry setting with larger gran sizes ($>$ 7 mm) result in under prediction. The results indicate that a hydrated upper mantle is preferred. (Dixon et al., 2004) suggests a hydrated upper mantle is required for western United States (and thus the Cordillera) is required to explain such low viscosities. We do show that lower viscosities can be obtained with smaller grain sizes, however, we also show this leads to a worse fit. The combinations of grain size and water content used here lead to a better fit if a hydrated mantle is present.

A number of best-fit models were obtained with different combinations of grain size (d) and water content (fH_2O). Such combinations include (a) (d, fH_2O) = 8mm, 400 H/10^6 Si, (b) (d, fH_2O) = 9mm, 500 H/10^6 Si and (c) (d, fH_2O) = 10mm, 700 H/10^6 Si. The corresponding χ^2 values are 20.7, 20.9 and 20.6, respectively. The list could be extended by using larger grain sizes, but these are outside our search space. The reason that there are multiple combinations possible is due to the scaling nature of the grain size and water

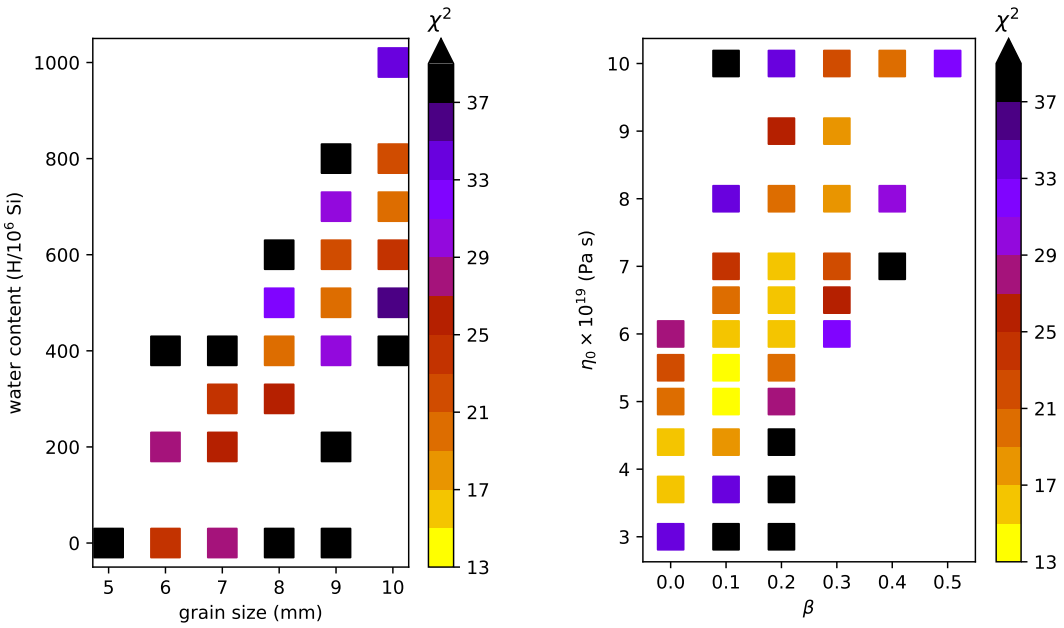

Figure 12: (a) Scatter plot of χ^2 values obtained with approach 1, where the viscosity distribution is computed through flow laws for olivine. (b) Scatter plot of χ^2 values obtained with approach 2, where the viscosity distribution is obtained directly from shear wave velocity anomalies.

content as only diffusion creep is considered. The combinations lead to very similar viscosity distribution and thus similar uplift patterns. Supplementary Figure S2 shows that models (b) and (c) cannot be distinguished by the GPS data within 2σ uncertainty. Models (a) and (b) differ most (1.0-1.7 mm/yr) around the two uplift peaks at GB and YK and farther away from the peaks no difference can be detected with GPS data within 2σ uncertainty. The residuals of model (a) are smaller than model (b) around the uplift peaks and the spread in residuals is smaller (Supplementary Figure S3). We select model (a) as the best-fit model obtained through flow laws for olivine. The residuals of this model are shown in Figure 13. The two uplift peaks at GB and YK are under predicted; residuals vary between 5-9 mm/yr. If the residuals are to be reduced at this two peak uplifts, the viscosity needs to be lowered. However, this causes the surrounding uplift rates to be overestimated, leading to a worse fit.

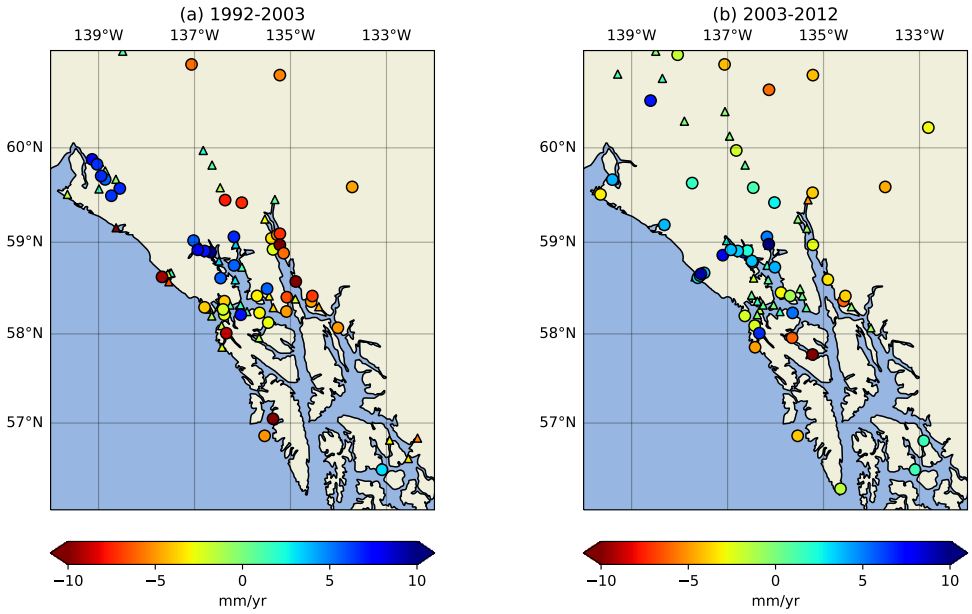

Figure 13: Residual maps of the best-fit model obtained through flow laws ($\chi^2 = 20.7$). Subfigures a and b correspond to the periods 1992-2003 and 2003-2012, respectively. Circles represent residuals resolved with the GPS uncertainty of 2σ and triangles indicate residuals that cannot be resolved.

4.3.2 Misfit evaluation of approach 2 (seismic anomalies)

Here, the search is done on the combination of the β parameter and the background viscosity η_0 in the asthenosphere that best fits the GPS data. Figure 12b shows the χ^2 values within the search space. Several observations can be made on Figure 12b. Firstly, lower β values are preferred, indicating that lateral variations should be small and that the thermal contribution to lateral variations is small. Secondly, higher background viscosities combined with a higher β parameter does not lead to a better fit. This shows that larger lateral variations together with a higher background viscosity cannot produce similar results as a profile where there is less lateral variation. Lastly, looking at the results for $\beta = 0$, a worse fit is obtained at the baseline setting, with respect to the incompressible case, where $\beta = 0$, $\eta_0 = 3.0 \times 10^{19}$ Pa s and $\chi^2 = 34.4$. This is to be expected as material compressibility is implemented. From Section 2 in the Supplementary Information it was concluded that material compressibility increases the uplift rate, thus we obtain a worse fit here as uplift rates are too high. When compressibility is considered, a higher mantle viscosity (with the same lithospheric thickness) is preferred. The results show a better fit for the 1D model with background viscosity of 3.7×10^{19}, which is an increase of 23% with respect the viscosity used for the 1D reference model, which is discussed later. The best-fit value for the latter model is 16.8, showing that compressibility can already lead to a better fit. Even so, the

best-fit 3D model has a best-fit value of 13.7, indicating that lateral variations improve the fit even further. The misfits of the best-fit 3D model and that of our 1D reference model are discussed in detail in Section 4.4.

The best-bit Earth model has a χ^2 value of 13.70 with $\eta = 5.0 \times 10^{19}$ Pas and $\beta = 0.1$. The second to best-fit is $\chi^2 = 13.75$ with $\eta = 5.5 \times 10^{19}$ Pas and $\beta = 0.1$. These two models are compared on a spatial level, shown in Supplementary Figure S4. We compare between the two periods 1992-2003 and 2003-2012. For the first period only a few GPS points can be resolved using GPS data, thus not much can be concluded from this period. However, it can be observed around YK that the model with $\eta_0 = 5.0 \times 10^{19}$ Pas is slightly performing better as residuals here are smaller (Supplementary Figure S5). The same holds the area in the vicinity of GB for the second period. Hence, a background viscosity of 5.0×10^{19} is preferred over a background viscosity of $5.5 \cdot 10^{19}$ Pas as the latter underestimates the two observed peaks at YK and GB to a larger extent. The differences in viscosity is relatively small (10%) and they reflect between 1 and 1.5 mm/yr difference in uplift around the observed peak uplifts which is slightly above the GPS uncertainty.

The residual map of the best-fit model obtained directly from shear wave anomalies is shown in Figures 16b and 17b. The uplift located at YK is underestimated by 7-8 mm/yr for select GPS points. The same holds for GB where uplift rates are underestimated between 2 and 6 mm/yr. This shows that the GIA model is performing worse where PDIM is larger. Therefore, ice thinning rates here may be underestimated. The residuals decrease land inwards, farther away from the ice load. For the first approach involving flow laws, the overall uplift was underestimated. This is likely due to inferred viscosity in the shallow upper mantle, however, ice thinning rates may similarly be underestimated around the two observed uplift peaks.

4.4 A 1D incompressible model versus a 3D compressible model

The misfits of the obtained best-fit 3D models, from approach 1 and 2, are compared with results from a 1D finite element reference model. The selected 1D reference model selected uses the same Earth layering as the 3D model as described in Table 1, however, the poisson's ratio is set to 0.4999. This models closely represents the best-fit normal-mode model by (Hu & Freymueller, 2019). The fit (χ^2) of our 1D reference model and that of the normal-mode model are 17.5 and 17.9, respectively. Note that these fit values were computed using a slightly older GPS dataset used in (Hu & Freymueller, 2019) (which mainly included larger GPS uncertainties). The χ^2 value for our 1D reference model, using the GPS dataset used in this article, is 16.8 and could not be computed for the normal-mode model as a select number of GPS points were missing. However, using the older GPS dataset, the two

best-fit models of approach 1 and 2 result in fit values of 22.1 and 14.6. respectively. The latter value is indeed lower than the best-fit 1D model, which shows that a 3D compressible model can provide improvements. In the next sections we will demonstrate in what ways the first approach fails to perform better than a 1D model and what kind of improvements are achieved with the second approach.

The statistics of the residuals of the 1D and the two best-fit 3D models obtained with approach 1 and 2, respectively, are shown in Figure 14. The 3D model obtained through flow laws ($\chi^2 = 20.7$) has a worse fit than the 1D model ($\chi^2 = 16.8$). This 3D model fails to explain the large observed uplift rates and the spread in residuals is the highest (4.39 mm/yr). From past GIA studies in this region it became apparent that with increasing PDIM, a thinner elastic lithosphere underlain with a slightly higher viscosity is required to explain the increasing rate in observed uplift. As explained in Section 3, the temperature profile by WINTERC-3D in this region follows a much thicker thermal lithosphere resulting in a larger elastic thickness, and ultimately a worse fit. In addition, following the 2002 Denali earthquake, Freed et al. (2006) showed that viscoelastic flow between 60 and 100 km with viscosity varying from 0.3×10^{19} to $> 10^{19}$ is required to explain the post-seismic deformation in the far-field. We conclude that in order to get a better fit for this particular 3D model, either (1) the ice thinning rates must be larger or (2) the thermal profile needs to be adjusted so that a thinner lithosphere is obtained. The former was already corrected for in Hu and Freymueller (2019) on a regional scale and showed that the best-fit model parameters had a low sensitivity towards errors in the recent ice load. However, uplift rates are also under predicted in this study for the area corresponding to the Yakutat Icefields, suggesting an even higher ice loss rate is required to explain the observed uplift rate for this particular area. Even so, we assume that the primary source, explaining the under prediction over the entire region, is related to the effective elastic thickness.

The second approach resulted in a better fit than the 1D reference model. From now on we refer to this model as the best-fit 3D model. Note that the 3D viscosity space of the best-fit 3D model beneath Southeast Alaska (Supplementary Figure S6) are within the same range found in 1D studies of this region (e.g., Larsen et al., 2005; Sato et al., 2011; Hu & Freymueller, 2019). Before we can compare the uplift results of the best-fit 3D model with the 1D reference model, we need to analyze the different parameters that were changed between these two models. These parameters include the compressibility, the background viscosity η_0, and the β parameter used to tune the lateral variations. Due to the linear rheology, these effects can easily be separated and analyzed individually. The steps taken to go from an incompressible 1D model to the compressible 3D model are:

554 1. incompressible 1D → compressible 1D;
555 2. compressible 1D → compressible 3D ($\eta_0 = 3.0 \times 10^{19}$ Pa s);
556 3. compressible 3D ($\eta_0 = 3.0 \times 10^{19}$ Pa s) → compressible 3D ($\eta_0 = 5.0 \times 10^{19}$ Pa s).

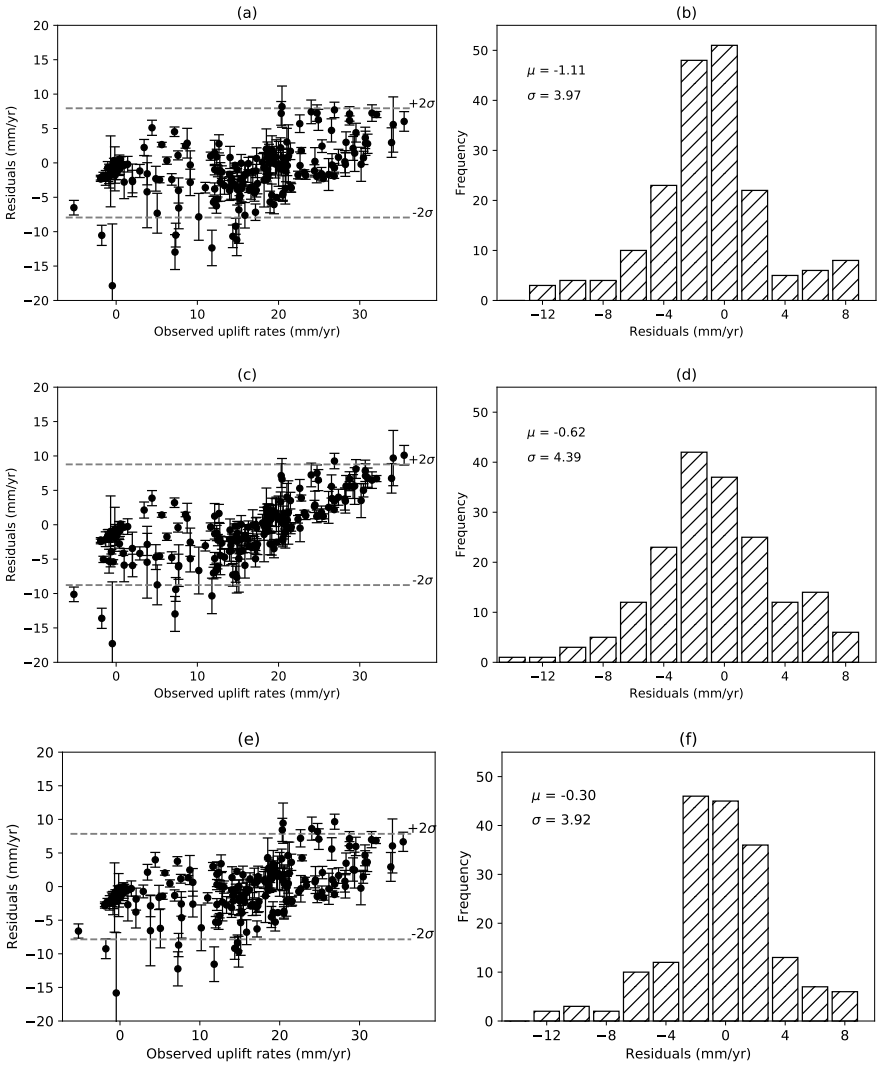

Figure 14: Residual histograms of the 1D and the two best-fit 3D models. Residuals cover the two periods 1992-2003 and 2003-2012. Fit values (χ^2) of the 1D, 3D (approach 1) and 3D (approach 2) models are 16.8, 20.7 and 13.7, respectively.

557 The differences in the resultant uplift rates between each of the steps described above
558 are shown in Figure 15. As shown in the Supplementary Information (Section 2) compress-
559 ibility has a non-uniform increasing effect on the uplift rate. When adding lateral variations
560 (Figure 15b) we observe again an increase in uplift rate (within the ice margin) where the
561 largest uplift occurs in the southeastern corner of the region of interest, which is attributed

to the relatively lower seismic anomalies here. By increasing the background viscosity (Figure 15c) a decrease in uplift is seen as the mantle strength is increased. The largest effects are seen around GB and YK. The first and second steps have a weakening effect on the mantle and the third step is required to increase the strength again to obtain a good fit, as shown in Figure 15d.

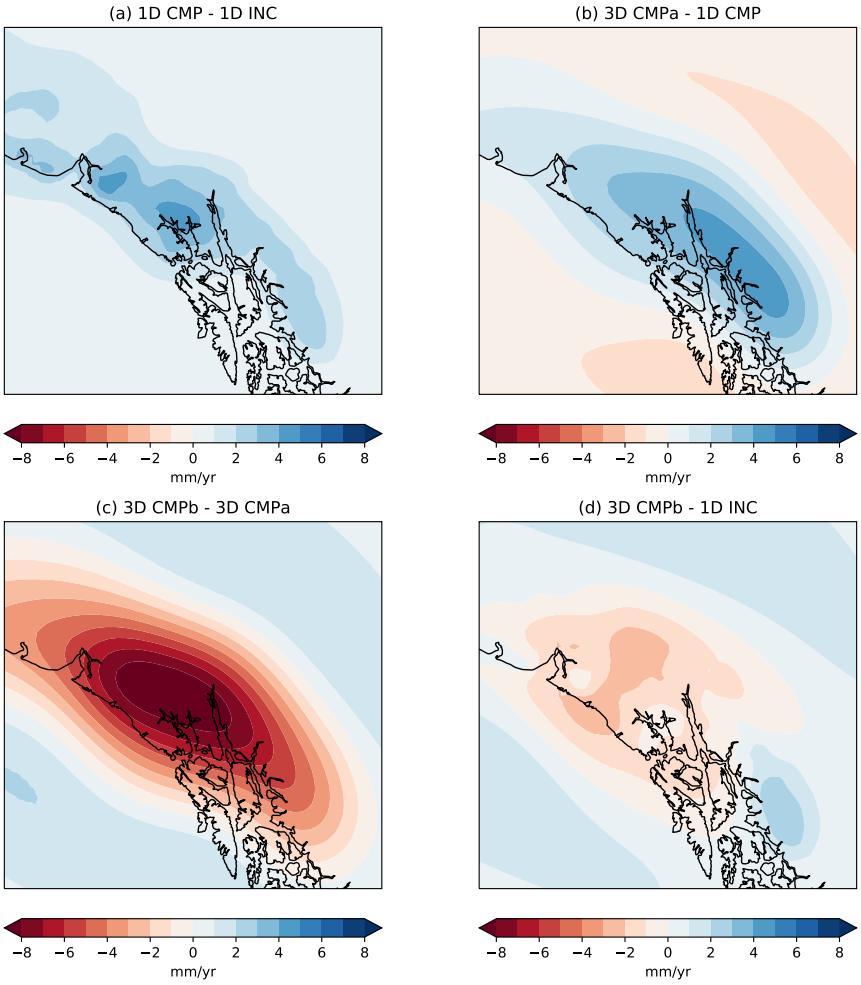

Figure 15: Compressibility, 3D and background viscosity effects (period = 2003-2012). (a) depicts the compressibility effects of the 1D model, (b) shows the effects of adding lateral variations (β=0.1), (c) shows the effect of changing the background viscosity in the asthenosphere from 3.0×10^{19} Pa s (3D CMPa) to 5.0×10^{19} (3D CMPb) and (d) depicts to overall change from an incompressible 1D model to a compressible 3D model. Note the different scales used.

We first compare the best-fit 3D model with the reference 1D model by looking at the difference in prediction rates over Southeast Alaska shown in Figure 15d. Later on we will draw conclusions with GPS data. The uplift rates at the two peaks seen in YK and GB are very similar. The largest differences (±2.7 mm/yr) occur in the south of the region of

interest (57.5°N, 132°W) and the area north of GB (60°N, 137°W). The south is attributed to the relatively low shear wave anomalies, resulting in lower viscosities and thus higher uplift. Less uplift is seen towards the North, which is opposed to the conclusions in Section 4.2, where uplift rates should increase as a result of lateral variations. This is attributed to the strengthening effects of increasing the background viscosity, as shown in Figure 15c. A similar effect is seen along the coast.

Secondly, we evaluate the spatial performance of the 1D and 3D models with GPS measurements for two periods, 1992-2003 and 2003-2012. We analyze both periods individually so that we can investigate the systemic errors in each of these time frames. The spatial residuals of our 1D reference model and the best-fit 3D model for first period, 1992-2003, are depicted in Figures 16a&b. Figure 16c shows the difference in the (absolute) residuals for the first observation period. A negative number indicates a decrease in the residual for the 3D model, i.e. a better prediction, whereas a positive number shows a worse fit. We only draw conclusions where the difference in the absolute residual is larger than the measurement uncertainty (indicated with circles). Hu and Freymueller (2019) identified a number of systematic residuals in their normal-mode model which also hold for our 1D reference model. These include (1) under prediction at the Yakutat Icefields, (2) over prediction from Haines to Juneau (135°W and 58°N-59°N) and (3) a good fit north of 135°W. Similarly, these systematic residuals can be identified for the 3D model. The differences between the two models for this model cannot be differentiated within 2σ uncertainty (except at 1 GPS point). We can see a slight improvement from Haines to Juneau, however, the 3D model still over predicts here. Also for the Yakutat area we cannot see an improvement or deterioration within a 2σ uncertainty. The latter also holds for points located around GB for this period. Recall that the 1D *finite element* model is used here as reference. From the benchmark analysis (the reader is referred to Section 1 in the Supplementary Information) the FE model produced less uplift around YK (1-2.5 mm/yr) where PDIM effects are largest, which is also attributed to smoothing if the ice load. This shows that the 3D model cannot solve the underestimated uplift in YK without changing the ice load model.

The spatial residuals for the second period can be seen in Figure 16. Similarly to the first period, the band along Haines to Juneau is over predicted by both the 1D and 3D models, however, the 3D model does perform better here which is also detectable by the GPS network within 2σ uncertainty. To the north we observe that the 3D model under predicts, whereas the 1D model over predicts. Along the coast (i.e. Alsek River and Letuya Bay) a better fit is obtained for the first period and a worse fit for the second period. This shows that the 3D GIA cannot keep up with the increase in uplift rate seen at these locations for the second period. Overall, the mean of the residuals, the spread and χ^2 are reduced

for the 3D model over the period 1992-2003, as shown in the histograms in Figure 18. For the second period, similar conclusions can be made. Regardless of the systematic errors associated to the ice load model, the 3D model shows smaller residuals for both periods and thus we conclude that 3D variations results in a slight improvement. The improvements are small (1-2.7 mm/yr) but can be seen by the GPS network and are thus relevant. The improvements outweigh the points with worse misfits leading to a better fit than the 1D model.

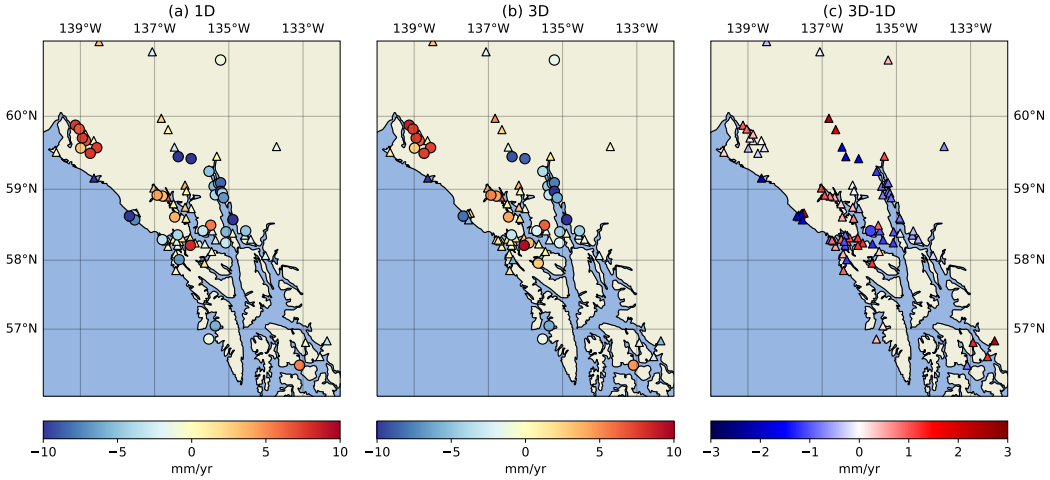

Figure 16: Spatial map of residuals of the 1D benchmark model and the best-fit model where $\chi^2 = 13.7$ for the period **1992-2003**. Circles represent differences detected by the GPS network within 2σ uncertainty, whereas triangles represent differences that cannot be detected.

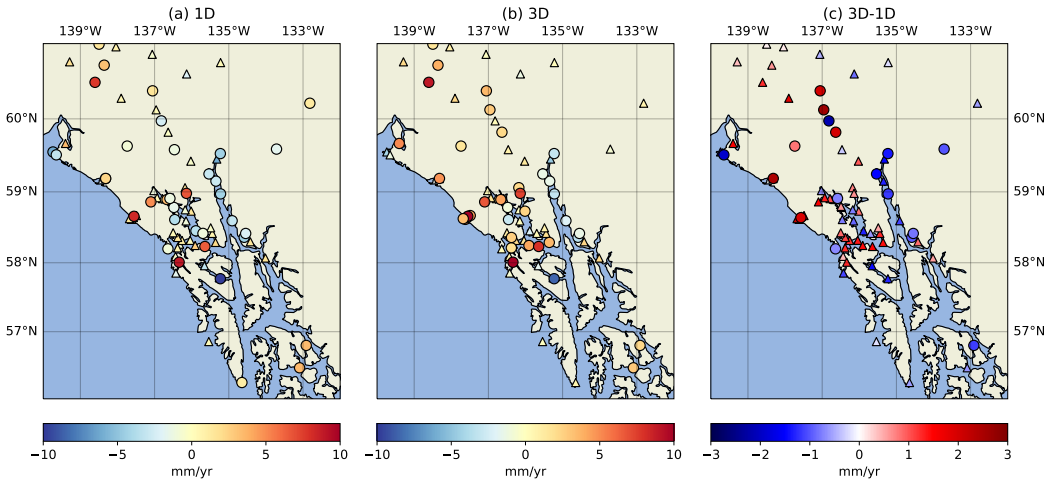

Figure 17: Spatial map of residuals of the 1D benchmark model and the best-fit model where $\chi^2 = 13.7$ for the period **2003-2012**. Circles represent differences detected by the GPS network within 2σ uncertainty, whereas triangles represent differences that cannot be detected.

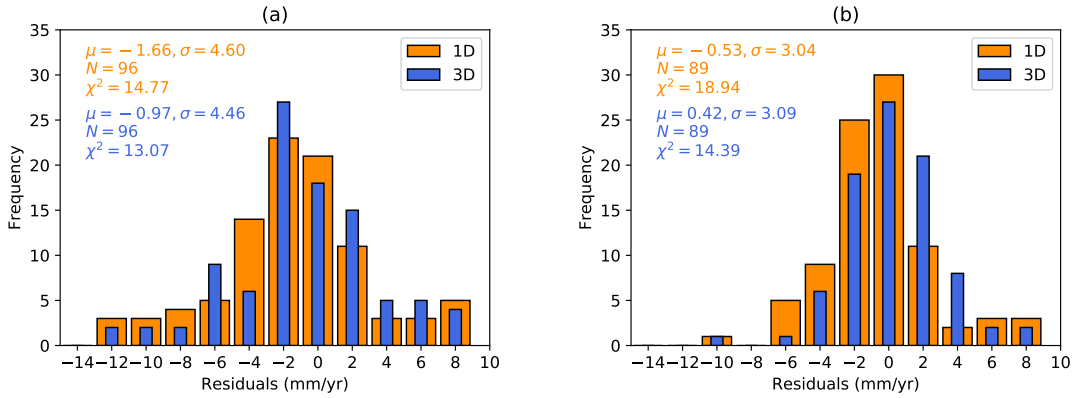

Figure 18: Residual histograms of the 1D and best-fit 3D model for the periods 1992-2003 and 2003-2012.

4.5 Model limitations

There are a number of limitations to the GIA model that are briefly discussed. First of all, the uncertainties regarding the ice load model, both spatially and in time, influence the earth model parameters. These uncertainties are related to both historic and PDIM load changes. The PDIM rates (1992-2012) were constrained by means of comparing GIA predictions with GPS observations in Hu and Freymueller (2019). Scaling of the ice thinning rates may not be uniform with Southeast Alaska and select areas may have an asynchronous ice load history with respect to the regional ice load model (such as YK and GB). The ice loading history was optimized for Southeast Alaska and this may not hold for all of Alaska. Moreover, the spatial loading history by (Berthier et al., 2010) may be subjected to uncertainties and biases related to the ice mass balance. Secondly, uncertainties in the creep flow parameters also reflect on uncertainties in the derived earth rheology parameters. Grain size and water content can vary with depth, and may play a more important role locally. Sensitivities to the scaling relationship were yet to be tested. Uncertainties in $[\partial \ln \nu_S / \partial T]_{tot}$ are between 10% and 20% (Karato, 2008) which also reflect the uncertainties in the β parameter. Thirdly, in this paper only diffusion creep was modelled. A number of GIA studies have shown that a power-law rheology or composite rheology improved the overall fit to GIA observables (e.g. van der Wal et al., 2010; van der Wal et al., 2013). However, this should be handled with care here, as composite and power-law rheologies have led to lower present-day uplift rates than linear rheologies, where past glaciations were modelled. A non-linear rheology results in higher relaxation times and thus lower present-day uplift rates. Here we also model PDIM and thus with faster relaxation times an increase in uplift can be expected. However, one should also keep in mind that from past glaciations,

a decrease in present-day uplift is expected. How much each component contributes to the total uplift is currently unknown. Background stresses could be significant here and affect GIA. Moreover, other creep mechanisms are at play, such as grain boundary sliding and transient creep. The latter could play an important role considering the timescales of the ice history. Transient creep has been shown to play a significant role in post-seismic studies in Alaska on monthly to decadal timescales (Freed et al., 2012). It is, however, unknown how this plays out with past and current ice load changes.

5 Conclusions

A 3D GIA has yet to be made for (Southeast) Alaska and we demonstrate first order estimates of the effects of lateral variations on the GIA uplift. Two approaches were used to infer lateral variations in the upper mantle rheology, which use seismological, petrological and thermochemical datasets. The second approach, which converts shear wave anomalies to viscosity using scaling laws, was superior to the first approach, which used a 3D temperature model and flow laws for olivine to obtain the viscosity.

Approach 1 uses a 3D temperature distribution to infer lateral variations in the upper mantle. The viscosity structure is derived using a linear rheology for olivine with use of experimental flow laws for olivine (Hirth & Kohlstedt, 2003) in the upper 400 km. We vary water content and grain size to find a viscosity distribution that best fits the GPS data. A best-fit model is found with 8 mm grain size with a wet rheology (400 ppm). A dry rheology leads to underestimation of the uplift rates for grain sizes larger than 5 mm, whereas severe overestimation is seen for smaller grain sizes. The obtained parameters are in agreement with xenolith data, which show grain sizes varying between 1 and 10 mm (e.g., Himmelberg et al., 1986; Himmelberg & Loney, 1986; Morales & Tommasi, 2011). However, this best-fit model does not perform better than a radially symmetric (1D) Earth with rheology parameters taken from Hu and Freymueller (2019). Our model underestimates the two peaks in uplift rate at the Yakutat Icefields and Glacier Bay worse than the 1D model. The temperature profile is not in agreement with findings from Hyndman et al. (2009) beneath 60 km depth. Hyndman et al. (2009) show a change in temperature gradient starting around 60 km, which follows the adiabatic gradient, whereas the adiabatic gradient in this study starts at approximately 100 km. In addition, lower temperatures by Hyndman et al. (2009) are likely to be attributed to the strong anelastic corrections. A thicker thermal lithosphere results in larger viscosities at depths shallower than 60 km. As a result, the effective elastic thickness is larger than that of the 1D model. Moreover, Freed et al. (2006) also support viscoelastic flow beneath 60 km depth to explain post-seismic deformation. Past GIA studies focused on this region showed that a thinner lithospheric thickness underlain with a higher

mantle viscosity is required to explain the increasing uplift rate. We thus conclude that the effective elastic thickness is the main reason that uplift rates are under predicted.

In approach 2 we use shear wave velocity anomalies to infer lateral variations in the viscosity structure of the upper mantle. Using the approach by Wu et al. (2013), seismic anomalies are translated into viscosity anomalies using scaling relationships, where it is assumed that temperature anomalies are partly responsible for the seismic anomalies. The β parameter is introduced to constrain the thermal contribution to lateral variations. A β parameter of 0 indicates no lateral variation, whereas a value of 1 indicates that only thermal effects contribute to lateral variations. In addition, we vary the background viscosity in the shallow upper mantle. Due to compressibility, a higher background viscosity in the asthenosphere is preferred when no lateral variations are incorporated. It was shown that a compressible 1D model with higher asthenospheric viscosity gives a better fit than an incompressible 1D model with a lower asthenospheric viscosity. Moreover, a higher background viscosity is required in the 3D model to counteract the weakening effect of the shear wave anomalies, as shear wave anomalies in this region are negative. The best-fit model was obtained with parameters $\beta = 0.1$ and $\eta_0 = 5.0 \times 10^{19}$ Pa s. This shows that improvements can be achieved with small lateral variations (up to 0.4 log units, or equivalently, a factor of 2.5) where the thermal contribution to shear wave anomalies is low (10%). Considering the extent of this study region, large viscosity variations are not likely and our results from approach 1 also indicate small variations up to 0.6 log units, or equivalently, a factor of 4.0. This also explains why a low β value is required, as larger β values result in too much lateral variation and in turn a worse fit.

Wu et al. (2013) showed that the thermal effect is contributing to approximately 65% to the lateral heterogeneity in the upper mantle under Laurentia and Fennoscandia. The contribution became higher in the deeper mantle. For Southeast Alaska we are limited to the upper mantle as the GIA process here is less sensitive to viscosity variations deeper within the Earth due to the short wavelength of the ice load. The low β value for Southeast Alaska suggests that non-thermal effects, such as composition, play an important role in lateral variations in viscosity within the shallow upper mantle. Moreover, in Wu et al. (2013) it was assumed that effects of water content and partial melting were negligible as no subduction zone was in the proximity. In this study we show that a hydrated mantle is preferred, however, this can also influence the seismic velocities. We note that the southeastern corner of our region of interests is characterized by low seismic waves, this can be attributed to higher water content and/or partial melt. On the other hand, this can also be attributed to uncertainties in the ice load model. For example, ice loss rates can be asynchronous with respect to the regional ice load model here, such that there is more or less ice loss in select

areas at certain times. Moreover, the sensitivity of seismic anomalies to thermal effects can vary in location.

We have shown that the inclusion of both compressibility and 3D effects improve the fit. The viscosity values ($2 - 5 \times 10^{19}$ Pa s) within the shallow upper mantle beneath Southeast Alaska of the best-fit 3D model, obtained with approach 2, are within the same range found in 1D studies of this region (e.g. Larsen et al., 2005; Sato et al., 2011; Hu & Freymueller, 2019). The best-fit 3D model does not solve the underestimation problem at the two observed uplift peaks, as similar rates of the two uplift peaks are seen in both the 1D and 3D models. Most of the improvements occur in the vicinity of Glacier Bay. The overall improvements caused the mean of the residuals to shift from -1.1 mm/yr (1D) to -0.3 mm/yr (3D), and slightly reduced the spread in residuals. We showed that a homogeneous compressible model could not produce better results than a heterogeneous model. We thus conclude that lateral variations improve the fit even further. Overall, improvements between 1.0 and 2.7 mm/yr are seen, which are slightly above the GPS uncertainty.

References

Amelung, F., & Wolf, D. (1994). Viscoelastic perturbations of the earth: significance of the incremental gravitational force in models of glacial isostasy. *Geophysical Journal International*, *117*(3), 864-879. Retrieved from `https://doi.org/10.1111/j.1365-246X.1994.tb02476.x` doi: 10.1111/j.1365-246X.1994.tb02476.x

Barnhoorn, A., van der Wal, W., & Drury, M. R. (2011). Upper mantle viscosity and lithospheric thickness under iceland. *Journal of Geodynamics*, *52*(3), 260 - 270. Retrieved from `http://www.sciencedirect.com/science/article/pii/S0264370711000287` doi: https://doi.org/10.1016/j.jog.2011.01.002

Behn, M. D., Hirth, G., & Elsenbeck, J. R. (2009). Implications of grain size evolution on the seismic structure of the oceanic upper mantle. *Earth and Planetary Science Letters*, *282*(1), 178 - 189. Retrieved from `http://www.sciencedirect.com/science/article/pii/S0012821X09001575` doi: https://doi.org/10.1016/j.epsl.2009.03.014

Bell, D. R., Rossman, G. R., Maldener, J., Endisch, D., & Rauch, F. (2003). Hydroxide in olivine: A quantitative determination of the absolute amount and calibration of the ir spectrum. *Journal of Geophysical Research: Solid Earth*, *108*(B2). Retrieved from `https://agupubs.onlinelibrary.wiley.com/doi/abs/10.1029/2001JB000679` doi: 10.1029/2001JB000679

Berthier, E., Schiefer, E., Clarke, G., Menounos, B., & Remy, F. (2010). Contribution of alaskan glaciers to sea-level rise derived from satellite imagery. *Nature Geoscience*, *3*, 92-95. doi: 10.1038/ngeo737

Dixon, J. E., Dixon, T., Bell, D., & Malservisi, R. (2004). Lateral variation in upper mantle viscosity: role of water. *Earth and Planetary Science Letters*, *222*(2), 451 - 467. Retrieved from http://www.sciencedirect.com/science/article/pii/S0012821X04002055 doi: https://doi.org/10.1016/j.epsl.2004.03.022

Durkin, W., Kachuck, S., & Pritchard, M. (2019). The importance of the inelastic and elastic structures of the crust in constraining glacial density, mass change, and isostatic adjustment from geodetic observations in southeast alaska. *Journal of Geophysical Research: Solid Earth*, *124*, 1106-1119.

Dziewonski, A. M., & Anderson, D. L. (1981). Preliminary reference earth model. *Physics of the Earth and Planetary Interiors*, *25*(4), 297 - 356. Retrieved from http://www.sciencedirect.com/science/article/pii/0031920181900467 doi: https://doi.org/10.1016/0031-9201(81)90046-7

Elliott, J. L., Larsen, C. F., Freymueller, J. T., & Motyka, R. J. (2010). Tectonic block motion and glacial isostatic adjustment in southeast alaska and adjacent canada constrained by gps measurements. *Journal of Geophysical Research: Solid Earth*, *115*(B9). Retrieved from https://agupubs.onlinelibrary.wiley.com/doi/abs/10.1029/2009JB007139 doi: 10.1029/2009JB007139

Freed, A., Burgmann, R., Calais, E., Freymueller, J., & Hreinsdottir, S. (2006). Implications of deformation following the 2002 denali, alaska, earthquake for postseismic relaxation processes and lithospheric rheology. *J. Geophys. Res*, *111*. doi: 10.1029/2005JB003894

Freed, A., Hirth, G., & Behn, M. (2012). Using short-term postseismic displacements to infer the ambient deformation conditions of the upper mantle. *Journal of Geophysical Research: Solid Earth*, *117*(B1). Retrieved from https://agupubs.onlinelibrary.wiley.com/doi/abs/10.1029/2011JB008562 doi: 10.1029/2011JB008562

Fullea, J., Lebedev, S., Martinec, Z., & Celli, N. (2019). Winterc: a new global thermochemical model of the uppermost mantle constrained by surface waves, heat flow, surface elevation and gravity satellite data. *Living Planet Symposium*.

Goes, S., & Govers, R. (2000). Shallow mantle temperatures under europe from p and s wave tomography. *Journal of Geophyscial Research*, *105*, 153-169.

Hibbitt, D., Karlsson, B., & Sorensen, P. (2016). *Getting started with abaqus, version (6.14).* (Hibbit, Karlsson & Sorensen, Inc.)

Himmelberg, G., & Loney, R. (1986). Characteristics and petrogenesis of alaskan-type ultramafic-mafic intrusions. *U.S. Geological Survey professional paper*, *1564*.

Himmelberg, G., Loney, R., & Craig, J. (1986). Petrogenesis of the ultramafic complex at the blashke islands, southeastern alaska. *U.S. Geological Survey Bulletin*, *1662*.

Hirth, G., & Kohlstedt. (2003). Rheology of the upper mantle and the mantle wedge: A

view from the experimentalists. In *Inside the subduction factory, 2004* (pp. 83–105). Blackwell Publishing Ltd. doi: 10.1029/138GM06

Hu, Y., & Freymueller, J. T. (2019). Geodetic observations of time-variable glacial isostatic adjustment in southeast alaska and its implications for earth rheology. *Journal of Geophysical Research: Solid Earth*, *124*(9), 9870-9889. Retrieved from `https://agupubs.onlinelibrary.wiley.com/doi/abs/10.1029/2018JB017028` doi: 10.1029/2018JB017028

Hyndman, R. (2017). Lower crustal flow and detachment in the north american cordillera: a consequence of cordillera-wide high temperatures. *Geophys.J. Internat.*.

Hyndman, R., Currie, C., Mazzotti, S., & Frederiksen, A. (2009). Temperature control of continental lithosphere elastic thickness, te vs vs. *Earth and Planetary Science Letters*, *277*, 539-548.

Ivins, E., & Sammis, E. (1995). On lateral viscosity contrast in the mantle and the rheology of low-frequency geodynamics. *Geophysical Journal Interna- tiona*, *123(2)*, 305-322.

James, T., Gowan, E., Wada, I., & Wang, K. (2009). Viscosity of the asthenosphere from glacial isostatic adjustment and subduction dynamics at the northern cascadia subduction zone, british columbia, canada. *Journal of Geophysical Research*, *114*, B04405. Retrieved from `https://doi.org/10.1029/2008JB006077`

Karato, S. (1993). Importance of anelasticity in the interpretation of seismic tomography. *Geophysical Research Letters*, *20*(15), 1623-1626.

Karato, S. (2008). *Deformation of earth materials: An introduction to the rheology of solid earth*. Cambridge University Press. doi: 10.1017/CBO9780511804892

Karato, S., & Karki, B. (2001). Origin of lateral variation of seismic wave velocities and density in the deep mantle. *Journal of Geophysical Research*, *106*(B10), 771-783.

Larsen, C. F., Motyka, R. J., Freymueller, J. T., Echelmeyer, K. A., & Ivins, E. R. (2005). Rapid viscoelastic uplift in southeast alaska caused by post-little ice age glacial retreat. *Earth and Planetary Science Letters*, *237*(3), 548 - 560. Retrieved from `http://www.sciencedirect.com/science/article/pii/S0012821X05004152` doi: https://doi.org/10.1016/j.epsl.2005.06.032

Morales, L. F. G., & Tommasi, A. (2011). Composition, textures, seismic and thermal anisotropies of xenoliths from a thin and hot lithospheric mantle (summit lake, southern canadian cordillera). *Tectonophysics*, *507*(1), 1 - 15. Retrieved from `http://www.sciencedirect.com/science/article/pii/S0040195111001776` doi: https://doi.org/10.1016/j.tecto.2011.04.014

Nield, G., Whitehouse, P., van der Wal, W., Blank, B., O'Donnell, J., & Stuart, G. (2018). The impact of lateral variations in lithospheric thickness on glacial isostatic adjustment in west antarctica. *Geophysical Journal International*, *214*, 811-824. Retrieved from

https://doi.org/10.1093/gji/ggy158

Pasyanos, M. E., Masters, T. G., Laske, G., & Ma, Z. (2014). Litho1.0: An updated crust and lithospheric model of the earth. *Journal of Geophysical Research: Solid Earth*, *119*(3), 2153-2173. Retrieved from https://agupubs.onlinelibrary.wiley.com/doi/abs/10.1002/2013JB010626 doi: 10.1002/2013JB010626

Peltier, W. R., Argus, D. F., & Drummond, R. (2015). Space geodesy constrains ice age terminal deglaciation: The global ice-6g (vm5a) model. *Journal of Geophysical Research: Solid Earth*, *120*(1), 450-487. doi: 10.1002/2014JB011176

Sato, T., Larsen, C. F., Miura, S., Ohta, Y., Fujimoto, H., Sun, W., ... Freymueller, J. (2011). Reevaluation of the viscoelastic and elastic responses to the past and present-day ice changes in southeast alaska. *Tectonophysics*, *511*, 79-88.

Sauber, J., & Molnia, B. (2004). Glacier ice mass fluctuations and fault instability in tectonically active southern alaska. *Global and Planetary Change*, *42*, 279-293. doi: 10.1016/j.gloplacha.2003.11.012

Schaeffer, A., & Lebedev, S. (2013). Global shear speed structure of the upper mantle and transition zone. *Geophys. J. Int.*, *194 (1)*, 417-449. doi: doi:10.1093/gji/ggt095

Schmidt, P. (2012). *Glacial isostatic adjustment : Inferences on properties and processes in the upper mantle from 3d dynamical modeling* (Unpublished doctoral dissertation). Uppsala University, Geophysics.

Schotman, H., Vermeersen, L., Wu, P., Drury, M., & De Bresser, J. (2009). Constraints on shallow low-viscosity zones in Northern Europe from future GOCE gravity data. *Geophysical Journal International*, *178*(1), 65-84. Retrieved from https://doi.org/10.1111/j.1365-246X.2009.04160.x doi: 10.1111/j.1365-246X.2009.04160.x

Schotman, H., Wu, P., & Vermeersen, L. (2008). Regional perturbations in a global background model of glacial isostasy. *Physics of the Earth and Planetary Interiors*, *171*(1), 323 - 335. Retrieved from http://www.sciencedirect.com/science/article/pii/S003192010800037X (Recent Advances in Computational Geodynamics: Theory, Numerics and Applications) doi: https://doi.org/10.1016/j.pepi.2008.02.010

Spada, G. (2003). *The theory behin taboo.* Samizdat Press, Golden-White River Junction.

Spada, G., Antonioli, A., Boschi, L., Brandi, V., Cianetti, S., Galvani, G., ... P., S. (2003). *Taboo, user guide.* Samizdat Press, Golden-White River Junction.

Spada, G., Barletta, V. R., Klemann, V., Riva, R. E. M., Martinec, Z., Gasperini, P., ... King, M. A. (2011). A benchmark study for glacial isostatic adjustment codes. *Geophysical Journal International*, *185*(1), 106-132. Retrieved from https://doi.org/10.1111/j.1365-246X.2011.04952.x doi: 10.1111/j.1365-246X.2011.04952.x

Stacey, F., & Davis, P. (2008). *Physics of the earth* (4th ed.). Cambridge University Press.

Turcotte, D., & Schubert, G. (2002). *Geodynamics.* Trumpington Street, Cambridge:

Cambridge University Press.

van der Wal, W., Wu, P., Wang, H., & Sideris, M. G. (2010). Sea levels and uplift rate from composite rheology in glacial isostatic adjustment modeling. *Journal of Geodynamics*, *50*(1), 38 - 48. Retrieved from `http://www.sciencedirect.com/science/article/pii/S0264370710000190` doi: https://doi.org/10.1016/j.jog.2010.01.006

van der Lee, S., & Frederiksen, A. (2005). Surface wave tomography applied to the north american upper mantle. *Geophysical Monograph Series*, *157*, 67-80.

van der Wal, W., Barnhoorn, A., Stocchi, P., Gradmann, S., Wu, P., Drury, M., & Vermeersen, B. (2013). Glacial isostatic adjustment model with composite 3-d earth rheology for fennoscandia. *Geophysical Journal International*, *194*. doi: 10.1093/gji/ggt099

Wheeler, L. (2013). *Modeling the influence of the last glacial maximum ice load on the tectonics of southeast alaska and the south island, new zealand* (Master's thesis). Retrieved from `https://digitalcommons.library.umaine.edu/etd/2043/` (University of Maine, Electronic Theses and Dissertions. 2043)

Whitehouse, P. (2018). Glacial isostatic adjustment modelling: historical perspectives, recent advances, and future directions. *Earth Surface Dynamics*, *6*, 401-429. Retrieved from `https://doi.org/10.5194/esurf-6-401-2018`

Wouters, B., Gardner, A. S., & Moholdt, G. (2019). Global glacier mass loss during the grace satellite mission (2002-2016). *Frontiers in Earth Science*, *7*, 96. Retrieved from `https://www.frontiersin.org/article/10.3389/feart.2019.00096` doi: 10.3389/feart.2019.00096

Wu, P. (2004). Using commercial finite element packages for the study of earth deformations, sea levels and the state of stress. *Geophysical Journal International*, *158*(2), 401-408. Retrieved from `https://doi.org/10.1111/j.1365-246X.2004.02338.x` doi: 10.1111/j.1365-246X.2004.02338.x

Wu, P., & Johnston, P. (1998). Validity of using flat-earth finite element models in the study of postglacial rebound. In (p. 191-202).

Wu, P., Wang, H., & Steffen, H. (2013). The role of thermal effect on mantle seismic anomalies under Laurentia and Fennoscandia from observations of Glacial Isostatic Adjustment . *Geophysical Journal International*, *192*(1), 7-17. Retrieved from `https://doi.org/10.1093/gji/ggs009` doi: 10.1093/gji/ggs009

3

Supplementary information

Supplementary information for

A 3-D Glacial Isostatic Adjustment model for post-Little Ice Age effects in Alaska

C.P. Marsman[1,2], et al.

[1] *Faculty of Civil Engineering and Geosciences, Delft University of Technology, Delft, The Netherlands*

[2] *Faculty of Aerospace Engineering, Delft University of Technology, Delft, The Netherlands*

Contents of this file

1 Benchmark for a 3D GIA model in SE-Alaska

The validity of the finite element code is checked with the output obtained by a normal-mode model in Hu & Freymueller (2019). The benchmark model consists of 5 unique material layers, which are defined in Table S1.

Table S1: Material properties of the incompressible 5-layered Earth model

Top of layer radius (km)	Layer thickness (km)	Density (kg/m^3)	Young's modulus (GPa)	Poisson's ratio (-)	Viscosity (Pa s)	Gravity (m/s^2)
6371	55	3028.4	157.6	0.4999	-	9.761
6316	230	3397.8	209.0	0.4999	$3.00 \cdot 10^{19}$	9.794
6086	385	3729.3	288.9	0.4999	$2.40 \cdot 10^{21}$	9.873
5701	2221	4877.9	658.4	0.4999	$5.01 \cdot 10^{21}$	9.963
3480	3480	10931.7	-	-	-	10.629

The number of finite elements required per Earth layer was investigated in order to minimize the bending errors associated with a finite element model. The first test included two finite element layers per Earth layer. The calibration test showed this setup resulted in lower uplift rates, indicating that the FE model does not bend enough. The second test included a total of 26 finite element layers, where the layer thickness increases with increasing depth, as shown in Table S2.

Table S2: Finite element layers definition. *FE layer thicknesses given from top to bottom layer.

Earth layer top radius (km)	Thickness (km)	Number of FE layers	FE layer thicknesses* (km)
6371	55	4	12, 14, 14, 15
6316	230	11	15, 9 × 20, 35
6086	385	4	55, 60, 135, 135
5701	2221	6	2 × 250, 3 × 430, 431
3480	3480	1	3480

Next to the vertical layering, the horizontal resolution was adjusted. The ice model is made of disks of approximately 22 km diameter. The normal-mode model in Hu & Freymueller (2019) uses spherical harmonics with maximum order and degree 2048 (∼10 km resolution). Tests were performed using a 10 and 15 km resolution. The 10 km resolution test did not yield significantly better results than the 15 km resolution test (differences less than 0.5 mm/yr) and resulted in much longer computational times. For that reason, the 15 km resolution was used in further simulations.

1.1 Uplift rate

The uplift rates (averaged between 2003 and 2012) for all of Alaska for both the normal-mode (NM) and finite element (FE) models can be seen in Figure S1. The uplift patterns obtained by both models are remarkably similar. Next, we will study the differences in Southeast Alaska interpolated at the GPS stations.

The interpolated differences at the GPS locations between the uplift rates of the two models

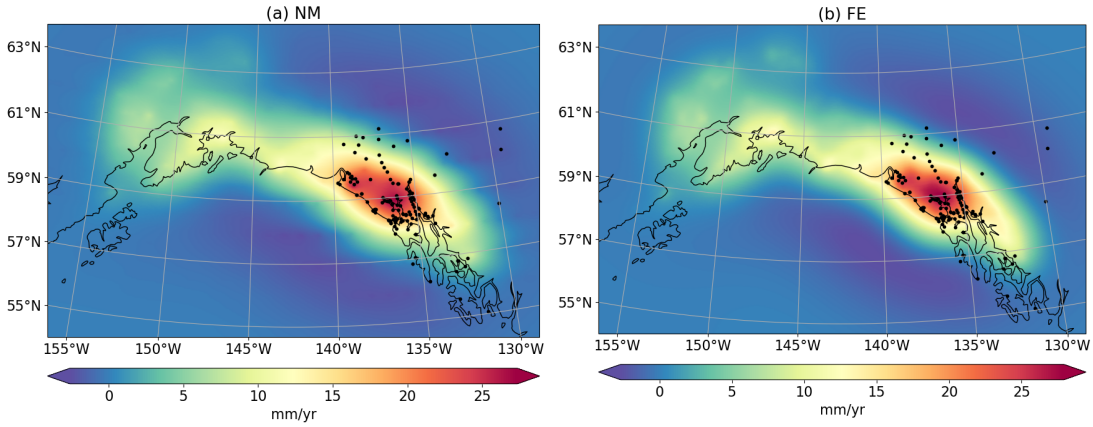

Figure S1: Averaged uplift rates between 2003-2012 for (a) the spherical NM model and (b) the flat Earth FE model. Black dots indicate GPS locations.

and their histograms are depicted in Figure S2. The differences vary between 0.5 and 2.5 mm/yr. The largest differences (>1mm/yr) correspond to the Yakutat Icefields. Note that regions outside Southeast Alaska are not included in this statistical analysis, as differences between the two models are close to zero outside this region. The relatively larger magnitude in the Yakutat Icefields is likely due to the enhanced ice loss modelled for this area, which leads to larger differences in the relaxation times between the FE and NM models. In addition, the enhanced ice loss in this area is implemented with an increase in ice loss rate at three disks in the spherical model (Hu & Freymueller, 2019), which is smoothed in the finite element model. Overall, the differences between the normal-mode and finite element models are due to a number of factors, which include (i) discretization of the ice model, (ii) fundamental differences between the two methods, such as

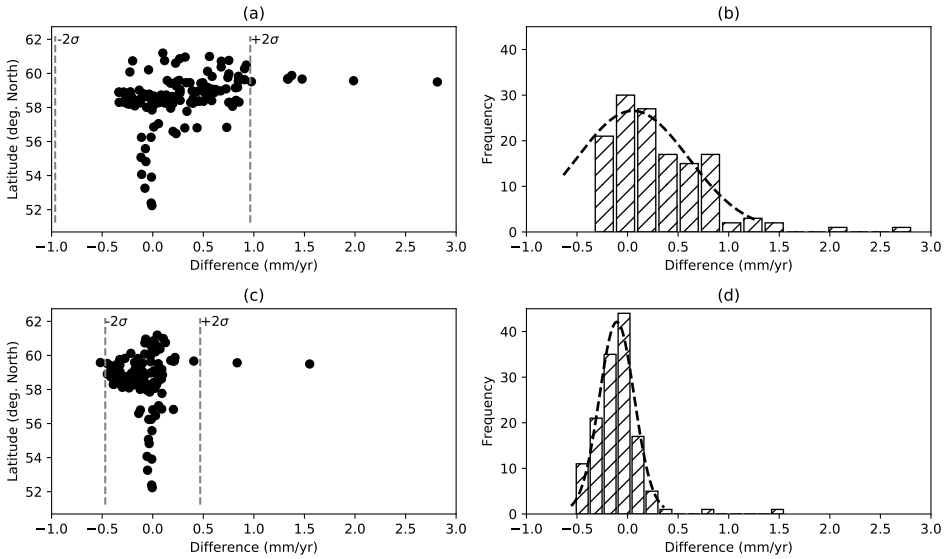

Figure S2: Differences in uplift between the finite element and normal-mode models and their histograms. (a), (b) and (c), (d) correspond to the periods 1995-2003 and 2003-2012, respectively. The dotted curves in (b) and (d) are fitted to a Gaussian distribution covering the 95% confidence interval. Only the viscoelastic response since the LIA is modelled here.

neglect of sphericity and self-gravitation in the FE model, resulting in different relaxation times.

The models are tested against the observational data, using a Chi-square (χ^2) test. The Chi-square values for the FE and NM models are 17.7 and 17.2, respectively, which are relatively close to each other. Note that the prior value is larger in the main text, as the model performance was tested against the GPS dataset in Hu & Freymueller (2019), which has less measurement points in comparison to the dataset used in the main text.

1.2 Horizontal velocities

Differences in horizontal velocities are between -0.8 and 0.3 mm/yr for the period 2003-2012, as shown in Figure S3. Differences in the direction are negligible (not shown in the figure). The largest differences can be seen in the vicinity of the maximum ice load. Farther away the differences in magnitude are negligible. The flat-Earth model is very similar to the spherical model in the far field, however, in the near field careful consideration of the horizontal velocities. Even though the absolute difference is relatively small and not detectable by a GPS network (<1 mm/yr), in could produce a small bias for this small region.

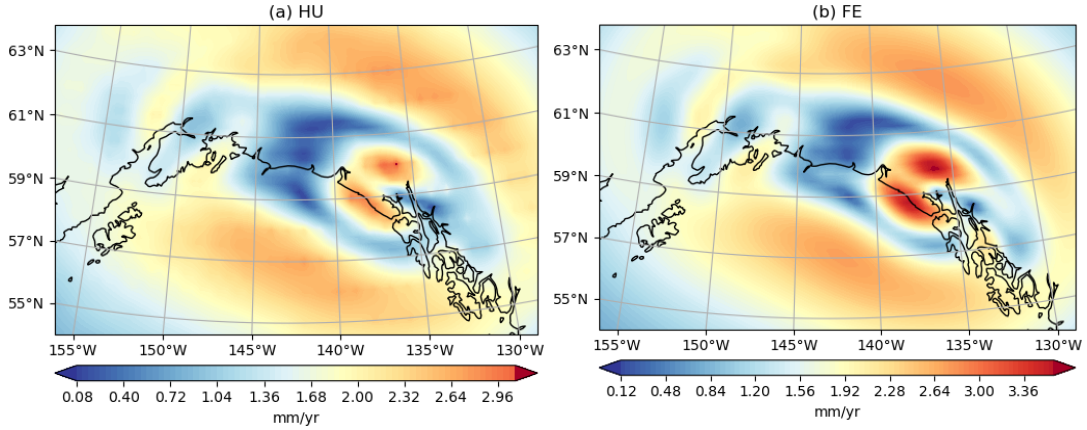

Figure S3: Magnitude of horizontal velocities for (a) the spherical HU model and (b) the flat Earth FE model.

2 Compressibility effects

To study compressibility effects, we assume material compressibility by using the scheme by Wu (2004). Generally, compressibility can be separated into material compressibility (i.e. the Poisson's ratio is smaller than 0.5) and internal buoyancy (i.e. the dilation of the material causing buoyancy) (Klemann et al., 2003). One cannot simply turn off one of these components as compressibility will lead to dilatation. Numerical instabilities could arise upon deformation of an element due to the perturbed density when dilatation is turned on (Wu, 2004). In using the scheme by Wu (2004) we ignore the effects of density changes by assuming that the effects are small. Only the materials

Poisson's ratio is changed, while keeping the internal buoyancy at zero.

2.1 Effect on uplift

Figures S4 and S5 show the spatial effect on the average velocities when material incompressibility is incorporated by changing the Poisson's ratio to 0.28 for each element. A non-uniform increase in uplift is seen which is related to the heterogeneous ice load history. The largest increase is seen around the Yakutat Icefields (16-18%) where PDIM effects are largest. In Glacier Bay, an increase of 12-14% is seen. The areas surrounding the modelled ice load the effects are between 6-9%. Also, the area affected by positive uplift is increased and the velocity of the fore-bulges are slightly decreased (not shown).

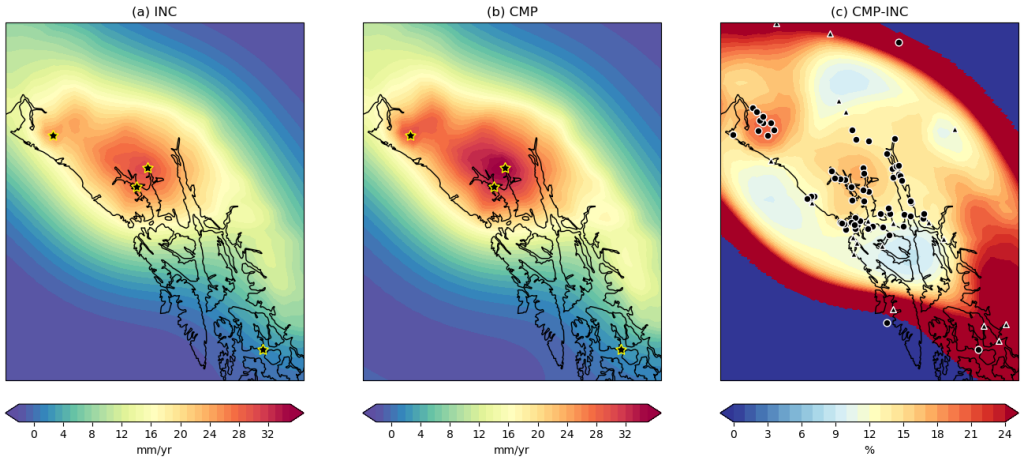

Figure S4: Averaged uplift rate (1992-2003) for (a) an incompressible Earth and (b) a compressible Earth. The differences (c) are largest at the center of Glacier Bay up to 4.7 mm/yr. The stars mark the GPS stations from top to bottom: YAKU, BAGO, CINC and LEV1. Circles represent differences detected by the GPS network within 1σ uncertainty, whereas triangles represent differences that cannot be detected. Only LIA and PDIM effects are modelled.

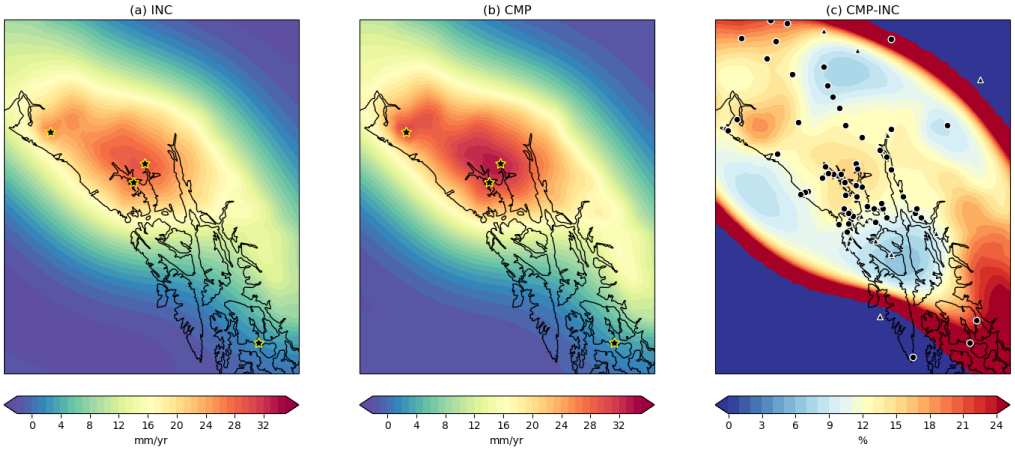

Figure S5: Averaged uplift rate (2003-2012) for (a) an incompressible Earth and (b) a compressible Earth. The differences (c) are largest at Yakutat up to 5.3 mm/yr. The stars mark the GPS stations from top to bottom: YAKU, BAGO, CINC and LEV1. Circles represent differences detected by the GPS network within 1σ uncertainty, whereas triangles represent differences that cannot be detected. Only LIA and PDIM effects are modelled.

One of the implications of an incompressible model is that it leads to a larger effective lithospheric thickness. Tanaka et al. (2011) showed that by adjusting the flexural rigidity of the incompressible model so that it matches the flexural rigidity of the compressible model, the differences in uplift rate almost disappear. To match the flexural rigidity, the elastic constants and the thickness of the lithosphere can be adjusted. Here, we will only adjust the thickness of lithosphere. To do this, the model mesh is updated to allow for change in the elastic lithospheric thickness in steps of 5 km. The density and elastic parameters are kept constant, whereas the viscosity is updated for each layer. The difference between a compressible model with lithospheric thickness of 55 km is compared with an incompressible model with varying lithospheric thickness. The differences between compressible model and that of an incompressible model with lithospheric thickness of 40, 45, 50 and 55 km can be seen in Figure S6.

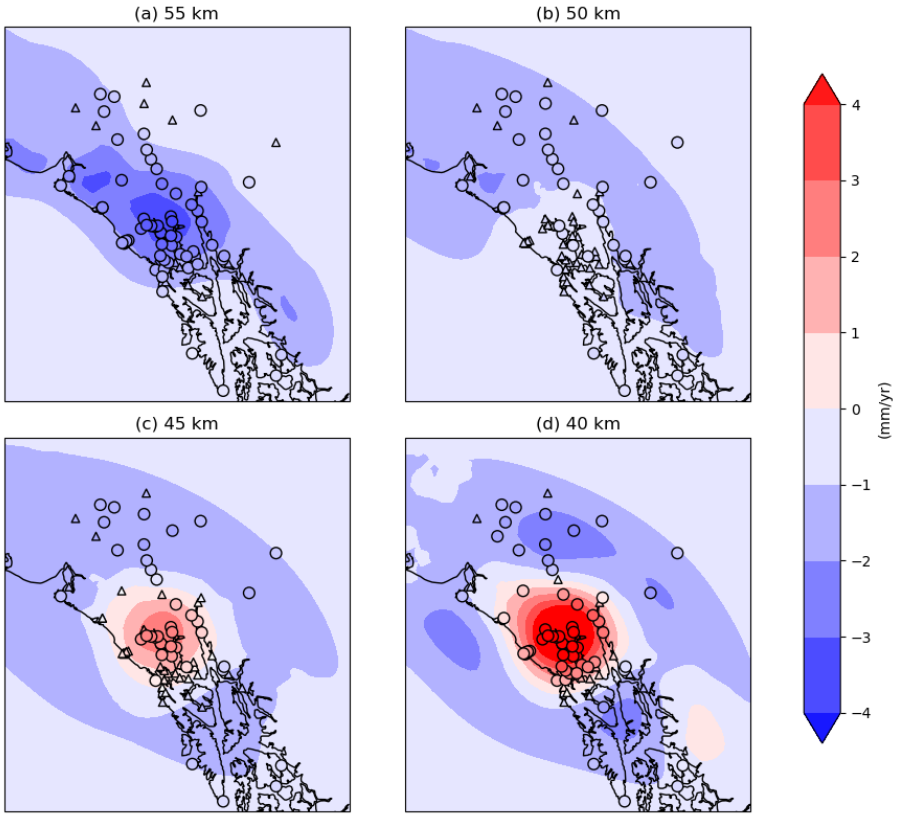

Figure S6: Incompressible models with adjusted lithospheric thickness. In each plot the difference between the compressible model with lithospheric thickness 55 km and the incompressible model with variable thickness is depicted (the former is subtracted from the latter). Circles represent differences detectable by the GPS network within 1σ uncertainty, whereas triangles cannot be detected. Only LIA and PDIM effects are modelled.

Theoretically, the flexural rigidity of a plate is computed using $D = Eh^3/12(1-\nu^2)$ (e.g. Karato, 2008), where E is the Young's modulus, h the elastic lithospheric thickness and ν the Poisson's ratio. A compressible model ($\nu = 0.28$) with lithospheric thickness of 55 km should have the same flexural rigidity of an incompressible model ($\nu = 0.5$) with lithospheric thickness 51.3 km. The results in Figure S6 show that a single lithospheric thickness for a compressible model

cannot reproduce the same results as an incompressible model. The closest approximation are obtained for elastic thicknesses of 45 and 50 km, which is slightly lower than the theoretical value. To match the results in Yakutat, a thinner lithosphere is required than in Glacier Bay. This shows that compressibility alters the relaxation times, which cannot be obtained with an incompressible model with another lithospheric thickness. In other words, the effects of material compressibility cannot be obtained with an incompressible model with a thinner lithosphere.

2.2 Effect on horizontal velocities

The horizontal velocities for an incompressible and compressible Earth are depicted in Figure S7. The direction of the velocities is not affected by compressibility, instead, the magnitude changes. The horizontal velocities for the incompressible case reach a maximum of 4.4 mm/yr around Glacier Bay, whereas for the compressible case this value is 5.7 mm/yr. Many of the differences are between 0-2 mm/yr, which cannot be distinguished by the GPS observations (1-2 mm/yr). A small area, just south of the Yakutat Ice Fields does show a significantly larger difference of 3.0 mm/yr, suggesting that an incompressible model would underestimate the horizontal motion in this area slightly.

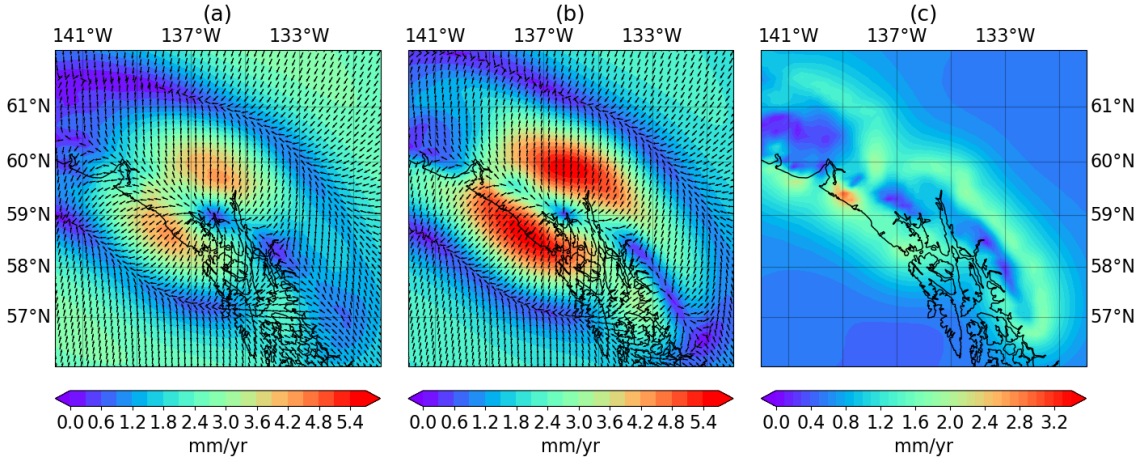

Figure S7: Average horizontal velocities (2003-2012) for (a) an incompressible Earth and (b) a compressible Earth. Arrows indicate the direction of the horizontal velocities. The differences (c) are largest around Glacier Bay. Only LIA and PDIM effects are modelled.

3 Effects of present-day ice melt on uplift

The PDIM effects are investigated here by adjusting the ice load model. Three experiments are conducted. Experiment I includes the entire ice load model till 2012. In Experiment II the ice load is stopped 2003 and in Experiment III the ice load is set to zero in 1995. All experiments use a compressible earth model with a HU rheology profile (i.e. the best-fit parameters by Hu & Freymueller (2019)).

Figures S8 and S9 show the results of and differences between experiments I/III and I/II, respectively. The differences between experiment I and III lead up to -16.3 mm/yr and -14.3 mm/yr between experiments I and II. This peak is reached at the Yakutat Ice Fields where PDIM effects
105 are largest. PDIM effects around the Yakutat Icefields and Glacier Bay account for approximately 45-50% and 25% of the uplift caused by the viscoelastic response (LIA and PDIM), respectively. Larsen et al. (2005) predicted that the elastic uplift rates account for 40% and 15% of the observed uplift near the Yakutat Icefield and in Glacier Bay, respectively. The larger predictions in this study are due to the enhanced ice loss modelled.

110 The difference between experiment II and III vary between 0.0 and 2.0 mm/yr. This difference shows that the ice loss in 1995-2003 adds a contribution up to 2.0 mm/yr on the viscoelastic response in 2003-2012. The largest differences (2.0 mm/yr) are seen around the Yakutat Icefields and for Glacier Bay the contribution is up to 1.5 mm/yr.

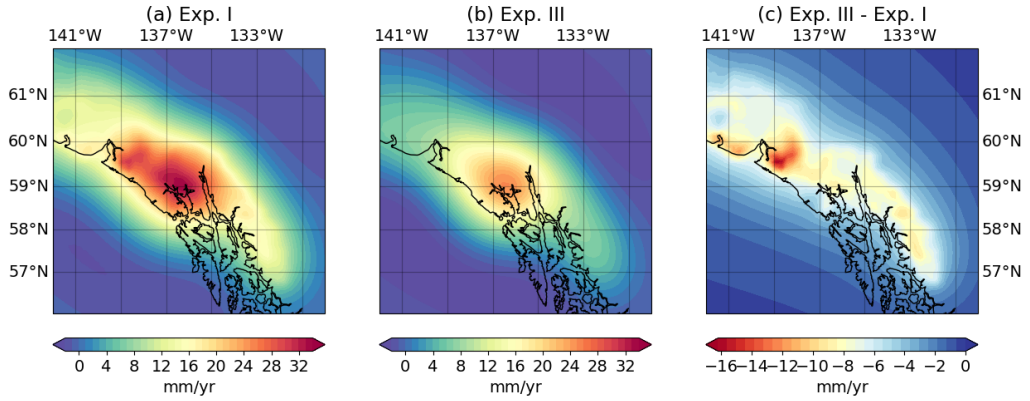

Figure S8: Average uplift (2003-2012) for (a) ice loading ends in 2012 and (b) ice loading ends in 1995. In (c) the differences between (b) and (a) are plotted. Only (post-)LIA effects are modelled.

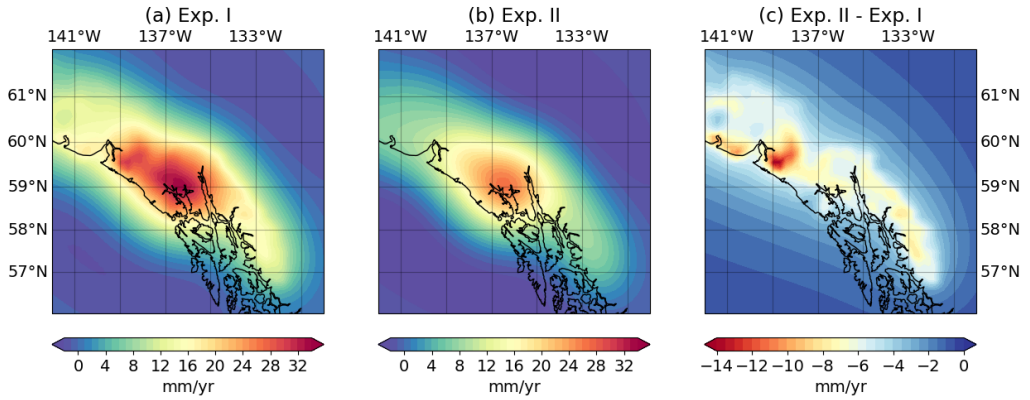

Figure S9: Average uplift (2003-2012) for (a) ice loading ends in 2012 and (b) ice loading ends in 2003. In (c) the differences between (b) and (a) are plotted. Only (post-)LIA effects are modelled.

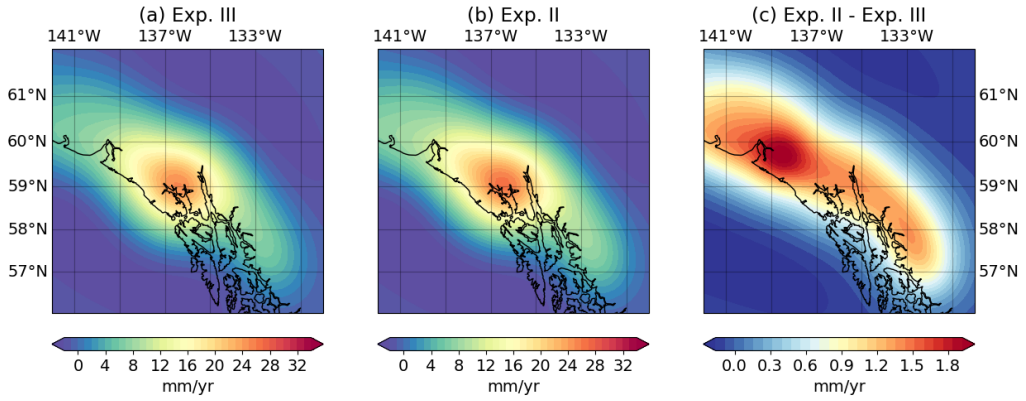

Figure S10: Average uplift (2003-2012) for (a) ice loading ends in 1995 and (b) ice loading ends in 2003. In (c) the differences between (b) and (a) are plotted. Only (post-)LIA effects are modelled.

4 Crustal flow

Crustal composition can significantly affect the GIA (Schotman et al., 2009). Here we investigate the effect of crustal flow in Southeast Alaska. We assume the following creep law for the crust (e.g. Tesauro et al., 2015):

$$\dot{\epsilon} = A \exp\left(-\frac{E}{RT}\right)\sigma^n \tag{1}$$

in which A is the pre-exponental factor, E the activation energy, R the gas constant, T the temperature and σ the stress to a power n. Tesauro et al. (2015) defines the crustal rheology of the North American lithosphere with input from the crustal seismic model NACr14 (Kaban et al., 2014). Rheologies of the upper, middle and lower crust layers are assigned based on the magnitude of seismic velocities. We use the assigned rheology covering Southeast Alaska (category 6 in Table 1 in Tesauro et al. (2015)). We determine the thickness of the crustal layers in the FE model based on average crustal thicknesses by the NACr14 model in Southeast Alaska. The rheology parameters for each layer are shown in Table S3. We acknowledge that these values should be taken with care considering the uncertainties and that the crustal layers may behave under the brittle regime. Shallow earthquakes have been recorded at depths 10 km (U.S. Geological Survey, 2019), indicating a non-ductile regime. Nevertheless, this can give insights in the effects of crustal flow when a ductile regime for the crust is modelled.

Opposed to the main article, where diffusion creep ($n = 1$) was considered everywhere, we use a power law rheology in the crust so that we can implement the parameters in Table S3. We use temperatures from WINTERC-3D Fullea et al. (2019), where temperatures in the crust are consistent with results in Hyndman et al. (2009). The resultant dislocation creep parameters in the crust vary between 10^{-40} and 10^{-35} Pa^{-3} s^{-1}. We did not compute the stresses involved, but with a stress of 1 MPa the effective viscosity is of the order $10^{28} - 10^{32}$ Pa s. The simulations

Table S3: Overview of rheological parameters for materials in the crust. Composition by Tesauro et al. (2015) (category 2). Depths are based on average crustal thicknesses and assigned to the FE layer.

Layer	Depth (km)	Composition	A $\mathrm{Pa}^n\mathrm{s}^{-1}$	n	E kJ mol^{-1}
Upper crust	0-12	Dry Quartzite[(a)]	6.03×10^{-24}	2.72	134
Middle crust	12-26	Wet Diorite[(a)]	1.26×10^{-16}	2.4	212
Lower crust	26-40	Dry Diabase[(a)]	6.31×10^{-20}	3.05	276

[(a)]Carter & Tsenn (1987)

showed no notable differences in uplift when crustal flow was modelled. We conclude that the GIA in this region is insensitive to the crustal rheology modeled here as the crust effectively behaves elastic due to the high viscosities involved.

5 Supplementary figures

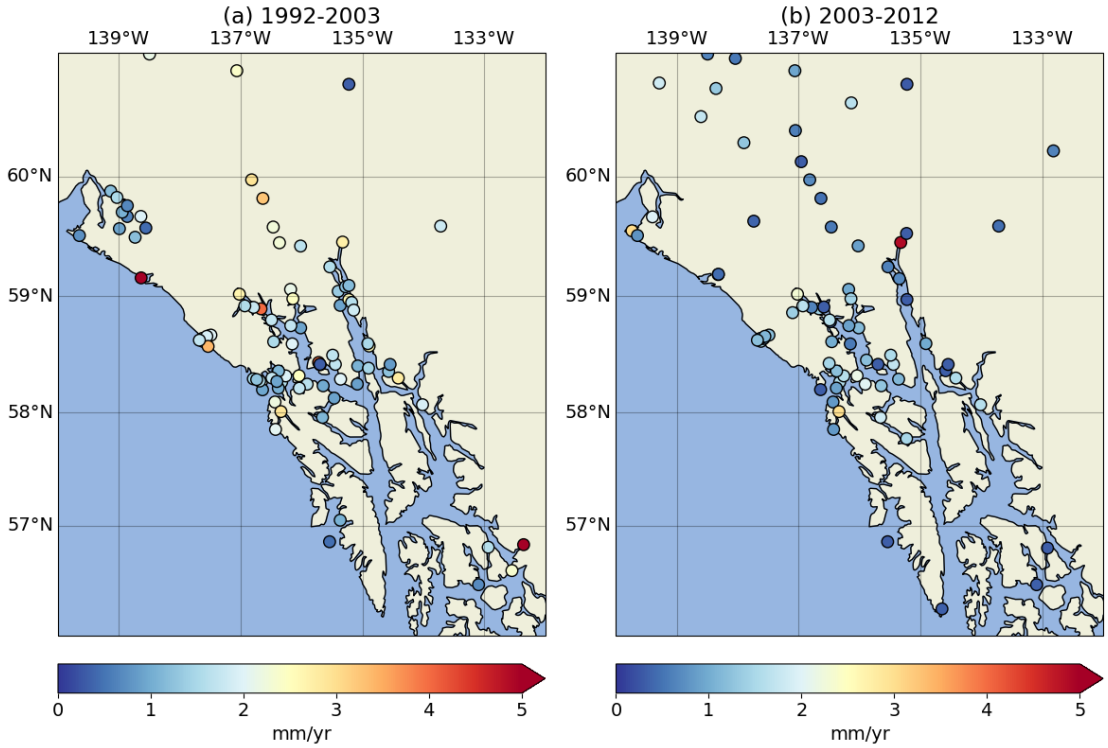

Supplementary Figure S1: GPS uncertainties in Southeast Alaska for (a) 1992-2003 and (b) 2003-2012. Most uncertainties are between 1-2 mm/yr but a select number of points have larger uncertainties between 5-8 mm/yr. Data from Hu & Freymueller (2019).

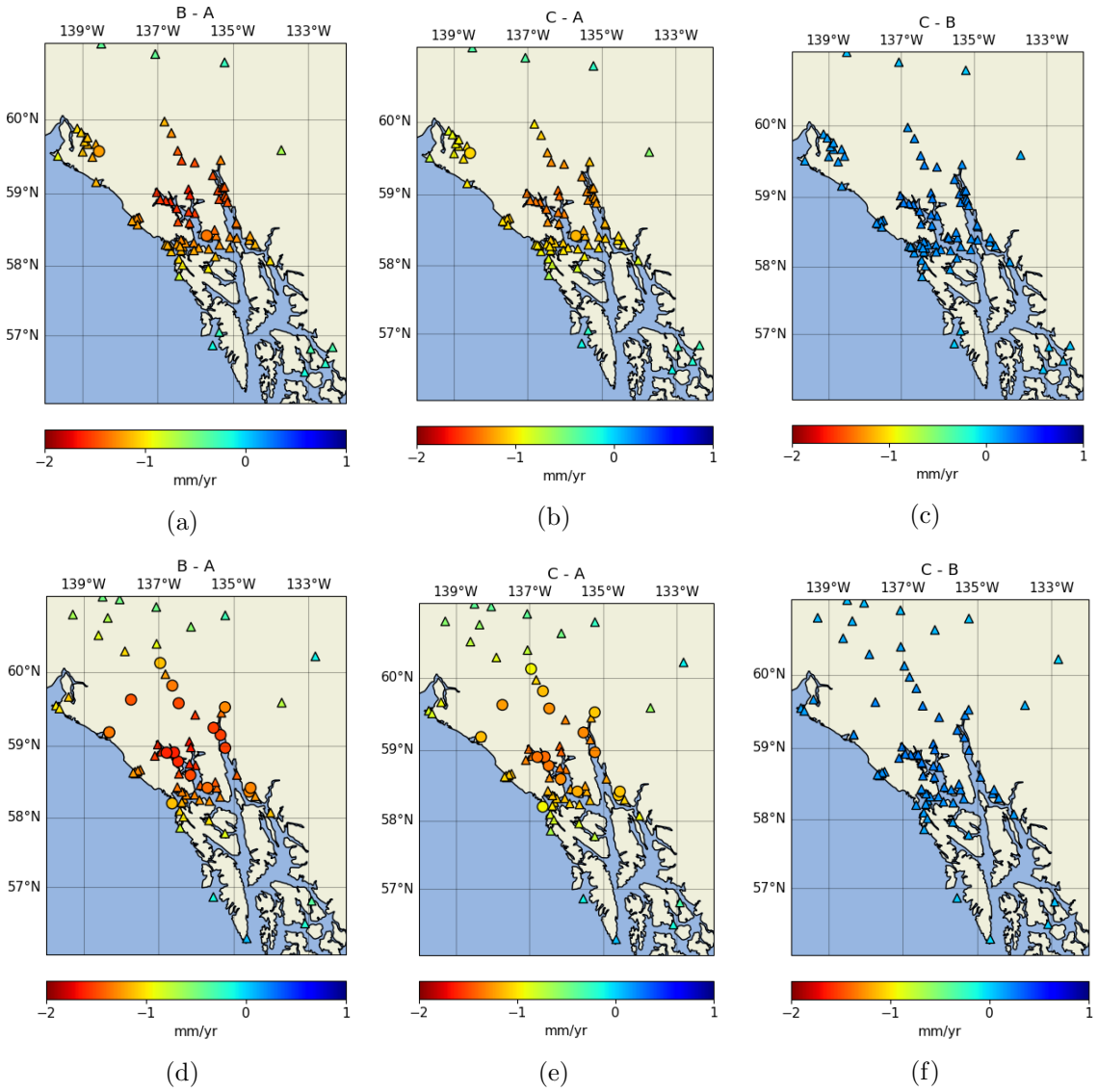

Supplementary Figure S2: Difference maps of 3 best-fit models. Subfigures (a)-(c) correspond to the period 1992-2003 and subfigures (d)-(f) correspond to the period 2003-2012. Models A, B and C have different grain size (d) and water content (f_{H_2O}). Model A ($\chi^2 = 20.7$): (d, f_{H_2O}) = 8mm, 400 H/10^6Si. Model B ($\chi^2 = 20.9$): (d, f_{H_2O}) = 9mm, 500 H/10^6Si. Model C ($\chi^2 = 20.6$): (d, f_{H_2O}) = 10mm, 700 H/10^6Si. Circles represent residuals resolved with the GPS uncertainty of 2σ and triangles indicate residuals that cannot be resolved.

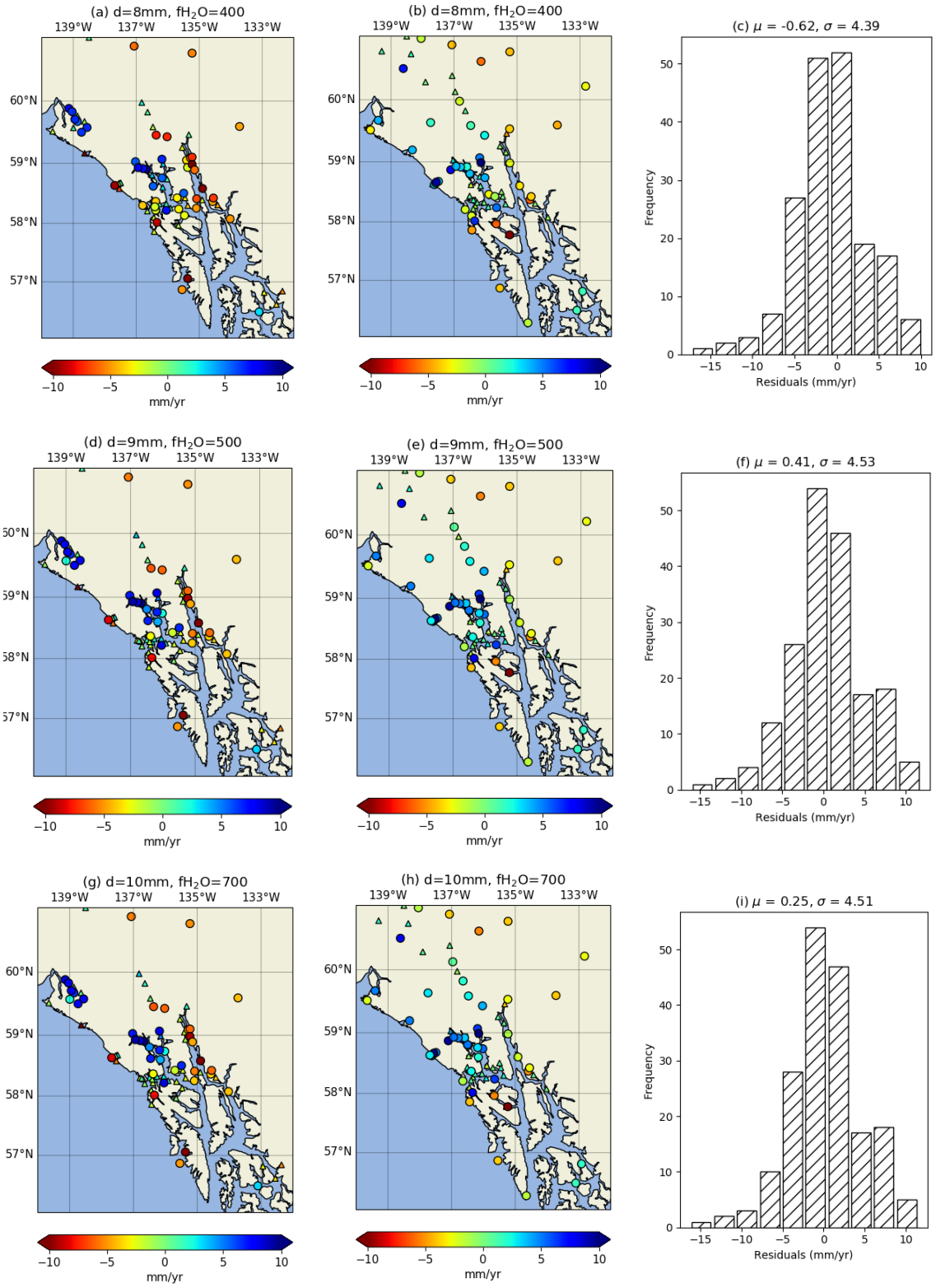

Supplementary Figure S3: Residual maps and histograms of the 3 best fit models obtained through creep flow laws. Subfigures a, d and e correspond to the period 1992-2003. Subfigures b, e and f correspond to the period 2003-2012. The histograms capture all of the residuals of both periods. Circles represent residuals resolved with the GPS uncertainty of 2σ and triangles indicate residuals that cannot be resolved.

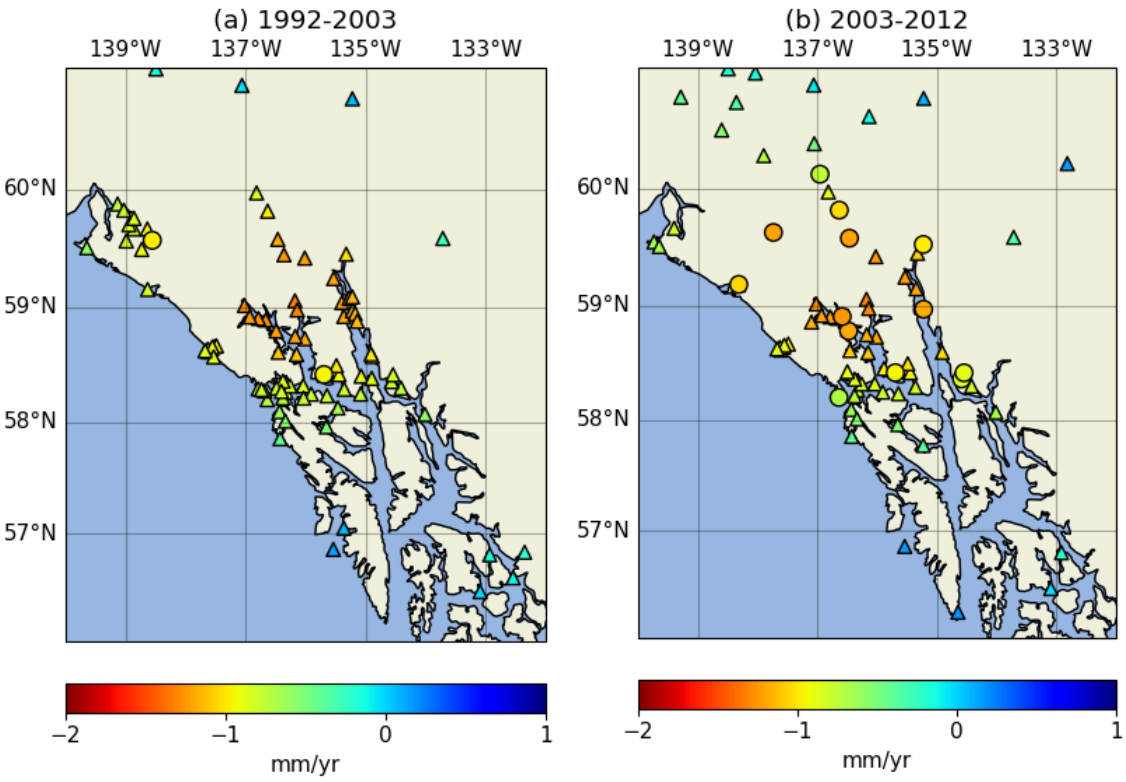

Supplementary Figure S4: Spatial differences between the two best-fit models for the thermal contribution results. Differences are obtained by subtracting model A ($\eta_0 = 5.0 \times 10^{10}$, $\beta = 0.1$) from model B ($\eta_0 = 5.5 \times 10^{10}$, $\beta = 0.1$) . Circles indicate that differences can be resolved by the GPS data within 2σ uncertainty, whereas triangles indicate that the differences cannot be resolved.

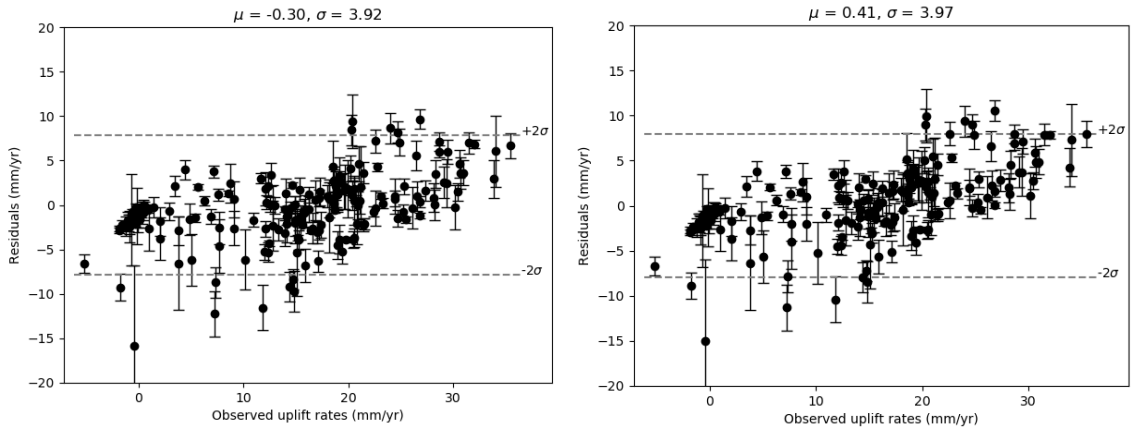

(a) model A (b) model B

Supplementary Figure S5: Histogram of residuals of model A ($\eta_0 = 5.0 \times 10^{10}$, $\beta = 0.1$) and model B ($\eta_0 = 5.5 \times 10^{10}$, $\beta = 0.1$).

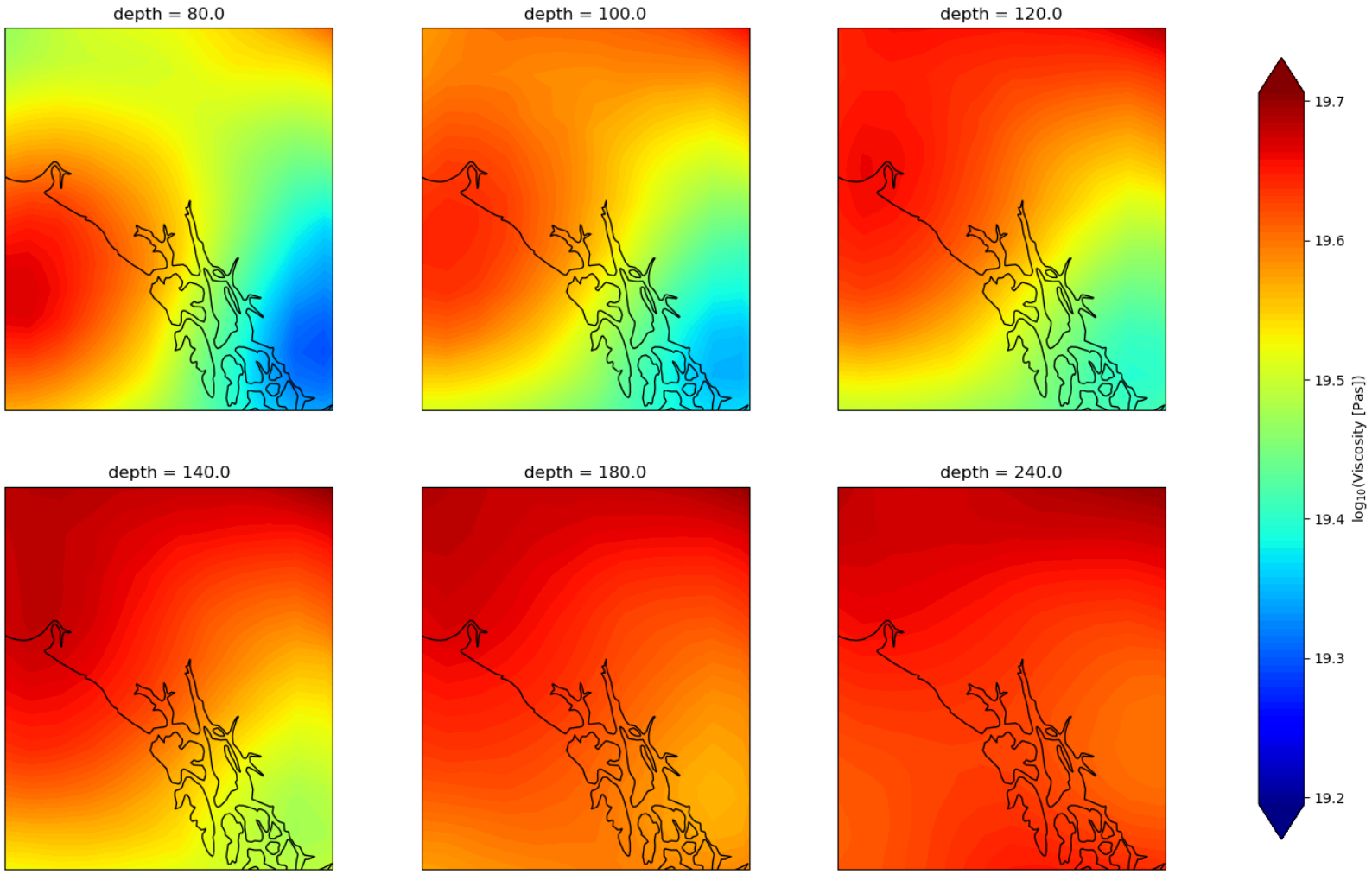

Supplementary Figure S6: Effective viscosity at different depths of the best fit 3D model where $\beta = 0.1$ and $\eta_0 = 5.0 \times 10^{19}$ Pas.

References

Carter, N. L. & Tsenn, M. C. (1987). Flow properties of continental lithosphere. *Tectonophysics*, 136(1), 27 – 63.

Fullea, J., Lebedev, S., Martinec, Z., & Celli, N. (2019). Winterc: a new global thermochemical model of the uppermost mantle constrained by surface waves, heat flow, surface elevation and gravity satellite data. *Living Planet Symposium*.

Hu, Y. & Freymueller, J. T. (2019). Geodetic observations of time-variable glacial isostatic adjustment in southeast alaska and its implications for earth rheology. *Journal of Geophysical Research: Solid Earth*, 124(9), 9870–9889.

Hyndman, R., Currie, C., Mazzotti, S., & Frederiksen, A. (2009). Temperature control of continental lithosphere elastic thickness, te vs vs. *Earth and Planetary Science Letters*, 277, 539–548.

Kaban, M. K., Tesauro, M., Mooney, W. D., & Cloetingh, S. A. P. L. (2014). Density, temperature, and composition of the north american lithosphere: New insights from a joint analysis of seismic, gravity, and mineral physics data: 1. density structure of the crust and upper mantle. *Geochemistry, Geophysics, Geosystems*, 15(12), 4781–4807.

Karato, S. (2008). *Deformation of Earth Materials: An Introduction to the Rheology of Solid Earth*. Cambridge University Press.

Klemann, V., Wu, P., & Wolf, D. (2003). Compressible viscoelasticity: stability of solutions for homogeneous plane earth models. *Geophys. J. Int.*, 153, 569?585.

Larsen, C. F., Motyka, R. J., Freymueller, J. T., Echelmeyer, K. A., & Ivins, E. R. (2005). Rapid viscoelastic uplift in southeast alaska caused by post-little ice age glacial retreat. *Earth and Planetary Science Letters*, 237(3), 548 – 560.

Schotman, H., Vermeersen, L., Wu, P., Drury, M., & de Bresser, J. (2009). Constraints on shallow low-viscosity zones in northern europe from future goce gravity data. *Geophys. J. Int*, 178, 65–84.

Tanaka, Y., Klemann, V., Martinec, Z., & Riva, R. E. M. (2011). Spectral-finite element approach to viscoelastic relaxation in a spherical compressible Earth: application to GIA modelling. *Geophysical Journal International*, 184(1), 220–234.

Tesauro, M., Kaban, M., & Mooney, W. (2015). Variations of the lithospheric strength and elastic thickness in north america. *Geochemistry, Geophysics, Geosystems*, 16, 2197–2220.

U.S. Geological Survey (2019). Search earthquake catalog. accessed March 3rd, 2020.

Wu, P. (2004). Using commercial finite element packages for the study of earth deformations, sea levels and the state of stress. *Geophysical Journal International*, 158(2), 401–408.

4

Conclusion and Recommendations

In this chapter conclusions are drawn from the results and the research questions posed in the introduction are answered. Furthermore, a number of recommendations are mentioned for future work.

4.1. Conclusions

Firstly, the sub-questions are answered in a convenient order. Then, the main research question is answered.

1. *To what extent do lateral variations affect the GIA model predictions in comparison with a radially symmetric GIA model?*

   The inclusion of lateral variations in the Earth rheology had not yet been implemented in the current GIA models for Southeast Alaska. In this research two approaches are used to implement a 3D viscosity structure in shallow the upper mantle. The viscosity in deeper Earth layers have little effect on GIA due to the short wavelength of the ice load. Hence, deeper layers are not of interest in this study.

   In the first approach, the viscosity distribution was inferred using a 3D temperature model and flow laws for olivine. An optimal viscosity distribution was found by varying the grain size and water content in the flow law. However, the results show that this 3D model could not produce a better result than the 1D model and severely underestimates the GIA rates at Glacier Bay and at the Yakutat Icefields (>5 and >2 mm/yr more than the 1D model, respectively). This is attributed to the temperature profile, which has a much thicker thermal lithosphere than that was found by a regional study (Hyndman et al., 2009). As a result the viscosity in the upper 100 km is relatively large and thus the elastic lid is much thicker than in the 1D model (55km). Thus, this approach is not used to investigate the effect on lateral variations. Instead, the focus is set on the results of an alternative approach described next.

   The second approach translates viscosity anomalies into viscosity perturbations. A β parameter is introduced to scale the magnitude of the viscosity anomalies. A β parameter with value 0 indicates a homogeneous viscosity structure, whereas a value of 1 indicates that only thermal effects are contributing to seismic anomalies. The shear wave anomalies in this region are negative and this corresponds to a weaker upper mantle, resulting in higher uplift rates. To account for this effect, the background viscosity is increased. Around the larger ice load changes (Glacier Bay and the Yakutat Icefields), a β increase from 0.1 to 0.2 results in twice the increase in velocity with respect to a 1D model. Past the ice margin the increase quickly deteriorates to zero (except for at the fore-bulges where rates decrease with ~0.6mm/yr). From $\beta = 0$ to $\beta = 1$ (i.e. the best-fit value), uplift rates at Glacier Bay increase with 3-3.5 mm/yr and at the Yakutat Icefields approximately with 1.5 mm/yr. At another zone on the south-eastern margin of the area of interest, the increase is relatively larger considering the extent of the ice load. Ice load changes here are relatively small whereas lower seismic anomalies are seen, resulting in higher uplift rates. This can be interpreted as a flaw in the 3D model. Seismic velocities in this region are low, but the thermal contribution may be locally lower here due to other effects such as partial melt or water content. Nevertheless, errors from the ice load model may also play a role. For example, the ice load history may be asynchronous with respect to the regional ice load model in this region such

that there is less ice loss mass than currently modelled. Note that the above values are purely the result of changing the β parameter, without looking at the fit, which is discussed in the next sections.

2. *To what extent are experimental flow law parameters for diffusion constrained by the GIA observations?*

   Until now, no regional GIA studies have investigated the the potential of flow laws in Southeast Alaska. A number of assumptions were made by using these flow laws. First of all, flow laws for olivine are adopted and it is assumed that olivine is the main constituent responsible for deformation. Secondly, only a linear rheology (diffusion mechanism) is considered. This was purposely chosen to avoid having a mantle rheology dependent on stress. Background stresses may play an important role in this region and are therefore not taken into account in this research. Moreover, partial melt is not modelled. Only the water content and grain size are varied as they are assumed to influence the viscosity structure the most. For simplicity and lack of evidence, these parameters are constant in both lateral and vertical directions. Even though xenolith samples show a possible range of grain sizes, a single grain size is assumed to obtain the viscosity structure. Moreover, enhanced water content and partial melt may play an important role in select areas. Any uncertainties are reflected back into the obtained water content and grain size.

   The results show an optimal fit for a viscosity structure with a grain size of 8 mm and water content of 400 H/10^6 Si. Other combinations with good fits include a grain size of 9 mm with water content 500 H/10^6 Si and grain size of 10 mm with water content 700 H/10^6 Si. A trend was observed that similar viscosity distributions can be obtained with higher grain size and water content. However, these were outside the search space as larger grain sizes were not found in xenolith data. The grain sizes found are somewhat larger than the typical sizes found in xenoliths; however, it is in the acceptable range (< 10 mm). A wet rheology is preferred as dry rheologies result in too low uplift rates. Moreover, the best fit model under predicts the rates at the two uplift peaks between 5-9 mm/yr. Even though the remaining best fit models (the 1D model and 3D model obtained directly from shear wave anomalies) also under predict the GIA at the same location, this 3D model has larger residuals. There are several factors which can explain why this model is not performing that well. These include the temperature model, uncertainties in flow law parameters, deformation mechanism and compositional effects. The temperature model used here is not consistent with findings by a regional study (Hyndman et al., 2009). Generally, the upper temperatures in the first 60 km are similar. However, Hyndman et al. (2009) shows a change in temperature gradient starting around 60 km, which follows the adiabatic gradient, whereas the adiabatic gradient in this study starts at approximately 100 km. The differences are likely to be attributed to the strong anelastic corrections made in Hyndman et al. (2009). A thicker thermal lithosphere results in larger viscosities at depths shallower than 60 km. As a result, the effective elastic thickness is larger than that of the 1D model. Past GIA studies focused on this region showed that a thinner lithospheric thickness underlain with a higher mantle viscosity is required to explain the increasing uplift rate. It is concluded that the effective elastic thickness is the main reason that uplift rates are under predicted. Locally higher water content and partial melt are assumed to be secondary effects and these uncertainties are absorbed by the obtained uniform grain size and water content.

3. *To what extent are the parameters to determine the viscosity distribution directly from mantle shear wave velocities constrained by GIA observations?*

   To answer this question a search was performed to find the optimal combination of the β parameter and the background viscosity η_0 in the asthenosphere. The initial background viscosity is taken from Hu and Freymueller (2019). The asthenospheric viscosity is then increased as seismic wave anomalies have a weakening effect on the upper mantle in Southeast Alaska. Previous GIA models in Alaska only considered an incompressible model, whereas in this study a compressible model is adopted. It was shown that due to compressibility effects a higher background viscosity is preferred as uplift rates increase with compressibility. The best fit model was obtained with $\beta = 0.1$ and $\eta_0 = 5.0 \times 10^{19}$ Pa s. The misfit found was $\chi^2 = 13.7$ with the mean and standard deviations of the residuals being -0.30 mm/yr and 3.92 mm/yr, respectively. A higher background viscosity would result in lower uplift rates and higher β values result in higher uplift rates. No other combination was found (i.e. higher viscosity and higher β) was found to produce a similar fit. This suggests that the solution is unique and that small lateral variations (up to 0.4 log units) can improve the overall fit. There are a number of uncertainties in this method (a number of them are explained in the recommendations). It is emphasized that seismic anomalies should be handled with care for regions of high temperatures. Anelastic effects play a larger

role and these could affect the partial derivatives used to derive the viscosity anomalies. In this study partial derivatives were used from Karato (2008) Table 20.2, which represent global averages, including anharmonic and anelastic effects. The question remains whether the anelastic effects are large enough to result in different uplift rates. Moreover, partial melt and water content are not well constrained (Hyndman et al., 2009) and could produce a bias in the results. Both parameters cause a decrease in seismic wave anomalies and it is suggested that these play a role on the southeastern margin of our region of interest (Hyndman et al., 2009). This shows that the β parameter may vary spatially and could produce a bias in the results. Nevertheless, these errors could also be attributed to the ice load model. For example, around the Yakutat Icefields, both the 1D and 3D models systematically under predict the uplift rate, suggesting a higher present-day ice loss rate is required to explain the observed uplift rates. Similarly, the 3D model shows a slightly lower viscosity region in the southwestern corner of our area of interest, which suggest that ice load changes should be lower here to obtain a better fit with the same earth model.

What is the impact of the inclusion of lateral variations in the Earth rheology in glacial isostatic adjustment models on uplift predictions in Southeast Alaska?

In this study two approaches were used to infer lateral variations in the upper mantle viscosity. It is demonstrated that different data sources can be used to derive lateral variations and agree with the GIA observations. The first approach, which used a readily available 3D temperature structure showed maximum variations in viscosity at depths between 150 and 200 km depth are up to 0.6 log units (equivalent to a factor of 4.0). For the second approach the largest viscosity variations are seen around 100 km depth of up to 0.4 log units (equivalent to a factor of 2.5). Even though a narrow study area is analyzed, the relatively small variations show to have a measureable impact on the GIA, discussed below.

The first approach did not yield better results than a 1D model as the GIA is being severely underestimated, which is for a large part due to the larger effective thickness of the elastic lithosphere. One could either (1) increase PDIM rates at select areas or (2) implement a temperature distribution with a thinner thermal lithosphere resulting in a thinner elastic lithosphere. Hu and Freymueller (2019) incorporated a correction of present-day ice melt rates by increasing the rates with a constant scale with respect to the ice load rates obtained from averaged ice thinning rates for the late twentieth century (Berthier et al., 2010). These scaling factors were 1.8 and 2.2 for the periods 1995-2003 and 2003-2012, respectively. Hu and Freymueller (2019) showed that changing these scaling factors with a value of 0.1 had little effect on the asthenospheric viscosity ($< 10\%$). For Yakutat and Glacier Bay an asynchronous ice load history is implemented with respect to the regional ice load model. Specifically, for Yakutat, the ice loss rates were 3 times higher than the regional rates. The above corrections were also used in this study, however, it is suggested that even higher ice loss rates are necessary in select areas such as the Yakutat Icefields, also for the 3D earth model. The best-fit model parameters (water content and grain size) were within the range found in geologic surveys. A lower viscosity, e.g. by increasing water content or decreasing the grain size, did not yield better results as uplift rates in the vicinity of the two uplift peaks increased too much, worsening the fit.

The second approach yielded better results than the reference 1D model, where seismic anomalies are used to infer lateral variations in the upper mantle. In the area of interest seismic anomalies are negative and thus have a weakening effect on the mantle strength. To counteract this, the background viscosity in the shallow upper mantle is increased. The best fit 3D model has a β value of 0.1, resulting in small lateral variations. Wu et al. (2013) showed that the thermal effect is contributing to approximately 65% to the lateral heterogeneity in the upper mantle under Laurentia and Fennoscandia. The contribution became higher in the deeper mantle. In Southeast Alaska GIA parameters are limited to the shallow upper mantle as the GIA process in Southeast Alaska is less sensitive to viscosity variations deeper within the Earth due to the short wavelength of the ice load. Moreover, in Wu et al. (2013) it was assumed that effects of water content and partial melting were negligible as no subduction zone was in the proximity. In this study it was shown that a hydrated shallow upper mantle is preferred which can also influence the seismic velocities. Note that the southeastern corner of our region of interests is characterized by low seismic waves, this can be attributed to higher water content and/or partial melt. On the other hand, this can also be attributed to uncertainties in the ice load model. For example, ice loss rates can be asynchronous with respect to the regional ice load model here, such that there is less ice loss. Moreover, the sensitivity of seismic anomalies to thermal effects can vary in location. The low β parameter is also attributed to the values chosen as input, such as the background temperature and the velocity derivatives with respect to temperature. For example, Wu et al. (2013) showed that a higher back-

ground temperature results in a higher β value. Similarly, if anelastic corrections are not taken into account or not high enough, than an increase in the viscosity anomaly is seen, and in turn the β parameter should increase. Moreover, it should be acknowledged that the global shear wave tomography SL2013 (Schaeffer and Lebedev, 2013), may produce different lateral variations is seismic velocities than a regional high resolution tomography model.

The sensitivity of the uplift rates with respect to the β parameter was tested. Solely based on two cases where only the β parameter is changed (by 0.1), lateral variations result in 2-3 mm/yr and 3-4 mm/yr more uplift in the Yakutat Icefields and Glacier Bay, respectively. However, other regions are also affected by the increase and the overall fit becomes worse. The viscosity values of the best-fit 3D model ($2-5\times10^{19}$ Pa s) within the shallow upper mantle beneath Southeast Alaska are within the same range found in 1D studies of this region (e.g. Larsen et al., 2005; Sato et al., 2011; Hu and Freymueller, 2019). Lateral variations are large enough in this region, combined with a low viscosity, such that relaxation times vary between years to decadal times. The improvements of the best-fit 3D model are between 1.0 and 2.7 mm/yr which outweigh points where a larger misfit is obtained and are larger than the measurement uncertainty. This demonstrates that the inclusion of lateral variations have a small but measurable effect on the local GIA. The translation of shear wave anomalies to viscosity may not be uniformly over the entire region. It is suggested that for the southeastern corner of our region of interest seismic anomalies are somewhat lower which are attributed to a higher water content/partial melt. Also, errors in the ice load model may play a role and lead to a bias the results.

4.2. Recommendations

In this section a number of recommendations are made for future work. They are listed from highest to lowest priority.

1. *A better ice load model*
   One of the largest uncertainties is the ice load model, both spatially and in time. PDIM rates could be further investigated, which have up until now been based on an older dataset of ice change rates and extrapolated to the present. This is may produce a bias in certain areas, as the melt rate does not increase linearly everywhere. Considering that PDIM has a significant influence on the observed uplift, this could improve the GIA predictions. Moreover, the ice load model can be updated with new empirical data on ice thinning rates, instead of matching present day thinning rates so that the predicted GIA fits to the observations.

2. *An accurate 3D temperature model for the lower crust and upper mantle*
   The temperature model was not consistent with findings of a regional study. The temperature model used in this research showed a thicker thermal lithosphere. As a result, viscosity jumps in the upper 100 km are the largest and viscosities here are much larger than previous 1D GIA studies showed (e.g. Larsen et al., 2005; Sato et al., 2011; Hu and Freymueller, 2019). To start with, one can derive a viscosity structure using flow laws with a select number of 1D temperature profiles. This provides insights on the effect of a thinner thermal lithosphere, for example. The next step is to implement a 3D structure and analyze what the effect is of lateral variations.

3. *Implement a non-linear rheology with constant background stress*
   In this study only a linear rheology was considered. Experimental laboratory data shows that diffusion and dislocation creep can occur simultaneously. The implementation of a non-linear or composite rheology does have a number of implications. First of all, studies have shown that non-linear and composite rheologies result in lower uplift rates (van der Wal et al., 2010). Due to unloading of ice, where stress levels decrease, uplift rates tend to decrease rapidly (Wu, 1998). In other words, the relaxation times reduce. It cannot be deduced how present-day uplift rates will change due to a larger relaxation, as both past glaciations and PDIM are modelled together. If indeed present-day uplift rates decrease, than this is also a problem for the 1D and 3D models (this study) for Southeast Alaska, since the linear models already underestimate the GIA at the peak observations. In such a case, only implementing a non-linear or composite rheology is not enough. As mentioned earlier, the ice history is one of the larger uncertainties and this could be changed together with a non-linear rheology for example. The second point to consider is that ambient tectonic stresses can be high enough in this region such that the GIA process only sees a linear rheology. It is recommended to test different case studies with constant stress to see at which point a non-linear rheology is relevant and also if it is reasonable for this

region.

4. *Transient creep*
   Glacier rebound in Southeast Alaska may not be limited to steady-state creep. Transient creep can also play a significant role. If a load is removed, an instantaneous elastic response is followed by a transient anelastic strain before reaching a steady state response. The transient creep phase is time-dependent and when under constant stress can be written as (Ranalli, 1995, p.80): $\epsilon(t) = \epsilon_e + \epsilon_t(t) + \dot{\epsilon}t$, where ϵ is the strain rate, t is the time, and the indices e and t correspond to the elastic and transient strain rates, respectively. The transient deformation has been shown to play an important role in short-term post-seismic displacements in Central-Alaska (e.g Freed et al. (2006). Transient creep may be at work considering the glacial timescales and should therefore be taken under consideration for future work.

5. *Large scale implementation of the 3D GIA model*
   This study only focused on Southeast Alaska, whereas the ice model is extended over all of Alaska. Considering that lateral variations in viscosity increases towards the east, these could have a relatively larger influence on the predicted GIA. The first approach, where a global temperature model was applied through flow laws to obtain a 3D viscosity distribution, could give a first order approximation of the effects of lateral variations in viscosity on GIA. The second approach would not be suitable as the background viscosity was locally optimized for the GIA effects.

6. *Reducing the computational time of the 3D model*
   3D models are computationally expensive. Even though the focus is set on a relatively small region, a high resolution is required and thus the number of elements large. The number of elements can be reduced by decreasing the number of vertical layers and decreasing the resolution in deeper layers. In this study only two settings for vertical layers were tested which were enough for the purpose of this study. Viscosity jumps reduce significantly from 200 km depth. Also, the lateral variations at deeper depths are less pronounced. This suggests that less vertical layers and lower resolution could suffice to be accurate enough.

A

Appendix A

A.1. Coordinate transformations

The data provided by the temperature, seismic and reference models are given in Latitude Longitude and Altitude (LLA) geodetic coordinates. The flat Earth model uses North East Down (NED) Cartesian coordinates. The transformation from LLA to NED occurs in two levels. First, LLA is converted to the Earth Center Earth Fixed (ECEF) coordinate system with

$$\begin{aligned} X &= (N+h)\cos\phi\cos\lambda \\ Y &= (N+h)\cos\phi\sin\lambda \\ Z &= \left(\frac{b^2}{a^2}N+h\right)\sin\phi \end{aligned} \tag{A.1}$$

where ϕ, λ and h, are the latitude, longitude and height, respectively, X, Y and Z are the Cartesian coordinates, and N is the radius of curvature of the prime vertical:

$$N = \frac{a}{1-e^2\sin^2\phi} \tag{A.2}$$

where a is the semi-major axis, b is the semi-minor axis and e the eccentricity in the WGS84 coordinate system.

The second transformation is from ECEF to NED. In order to accomplish this transformation, a local reference point is chosen. Defined are the location vectors $\begin{bmatrix} X_p & Y_p & Z_p \end{bmatrix}^T$ and $\begin{bmatrix} X_r & Y_r & Z_r \end{bmatrix}^T$ in ECEF for a given point P and reference point, respectively. Then, the vector point $\begin{bmatrix} x & y & z \end{bmatrix}^T$ can be found using:

$$\begin{bmatrix} x \\ y \\ z \end{bmatrix} = \begin{bmatrix} -\sin\phi_r\cos\lambda_r & \sin\phi_r\sin\lambda_r & \cos\phi_r \\ -\sin\lambda_r & \cos\lambda_r & 0 \\ \cos\phi_r\cos\lambda_r & \cos\phi_r\sin\lambda_r & -\sin\phi_r \end{bmatrix} \begin{bmatrix} X_p - X_r \\ Y_p - Y_r \\ Z_p - Z_r \end{bmatrix} \tag{A.3}$$

where ϕ_r and λ_r are the latitude and longitude coordinates of the reference point. In this study, the reference point is the location of Glacier Bay. Moreover, the z-coordinate does not undergo the transformations described above. Points given at an X depth are taken directly as the z-coordinate.

Bibliography

A. A. Arendt, K. A. Echelmeyer, W. D. Harrison, C. S. Lingle, and V. B. Valentine. Rapid wastage of alaska glaciers and their contribution to rising sea level. *Science*, 297:382?386, 2002.

A. Barnhoorn, W. van der Wal, B.L.A. Vermeersen, and M.R. Drury. Lateral, radial, and temporal variations in upper mantle viscosity and rheology under scandinavia. *Geochemistry, Geophysics, Geosystems*, 12(1), 2011. doi: 10.1029/2010GC003290. URL https://agupubs.onlinelibrary.wiley.com/doi/abs/10.1029/2010GC003290.

E. Berthier, E. Schiefer, G.K.C. Clarke, B. Menounos, and F. RÃ©my. Contribution of alaskan glaciers to sea-level rise derived from satellite imagery. *Nature Geoscience*, 3:92–95, 2010. doi: 10.1038/ngeo737.

P.E. Calkin and G.C. Wiles. Little ice age glaciation in alaska: A record of recent global climatic change (conf-9006128–vol2). *CONF-9006128–Vol2*, pages 617–625, 1991.

K.G. DeGrandpre and J.T. Freymueller. Vertical velocities, glacial isostatic adjustment, and earth structure of northern and western alaska based on repeat gps measurements. *Journal of Geophysical Research: Solid Earth*, 124(8):9148–9163, 2019. doi: 10.1029/2018JB017163. URL https://agupubs.onlinelibrary.wiley.com/doi/abs/10.1029/2018JB017163.

J.L. Elliott, C.F. Larsen, J.T. Freymueller, and R.J. Motyka. Tectonic block motion and glacial isostatic adjustment in southeast alaska and adjacent canada constrained by gps measurements. *Journal of Geophysical Research: Solid Earth*, 115(B9), 2010. doi: 10.1029/2009JB007139. URL https://agupubs.onlinelibrary.wiley.com/doi/abs/10.1029/2009JB007139.

A.M. Freed, R. Burgmann, E. Calais, and J.T. Freymueller. Stress-dependent power-law flow in the upper mantle following the 2002 denali, alaska, earthquake. *Earth and Planetary Science Letters*, 252(3):481 – 489, 2006. ISSN 0012-821X. doi: https://doi.org/10.1016/j.epsl.2006.10.011. URL http://www.sciencedirect.com/science/article/pii/S0012821X06007321.

J. Fullea, S. Lebedev, Z. Martinec, and N. Celli. Winterc: a new global thermochemical model of the uppermost mantle constrained by surface waves, heat flow, surface elevation and gravity satellite data. *Living Planet Symposium*, 2019.

K. L. Haynie and M. A. Jadamec. Tectonic drivers of the wrangell block: Insights on fore-arc sliver processes from 3-d geodynamic models of alaska. *Tectonics*, 36(7):1180–1206, 2017. doi: 10.1002/2016TC004410. URL https://agupubs.onlinelibrary.wiley.com/doi/abs/10.1002/2016TC004410.

G. Hirth and D. Kohlstedt. *Rheology of the upper mantle and the mantle wedge: A view from the experimentalists*, pages 83–105. Geophysical Monograph Series. Blackwell Publishing Ltd, 1 2003. ISBN 9780875909974. doi: 10.1029/138GM06.

Y. Hu and J.T. Freymueller. Geodetic observations of time-variable glacial isostatic adjustment in southeast alaska and its implications for earth rheology. *Journal of Geophysical Research: Solid Earth*, 124(9):9870–9889, 2019. doi: 10.1029/2018JB017028. URL https://agupubs.onlinelibrary.wiley.com/doi/abs/10.1029/2018JB017028.

R.D. Hyndman, C.A. Currie, S. Mazzotti, and A. Frederiksen. Temperature control of continental lithosphere elastic thickness, te vs vs. *Earth and Planetary Science Letters*, 277:539–548, 2009.

E.R. Ivins and C.G. Sammis. On lateral viscosity contrast in the mantle and the rheology of low-frequency geodynamics. *Geophysical Journal International*, 123(2):305–322, 11 1995. ISSN 0956-540X. doi: 10.1111/j.1365-246X.1995.tb06856.x. URL https://doi.org/10.1111/j.1365-246X.1995.tb06856.x.

Shun-ichiro Karato. *Deformation of Earth Materials: An Introduction to the Rheology of Solid Earth*. Cambridge University Press, 2008. doi: 10.1017/CBO9780511804892.

C.F. Larsen, R.J. Motyka, J.T. Freymueller, K.A. Echelmeyer, and E.R. Ivins. Rapid viscoelastic uplift in southeast alaska caused by post-little ice age glacial retreat. *Earth and Planetary Science Letters*, 237(3): 548 – 560, 2005. ISSN 0012-821X. doi: https://doi.org/10.1016/j.epsl.2005.06.032. URL http://www.sciencedirect.com/science/article/pii/S0012821X05004152.

G. Ranalli. *Rheology of the Earth*. Springer, 1995. ISBN 978-0-412-54670.

K. Roy and W.R. Peltier. Glacial isostatic adjustment, relative sea level history and mantle viscosity: reconciling relative sea level model predictions for the U.S. East coast with geological constraints. *Geophysical Journal International*, 201(2):1156–1181, 03 2015. ISSN 0956-540X. doi: 10.1093/gji/ggv066. URL https://doi.org/10.1093/gji/ggv066.

T. Sato, C.F. Larsen, S. Miura, Y. Ohta, H. Fujimoto, W. Sun, R.J. Motyka, and J.T. Freymueller. Reevaluation of the viscoelastic and elastic responses to the past and present-day ice changes in southeast alaska. *Tectonophysics*, 511:79–88, 2011.

A. J. Schaeffer and S. Lebedev. Global shear-speed structure of the upper mantle and transition zone. *Geophys. J. Int.*, 194 (1):417–449, 2013. doi: doi:10.1093/gji/ggt095.

G. Spada. *The theory behin TABOO*. Samizdat Press, Golden-White River Junction, 2003.

G. Spada, A. Antonioli, L. Boschi, V. Brandi, S. Cianetti, G. Galvani, C. Giunchi, B. Perniola, N.P. Agostinetti, A. Piersanti, and Stocchi P. *TABOO, User Guide*. Samizdat Press, Golden-White River Junction, 2003.

W. van der Wal, P. Wu, P. Hansheng, and Sideris. Sea levels and uplift rate from composite rheology in glacial isostatic adjustment modeling. *Journal of Geodynamics*, 50:38–48, 2010.

W. van der Wal, A. Barnhoorn, P. Stocchi, S. Gradmann, P. Wu, M.R. Drury, and L.L.A. Vermeersen. Glacial isostatic adjustment model with composite 3-d earth rheology for fennoscandia. *Geophysical Journal International*, 194, 04 2013. doi: 10.1093/gji/ggt099.

P Wu. Modelling postglacial sea levels with power-law rheology and a realistic ice model in the absence of ambient tectonic stress. *Geophys. J. Int*, 139:691–702, 1998.

P. Wu. Using commercial finite element packages for the study of earth deformations, sea levels and the state of stress. *Geophysical Journal International*, 158(2):401–408, 08 2004. ISSN 0956-540X. doi: 10.1111/j.1365-246X.2004.02338.x. URL https://doi.org/10.1111/j.1365-246X.2004.02338.x.

P. Wu, H. Wang, and H. Steffen. The role of thermal effect on mantle seismic anomalies under Laurentia and Fennoscandia from observations of Glacial Isostatic Adjustment . *Geophysical Journal International*, 192(1):7–17, 11 2013. ISSN 0956-540X. doi: 10.1093/gji/ggs009. URL https://doi.org/10.1093/gji/ggs009.